Engineered Platforms for the Development of Electroporation-based Tumor Therapies

Elisa M. Wasson

Dissertation submitted to the Faculty of the
Virginia Polytechnic Institute and State University
in partial fulfillment of the requirements for the degree of

Doctor of Philosophy
in
Mechanical Engineering

Rafael V. Davalos, Chair
Scott S. Verbridge
Mark R. Paul
Bahareh Behkam
Thomas E. Diller

December 11, 2019
Blacksburg, Virginia

Keywords: calcium electroporation, irreversible electroporation, microgels, tissue engineering, tumor models, droplet microfluidics

Engineered Platforms for the Development of Electroporation-based Tumor Therapies

Elisa M. Wasson

(ABSTRACT)

Cancer is a complex and dynamic disease that is difficult to treat due to its heterogeneous nature at multiple scales. Standard therapies such as surgery, radiation, and chemotherapy often fail, therefore superior therapies must be developed. Electroporation-based therapies offer an alternative to standard treatments, utilizing pulsed electric fields to permeabilize cell membranes to either enhance drug delivery (electrochemotherapy) or induce cancer cell death (irreversible electroporation). Electroporation treatments show promise in the clinic, however, are limited in the size of tumors that they can safely treat without increasing the applied voltage to an extent that induces thermal damage or muscle contractions in patients. A method to increase ablation size safely is needed. To make this advancement and to advance other cancer treatments as well, better *in vitro* tumor models are needed. Heterogeneity not only makes cancer difficult to treat, but also difficult to recapitulate *in vitro*. This dissertation addresses the complementary need to develop both better cancer therapies and more physiologically relevant *in vitro* tumor models. My results demonstrate that by using a calcium adjuvant with irreversible electroporation treatment, ablation size can be increased without using a higher applied voltage. Additional mechanistic studies identified signaling pathways that were differentially dysregulated under calcium and no calcium conditions, impacting cell death. Finally, I have successfully encapsulated cells in fibrin microgels which may enable the creation of more physiologically relevant and complex 3D *in vitro* and *ex-vivo* platforms to investigate IRE as well as other tumor therapies.

Engineered Platforms for the Development of Electroporation-based Tumor Therapies

Elisa M. Wasson

(GENERAL AUDIENCE ABSTRACT)

Cancer is a complex and dynamic disease. Heterogeneity exists at the single cell, tumor, and patient levels making it difficult to establish a unified target for therapy. Standard therapies such as surgery, radiation, and chemotherapy often fail for this reason, therefore superior therapies must be developed. Electroporation-based therapies offer an alternative to standard treatments, utilizing pulsed electric fields to permeabilize cell membranes to either enhance drug delivery (electrochemotherapy) or induce cancer cell death (irreversible electroporation). Electroporation treatments show promise in the clinic, however, are limited in the size of tumors that they can safely treat without increasing the applied voltage to an extent that induces thermal damage or muscle contractions in patients. A method to increase ablation size safely is needed. To make this advancement and to advance other cancer treatments as well, better tumor models are needed. Many of the same challenges in treating cancer serve as challenges in creating physiologically relevant tumor models. In this dissertation, I have developed a simplified platform to test whether using a calcium additive with irreversible electroporation therapies enhances ablation size. My results demonstrate that by using a calcium additive with irreversible electroporation treatment, ablation size can be increased without using a higher applied voltage. In addition, the biological pathways responsible for cell death in irreversible electroporation treatment with and without calcium were studied. Finally, I have successfully encapsulated cells in fibrin microgels that can be used to create better tumor models that encompass the heterogeneity of tumors found in the body.

Dedication

To my family, friends, and all the young New Mexicans aspiring to become scientists.

Acknowledgments

I would like to thank my advisor, Dr. Rafael Davalos who had enough faith in me to take me into his lab and help me to become the researcher that I am today. I am truly appreciative of all of the encouragement you have given me over the past few years and your willingness to support me in all the endeavors I have taken on. Without your support, some of these opportunities would not have been possible. To my committee members, thank you for providing me with the constructive criticism I have needed to become a better engineer and researcher.

To my mentors and supervisors at Lawrence Livermore National Laboratory: Dr. Monica Moya, Dr. Elizabeth Wheeler, and Dr. Melinda Simon. I am so thankful that you accepted me to be an intern the summer of 2017 and allowed me to adopt my internship project into my dissertation. You three have provided me with such a great opportunity the last two years that have helped me grow as a person and researcher. I look up to all three of you and hope to one day be as good at science as as you all are.

To my colleagues at Virginia Tech for your support and solidarity in trying to achieve what seems, at times, the impossible. Mohammad, Nastaran, Suyashree, Andrea, Dan, Temple, Tim, Melvin, Yajun, Natalie, Alex, Adwoa, Megan, Jill, Phillip, you were all my sounding board at one moment or another, both inside and outside of the lab. To my colleagues at Lawrence Livermore National Lab: Rick, Javier, Karen, Claire, Jonathan, Elaine, and Rebecca for always making it easy to come to work and have fun all day doing science.

To my SHPE familia: Javier, Anthony, Andrea, John, Carlos, Brianna, Katrina, Adam, and Daniel.

Without you I would not have made it. You guys kept me grounded, sane, and made me feel at home in southwest Virginia. We have built lifelong friendships over the years and I cannot wait to see where we all end up.

Last, and most importantly, to my family. For all of your prayers and countless hours on the phone with me always encouraging me to keep going. Your love and support are the reason why I am where I am today. This degree belongs to you as much as it belongs to me.

Contents

List of Tables

List of Figures

Chapter 1

Introduction

1.1 The complexity of cancer

Robert Weinberg was the first to describe the "Hallmarks of Cancer" [1], a set of six traits that all cancer cells possess: self-sufficiency in growth signals, insensitivity to anti-growth signals, evasion of apoptosis, limitless replication, sustained angiogenesis, and invasion and metastasis. Despite being summarized by six traits, cancer is complex and heterogeneous at the single cell [2, 3], tumor [4], and patient levels. Through clonal evolution and genomic instability, subpopulations of cancer cells that are genetically distinct, called subclones, are formed [5]. This heterogeneity makes it difficult to establish a unified target to design effective treatments [6] and may also lead to therapy resistance [7].

In addition to evolution of the tumor cells themselves, the surrounding tissue also evolves, creating selective pressures that further drive heterogeneity and therapy resistance. The tissue surrounding tumors contain many different stromal cells such as fibroblasts, macrophages, and other immune cells [8]. These cells can be induced by cancer cells to secrete growth factors that promote tumor growth. Stromal cells often co-evolve with cancer cells as tumor progression takes place [1], diverging from their healthy phenotype. As these supporting cells diverge, the extracellular matrix

(ECM) proteins (fibronectin, collagen, laminin) as well as proteases that break down ECM, also change, and the ECM itself becomes dysregulated [8]. Changes in the ECM have been associated with different clinical outcomes in breast cancer [9].

As cancer cells proliferate, a high pressure develops inside the tumor causing blood and lymphatic vessels to become compressed, increasing interstitial pressure [10], and therefore making transport of nutrients and drugs to the tumor difficult. Due to the lack of transport, the cores of tumors are often hypoxic. It is known that hypoxia leads to radiation resistance since radiation therapy requires the production of reactive oxygen species to damage cancer cell DNA [11, 12]. For tumors to continue to grow, they must acquire angiogenic ability. Oftentimes the vessels that do develop are tortuous and leaky [13, 14] further complicating delivery of chemotherapeutics. These high interstitial pressures have also been associated with an increase in metastasis [15].

Animal models are costly and do not always adequately represent human tumor physiology, therefore better *in vitro* models are needed to test new therapeutics as they are being developed. Many of the same challenges in treating cancer, serve as challenges when building these *in vitro* models. Multiple cell types and ECM materials must be incorporated as well as a range of mechanical and chemical gradients that are key in driving tumor progression. Therefore, there is a complementary need to develop both superior cancer therapies, that overcome limitations of standard treatments, and tissue engineering technologies that can be utilized to recapitulate the heterogeneity found *in vivo* within *in vitro* tumor models.

1.2 Electroporation-based tumor therapies

Electroporation-based tumor therapies are an alternative to standard cancer treatments. Electroporation utilizes pulsed electric fields (PEFs) with high magnitudes (0.4-100 kV/cm), short durations (0.1-100 μs) and both low (1 Hz) to high frequencies (1 MHz) to destabilize cellular membranes. Pulse parameters are designed with the goal of either enhancing cancer drug delivery or inducing

cancer cell death.

When a cell is at rest, the cell membrane serves as a barrier to protect the inner contents of the cell from the outside environment and maintain the distribution of ions and molecules needed for homeostasis. The varying concentration of these charged molecules gives rise to the potential difference ($\sim$-70 mV) across the membrane known as the transmembrane potential (TMP). Under the influence of an externally applied electric field, the cell's TMP will increase (0.25-1V) and lower the energy needed for small, hydrophobic pores that form naturally in the lipid bilayer due to thermal fluctuations, to transition to hydrophilic pores [16, 17]. This electrically induced poration allows otherwise impermeable ions and molecules to enter the cell, leading to a loss of homeostasis [18].

Electroporation treatments are typically described by the pulse parameters that are applied. Amplitude, pulse width, inter-pulse delay, polarity (monopolar or bipolar), and the number of pulses, or sets of pulses (bursts) that are applied can be tuned to elicit different cellular responses (Figure 1.1).

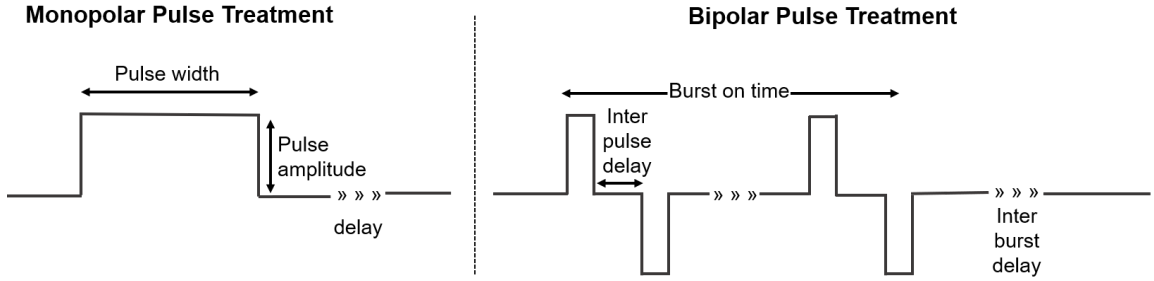

Figure 1.1: Typical pulse waveforms and parameters used in electroporation protocols to treat tumors. Electrochemotherapy (ECT) and conventional irreversible electroporation (IRE) deliver a series of monopolar pulses separated by a delay. High-frequency irreversible electroporation (H-FIRE) delivers *n* number of bipolar pulses in *m* number of bursts. Pulse parameters can be varied to exert the desired effect on cells and tissues.

When the applied electric field is below a certain energy threshold and the TMP reaches $\sim$500 mV, the pores that form in the membrane may reseal over time and the cell is able to recover [16, 19]. The cells are then said to experience reversible electroporation (RE). Taking advantage of the fact that cell membrane permeability is increased and greater molecular transport into the cytoplasm

achieved, reversible electroporation has commonly been used in gene transfection [20, 21], BBB disruption [22] and drug delivery [23]. Conversely, when the applied field exceeds a critical energy threshold and the TMP reaches a critical value ($\sim$1 mV), the pores undergo a spontaneous increase in size and the cell is unable to recover, experiencing what is termed irreversible electroporation (IRE).

Electrochemotherapy (ECT) utilizes reversible electroporation to enhance transport of cell impermeable drugs, such as the chemotherapeutic drug bleomycin, into cancer cells [24, 25, 23, 26] increasing cytotoxicity by 700 fold in a preclinical study [24]. ECT treatment typically consists of delivering 8, 100 μs pulses at either 1 or 5000 Hz using a commercially available unit called the Cliniporator® [27]. Appropriate voltages are chosen based on tumor size and tissue type. Treatments for cutaneous and subcutaneous tumors are delivered using parallel plate electrodes while percutaneous tumors are treated using needle electrodes. Chemotherapy drugs can either be injected directly into the tumor or delivered intravenously depending on tumor placement, and results in similar response of nearly 60-70% complete remission of tumors < 3 cm after one treatment [28, 29]. ECT is used clinically in the UK to treat melanoma [30], Kaposi's sarcoma [31], as well as basal and squamous cell carcinoma [32, 33]. In addition, ECT has been used to treat breast cancer metastases to the chest wall [34] as well as brain cancer [35, 36, 37], and is currently under investigation to treat pancreatic [38, 39] and liver cancer [40] in several clinical trials.

Recently, it has been shown that replacing bleomycin with calcium chloride during ECT treatments results in similar levels of cell death without the added toxicity of bleomycin, therefore potentially reducing side effects in patients [41, 42, 43] and promoting long-lasting immunity [44]. Since calcium is present at low concentrations inside of the cell, electroporating cells in the presence of calcium results in a flooding of the cell with calcium. It is hypothesized that this influx causes the cell to go into overdrive to regain homeostasis, depleting the cell of its energy (ATP), leading to cell death. [18, 41]. However, there are alternative pathways that have yet to be explored such as the effect calcium has on the production of reactive oxygen species (ROS) and lipases as well as the opening of the mitochondrial permeability transition pore.

IRE was first proposed as a tumor ablation therapy in 2005 [45]. Initially thought as an upper limit to reversible electroporation treatments, it became apparent that IRE can be used to kill tumor cells without the use of electrochemotherapy drugs [46, 47]. Treatments consist of delivering electrical pulses through needle electrodes that are inserted into the bulk tumor. The tumors are then pulsed with 80-100, monopolar, square wave pulses that are 100 μs long and delivered at a frequency of 1 Hz using a commercially available unit called the Nanoknife®. Since electrical pulses are delivered at short duration and low frequencies, there is minimal heating of tissue during treatment ensuring ablation with minimal thermal damage [48, 49, 50], unlike other ablation modalities such as radio-frequency or microwave ablation. Several preclinical studies *in vitro* and on animal patients have shown that IRE treatment results in a sharp delineation between treated and untreated tissue with submillimeter resolution [51, 52, 53], and sparing of critical structures such as vasculature [53, 54], extracellular matrix [54], and nerves [55]. IRE was FDA approved for ablation of soft tissues in 2007 and has since been used in more than 5,500 patients worldwide. IRE is currently being used in the U.S. for the treatment of pancreatic [56, 57, 58, 59] and liver [60] cancer in several pilot studies and clinical trials. Recently, it was shown that after IRE treatment, tissue surrounding the ablated tumor, experienced a decrease in expression of genes related to hypoxia (hypoxia-inducible factor 1-alpha) and increased stiffness of tumors (lysyl-oxidase) [61]. In addition, there was a transient increase in microvessel density in the tissue surrounding the treated tumor, resulting in an increase in permeability to FITC-conjugated dextran. This study demonstrated that IRE can overcome some of the obstacles that lead to treatment failure using radiation and chemotherapy discussed in section 1.1 as well as enhance the efficacy of novel therapies such as immunotherapy.

Despite the promising outcomes of IRE treatment, there are several limitations such as muscle contractions [60, 62], ablation of both healthy and malignant cells [63], as well as dependence on cell size and tissue geometry making it difficult to predict lesion size in heterogenous tissue. To address these limitations a second-generation IRE treatment was created. High-frequency irreversible electroporation (H-FIRE) is an emerging electroporation treatment that uses bipolar pulses with 1-10 μs durations delivered in a series of bursts. These bipolar pulses are delivered at higher

frequencies (kHz to MHz) and have been shown to reduce muscle contractions [64], target malignant over healthy cells [65, 66], promote systemic anti-tumor immunity [67], as well as lower the dependence of treatment outcome on cell size and tissue geometry [68, 69]. However, reducing pulse duration in H-FIRE treatment leads to a reduction in treatment volume compared to traditional IRE. This necessitates the use of much larger applied voltages to generate ablations comparable in size. Higher voltages may increase thermal damage and the likelihood of inducing muscle contractions [70, 71, 72], therefore negating some of the benefits that H-FIRE treatment has over traditional IRE.

The last class of pulsed electric fields that have been used to ablate cancer cells is called nanosecond pulsed electric fields or nsPEFs [73, 74, 75]. This treatment uses ultra short pulse widths (60-300 ns) and ultra high applied electric fields ($\sim$ 100 kV/cm). It is hypothesized that as pulse widths become much shorter than the plasma membrane charging time and the frequency of the applied electric field increases, the cell membrane conducts more of the high-frequency components of the applied field, allowing the field to reach intracellular organelles [76] and induce apoptosis [77, 78]. While there is experimental evidence that shows nsPEFs can cause intracellular calcium bursts [79, 80], the hypothesis is based on idealized computational models and no direct evidence of intracellular electroporation is currently available. nsPEFS have recently been used to treat basal cell carcinoma in a clinical trial where 7 out of 10 tumors were completely ablated, 2 were partially ablated and 1 recurred within ten weeks [81]. Although promising, nsPEF treatment requires expensive and complex waveform generator designs to produce ultra short and ultra high intensity pulses, therefore limiting its availability and use in the clinic.

Although it is generally thought that IRE causes a permanent loss of homeostasis, the exact mechanism of cell death is still being explored. It is largely thought that longer pulse widths such as those used in ECT and IRE result in necrosis of the cell while nsPEFs result in apoptosis, however there are conflicting reports in the literature [82, 83, 84]. Determining the different cell death pathways presents a challenge since there are multiple subroutines of cell death signaling within each mechanism and many overlap [85]. Adding to the complexity, cells that are located near the electrodes

will experience a higher electric field magnitude than cells further away, therefore it is believed that there may be four "zones" of electroporation: 1) small zone of cell death caused by thermal damage (Joule heating) near the electrodes, 2) medium sized zone of necrotic tissue in which cells are electroporated, lose homeostasis and are unable to recover, 3) large zone of apoptotic cell death in which defects in the membrane close, but cells are unable to recover, and 4) reversibly electroporated cells that recover and survive [18]. Despite the challenge, more fundamental research needs to be done to determine the biological effect electroporation treatments have on cells in treated tissues, specifically, uncovering the signaling pathways responsible for cell death.

Another avenue of improvement that needs to be explored in electroporation treatment is creating better *in vitro* models. A number of parameters outside of the applied pulse parameters can influence electroporation treatment outcomes such as cell size [86, 87], morphology [88, 89, 90], orientation to the electric field, and lipid composition [91, 92]. Therefore, care must be taken when selecting the method of cell culture for *in vitro* experiments. Many *in vitro* studies rely on testing electroporation treatments on cells cultured as a monolayer or in suspension, therefore, there is a need to develop and utilize simple platforms that mimic the *in vivo* treatment environment to advance electroporation treatments.

1.3 Motivation and aims

Even though ECT and IRE treatments have shown promise in ablating tumors in the clinic, they have only done so successfully in tumors that are < 4cm in diameter. To increase ablation size *in vivo*, either a higher voltage, higher number of pulses, or longer pulse width needs to be used. This results in enhanced joule heating effects which can lead to thermal damage of vital structures such as nerves and blood vessels. In addition, increasing the pulse parameters listed above can exacerbate muscle contractions and nerve stimulation which can hinder treatment success and patient recovery. Therefore, a method is needed to safely increase ablation size.

Furthermore, many *in vitro* studies rely on testing electroporation treatments on cells cultured as a monolayer or in suspension. It is well known that cell size, morphology, and membrane lipid composition affect the outcomes of treatment. Therefore, there is a need to develop and utilize simple platforms that mimic the 3D, *in vivo* treatment environment to advance electroporation treatments. *The overall objective of this dissertation is to develop and utilize simple 3D, in vitro platforms to help accelerate the understanding and development of electroporation-based tumor therapies.* These platforms will serve as a tool to advance and improve IRE treatment by studying the enhanced effect adjuvant calcium has on IRE ablations. Additionally, I have developed a tissue engineering technique that may enable the creation of more physiologically relevant and complex 3D *in vitro* and *ex-vivo* platforms to investigate IRE as well as other tumor therapies. The following work is subdivided into three aims.

Aim 1: A simplified tumor platform to study the enhanced susceptibility of glioblastoma cells to irreversible electroporation using a calcium adjuvant. *I hypothesize that combining IRE treatment with adjuvant calcium will extend treatment margins without the need for additional applied energy, therefore enhancing the safety and efficacy of IRE treatment.* This hypothesis is motivated by the fact that in a typical IRE treatment, there exists four zones of ablation: 1) thermal damage next to electrodes, 2) irreversibly electroporated zone where cells are lysed and die, 3) irreversibly electroporated zone where cells reseal, but are unable to recover from a loss of homeostasis, and 4) reversibly electroporated zone where cells survive. Calcium IRE treatment, through an influx of calcium, will induce cell death in region four, therefore extending the lesion margin. A collagen type I scaffold was used to investigate lesion size in response to calcium IRE treatment *in vitro*. Two levels of calcium (1mM and 5mM) were tested to determine dose dependence of the treatment. IRE and ECT pulse parameters were used to compare the effectiveness of both treatments. A custom algorithm was developed in MATLAB to quantify lesion area, reducing bias in measurements made by hand. In addition, a finite element simulation was developed to predict treatment volumes in brain tissue. The engineered platform developed in this chapter, allows quantification of lesion size and the electric field threshold of cell death in response to various calcium

concentrations and pulse parameters.

Aim 2: Understanding the role of calcium-mediated cell death in high-frequency irreversible electroporation. *I hypothesize that using adjuvant calcium in combination with H-FIRE will enhance lesion size in vitro.* Since a typical H-FIRE treatment consists of bipolar pulses that are 1-10 μs in duration, the TMP of the cell does not reach the critical threshold that leads to IRE ($\sim$1V) unless a larger voltage is applied. Increasing the applied voltage, in turn, leads to an increase in joule heating effects which can cause thermal damage of treated tissue. I investigated my hypothesis using the same platform that was developed in Aim 1. Collagen scaffolds were seeded with cancer cells and treated using H-FIRE waveforms with decreasing pulse widths (10, 5, 2, and 1 μs) in combination with calcium to investigate whether there is a transition towards calcium dependence for cell death. Both reversible and irreversible electroporation thresholds were quantified by measuring lesion area and calculating the corresponding electric field magnitude. Thresholds were compared to previously tested calcium IRE treatments to elucidate differences in cell death response to extracellular calcium. Finally, gene expression analysis was used to uncover the biological effects on cells in response to H-FIRE treatment with and without calcium.

Aim 3: Development of fibrin microgels for single cell analysis and tissue engineering applications. Droplet microfluidics has enabled creation of micron scale hydrogels (microgels) for single cell analysis, long-term cell culture, and tissue engineering applications. To my knowledge, fibrin microgels have not been fabricated using microfluidics previously. Fibrin has been shown to be an excellent biomaterial due to its permissive nature and degradability. *Therefore, I hypothesize that the ability to fabricate fibrin microgels in a tunable, controlled, and high-throughput fashion may enable their use for a wide range of single cell analysis studies as well as tissue engineering applications.* A flow focusing microfluidic device was used to encapsulate mammary gland cancer and endothelial cells in fibrin microgels. The efficiency of cell encapsulation was quantified and compared to the expected Poisson distribution. Viability of cells was assessed 3 days after encapsulation and a double emulsion flow-focusing device was designed and tested to keep fibrin microgels dispersed in media to enable long-term cell culture. Microgels of different materials

were created to demonstrate the versatility of this technology. Finally, fibrin microstructure was modulated using transglutaminase to control fibrin degradation in the presence of cancer cells. Fibrin microgels may enable testing of different concentrations of drugs, calcium, or microenvironments in combination with electroporation while providing a 3D environment. This technique may also allow creation of multi-material tissue models, therefore enabling *in vitro* and *ex-vivo* recapitulation of tumor heterogeneity found *in vivo*.

1.4 Outline

This dissertation is organized into six chapters. Chapter 1 has discussed how the obstacles to treating cancer also serve as obstacles in creating physiologically relevant *in vitro* and *ex-vivo* tumor models. A brief overview of the current state of electroporation treatments as an alternative to standard treatments is given, followed by outlining some limitations to IRE treatments. Finally, the aims of this project and goals to enhance both the efficacy of IRE treatments as well as the platforms used to test these therapies, are discussed.

Chapter 2 provides a review of the relevant theory of electroporation at the single cell and tissue levels. The theory describing the rise in TMP of a cell during treatment as well as pore formation in the membrane are discussed. Finally, modeling electroporation treatments in tissue is reviewed.

Chapter 3 describes the outcomes of Aim 1 and provides rationale for using adjuvant calcium with IRE treatment to enhance ablation size. A simplified tumor platform consisting of a collagen type I scaffold was utilized to allow cells to experience a 3D environment and assume a natural morphology prior to treatment. The platform also allows visualization and quantification of ablation area. A custom algorith was developed in MATLAB to automate measurement of ablation area. A finite element model was used to simulate the treatment both *in vitro* and *in vivo* to determine the electric field thresholds that result in cell death. These findings, combined with numerical modeling, make a strong case for using adjuvant calcium to increase electroporation ablations.

Chapter 4 extends the results found in the previous chapter to H-FIRE treatment. 1 mM and 5 mM $CaCl_2$ were tested in combination with H-FIRE treatments of varying pulse widths (1, 2, 5, and 10 μs). Both reversible and irreversible ablation areas and electric field thresholds were quantified for calcium and no calcium conditions. Additional mechanistic studies identified signaling pathways associated with calcium and no calcium conditions, elucidating potential cell death mechanisms.

Chapter 5 explores the development of fibrin microgels for single cell analysis and tissue engineering applications. Mouse mammary gland cancer and human brain endothelial cells were successfully encapsulated in fibrin microgels using a flow-focusing microfluidic device. Cell viability was quantified 3 days post encapsulation. A water-oil-water double emulsion was designed and tested to prevent fibrin microgels from clumping in cell culture media. Microgel microstructure was modulated using transglutaminase and microstructure effects on fibrin degrdation were studied. Microgels were also fabricated using Matrigel and a fibrin-alginate blend, demonstrating their versatility. To our knowledge, fibrin microgels have not been fabricated using microfluidics previously. In this chapter, we discuss how microgels can be utilized to incorporate heterogeneity for *in vitro* or *ex-vivo* tumor models.

Chapter 6 concludes this work with a summary of our present findings and discusses the future implications of both calcium IRE and the use of microgels for tissue engineering applications. Avenues for future work and potential challenges are discussed.

Chapter 2

Theory of electroporation

2.1 Electromagnetics

Electromagnetic theory is encompassed by Maxwell's equations which encompass the divergence and curl of the electric field **E** and magnetic field **B** as shown below.

$$\nabla \cdot \mathbf{E} = \frac{1}{\varepsilon_0}\rho \qquad \text{(Gauss's Law)} \tag{2.1}$$

$$\nabla \cdot \mathbf{B} = 0 \qquad \text{(no name)} \tag{2.2}$$

$$\nabla \times \mathbf{E} = -\frac{\partial \mathbf{B}}{\partial t} \qquad \text{(Faraday's Law)} \tag{2.3}$$

$$\nabla \times \mathbf{B} = \mu_0 \mathbf{J} + \mu_0 \varepsilon_0 \frac{\partial \mathbf{E}}{\partial t} \qquad \text{(Maxwell-Ampère's Law)} \tag{2.4}$$

where **E** is the electric field, ε_0 is the permittivity of free space, ρ is the charge density, **J** is the current density, **B** is the magnetic field, and μ_0 is the permeability of free space. Gauss's Law says that the electric flux through an enclosed surface is equal to the charge that is enclosed by that surface. Using the divergence theorem, we can rewrite the integral form of Gauss's Law in

differential form for any volume as shown in equation 2.1. The second equation (2.2) states that the divergence of the magnetic field is zero. Faraday's Law (2.3) states that a changing magnetic field induces an electric field. Likewise, from Maxwell-Ampère's Law (2.4), a changing electric field may induce a magnetic field.

While the current form of Maxwell's equations are correct, most materials are subject to electrical and magnetic polarization and contain bound charges and currents. We can rewrite Maxwell's equations in terms of the free charges, which we have direct control over since they are not inherent to the system. We can also use the constitutive relations for linear dielectric materials.

$$\mathbf{D} = \varepsilon \mathbf{E} \tag{2.5}$$

$$\mathbf{J} = \sigma \mathbf{E} \tag{2.6}$$

$$\mathbf{H} = \frac{1}{\mu}\mathbf{B} \tag{2.7}$$

where $\mathbf{D}$ is the electric displacement, ε is the permittivity of the material ($\varepsilon = \varepsilon_0(1+\chi_e)$), μ is the permeability of the material ($\mu = \mu_0(1+\chi_m)$), and $\mathbf{H}$ is the magnetic field expressed in terms of the free current of the system. Here, χ_e is the electric susceptibility and χ_m is the magnetic susceptibility. In a vacuum, there is no matter to magnetize or polarize and therefore the material's permeability (μ) becomes the permeability of free space (μ_0) and the relative permittivity or dieletric constant (ε) becomes the permittivity of free space (ε_0). Incorporating these changes into Maxwell's equations gives the following for (2.1) and (2.4).

$$\nabla \cdot \mathbf{D} = \rho_f \tag{2.8}$$

$$\nabla \times \mathbf{H} = \mathbf{J}_f + \frac{\partial \mathbf{D}}{\partial t} \tag{2.9}$$

It is possible to calculate the wavelength and the skin depth of an electromagnetic wave. The skin

depth is the distance a wave must travel before it decays by a factor of $1/e$. Since these distances are much larger than the diameter of a single cell ($\sim$10 μm), we can apply the quasi-electrostatic approximation, which assumes that the magnetic field changes slowly in time and that the electric field is irrotational ($\nabla \times \mathbf{E} = 0$). Since the curl of a gradient is always zero, we can therefore deduce that the electric field must be the gradient of some vector. It indeed is defined as the gradient of the electric potential (ϕ).

$$\mathbf{E} = -\nabla\phi \tag{2.10}$$

We can next take the divergence of (2.4) and substitute (2.10) as well as the constitutive relations for dielectric materials once again, resulting in the following equation for the quasi-electrostatic case.

$$0 = \nabla \cdot (\sigma \nabla\phi) + \varepsilon \nabla \cdot \frac{\partial(\nabla\phi)}{\partial t} \tag{2.11}$$

For standard IRE treatments, the pulse duration (100 μs) is much longer than the plasma membrane charging time ($\sim$1μs), therefore we can assume a steady-state condition and the above equation reduces to Laplace's equation.

$$0 = \nabla \cdot (\sigma \nabla\phi) \tag{2.12}$$

Laplace's equation can be solved analytically for a spherical cell with azimuthal symmetry using separation of variables.

2.2 Electroporation on a cellular level

2.2.1 Transmembrane potential development

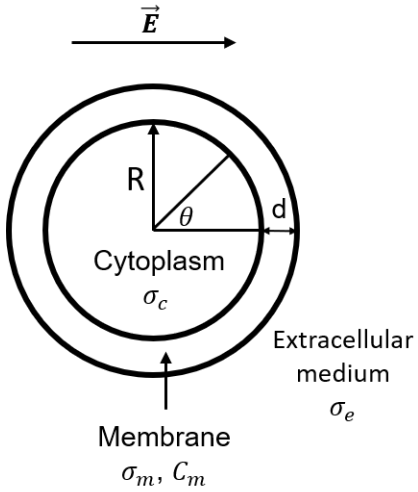

Figure 2.1: Geometric and electrical properties used to solve for the TMP in response to a homogenous electric field (E) for a spherical cell. The polar angle measured with respect to the direction of the applied field is denoted as θ. Here σ_c, σ_e, and σ_m are the conductivities of the cytoplasm, extracellular medium and membrane. The membrane capacitance is defined as C_m. Membrane thickness is denoted as d and radius of the cell R. (Adapted from Kotnik et al. 1997 [93].

Equation 2.12 can be solved analytically to obtain the voltage drop across the plasma membrane for a spherical cell exposed to an otherwise homogeneous electric field (far from electrical sources) **E** with no surface charge and constant conductivity (Figure 2.1). In this case, our system is comprised of three domains: the inside of the cell (cytoplasm), the cell membrane, and outside of the cell (extracellular medium). The plasma membrane has a thickness, d, and the radius of the cell to the inner boundary of the membrane is R. The conductivities of the cytosol, membrane, and extracellular medium are given as σ_c, σ_m, and σ_e. We assume azimuthal symmmetry which reduces Laplace's equation to two dimensions. Solving using separation of variables gives the general solution:

$$\phi(r,\theta) = A_i r + \frac{B_i}{r^2}(\cos\theta) \tag{2.13}$$

where A_i and B_i are arbitrary constants that can be determined by solving for the particular solution in each domain, r is the distance from the origin (center of the cell), and θ is the angle between the electric field and a chosen point on the cell membrane. We can now solve for the potential distribution in all domains of the cell.

$$\phi_c = A_c r + \frac{B_c}{r^2}(\cos\theta) \qquad 0 \leq r \leq R \tag{2.14}$$

$$\phi_m = A_m r + \frac{B_m}{r^2}(\cos\theta) \qquad R < r < R+d \tag{2.15}$$

$$\phi_e = A_e r + \frac{B_e}{r^2}(\cos\theta) \qquad r \geq R+d \tag{2.16}$$

To find the particular solution and solve for constants A_i and B_i in each domain i, we must apply continuity of electric potential and continuity of electric current density boundary conditions across each domain.

$$\phi_c = \phi_m \qquad at\ r = R \tag{2.17}$$

$$\phi_m = \phi_e \qquad at\ r = R+d \tag{2.18}$$

$$\sigma_c \frac{\partial \phi_c}{\partial R} = \sigma_m \frac{\partial \phi_m}{\partial R} \qquad at\ r = R \tag{2.19}$$

$$\sigma_m \frac{\partial \phi_m}{\partial R} = \sigma_e \frac{\partial \phi_e}{\partial R} \qquad at\ r = R+d \tag{2.20}$$

Since we have six unknowns, we need two more equations to fully define the problem. Due to the form of equation 2.13, we know that at $R = 0$, B_c must equal zero, otherwise the solution will approach infinity. In addition, we know that very far away from the cell ($R \to \infty$), the potential will equal the electric field ($A_e = -E$). To solve for the potential drop across the membrane we need to determine the potential distribution on both sides of the membrane first.

$$\Delta\phi = \phi_c - \phi_e = A_c r - Er - \frac{B_e}{r^2}(\cos\theta) \tag{2.21}$$

Plugging in the equations for A_c and B_e and simplifying gives a form of the Schwan equation.

$$\Delta\phi_m(R,\theta) = f_s ER\cos\theta \tag{2.22}$$

Here E is the electric field magnitude and f_s is a function representing the geometric and electrical properties of the cell.

$$f_s = \frac{3\sigma_e[3dR^2\sigma_c + (3d^2R - d^3)(\sigma_m - \sigma_c)]}{2R^3(\sigma_m + 2\sigma_e)(\sigma_m + \frac{1}{2}\sigma_c) - 2(R-d)^3(\sigma_e - \sigma_m)(\sigma_c - \sigma_m)} \tag{2.23}$$

This result provides the steady state TMP on a spherical cell when exposed to a uniform, constant electric field magnitude. From equation 2.22 it is clear to see that the TMP across the cell membrane is linearly dependent on the radius of the cell. As the radius increases, so does the TMP. In addition, the TMP will be largest at the regions of the cell closest to the anode and cathode ($\theta = 0^\circ, \theta = 180^\circ$). Typical values used to solve the model can be found in Kotnik et al. 1997 [93]. Equation 2.22 can be simplified if it is assumed that the membrane is nonconductive ($\sigma_c, \sigma_e \geq \sigma_m$) which yields the original Schwan equation.

$$\Delta\phi = \frac{3}{2}ER\cos(\theta) \tag{2.24}$$

While 2.24 provides an estimate for the TMP on a cell in the presence of an electric field, it has been shown to underestimate the value of f_s when compared to experimental results [94]. The above equations provide an equation for the steady state TMP, however, electroporation treatments utilize pulsed electric fields and therefore, the TMP is actually time-dependent. In the case of a step turn on of the electric field, the TMP can be described by the following equation.

$$\Delta\phi_m(R,\theta,t) = f_s ER\cos\theta[1-e^{-t/\tau}] \tag{2.25}$$

where τ is the time constant of the membrane.

$$\tau = \frac{RC_m}{\frac{2\sigma_e\sigma_c}{2\sigma_e+\sigma_c}+\frac{R}{d}\sigma_m} \tag{2.26}$$

Here C_m is the membrane capacitance defined as the membrane permittivity divided by the thickness of the membrane ($C_m = \varepsilon_m/d$). Here it is important to consider permittivity because of the transient nature of the solution.

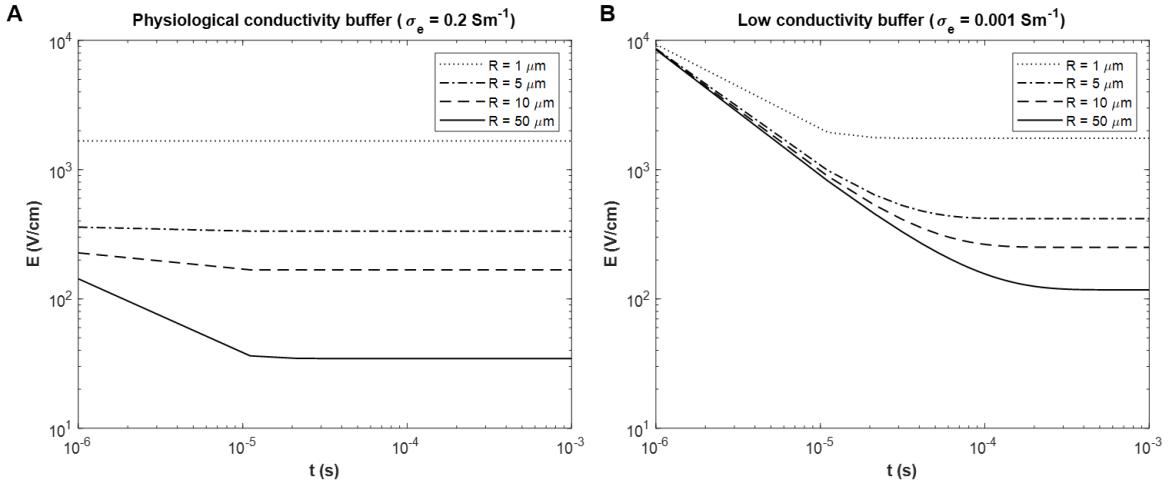

Figure 2.2: Electric field strength needed to induce electroporation as a function of pulse duration. A) Extracellular medium conductivity close to physiological value ($\sigma_e = 0.2$ Sm^{-1}). **B)** Extracellular medium with low conductivity ($\sigma_e = 0.001$ Sm^{-1}). Electroporation was considered to occur at 250 mV ($\sigma_c = 0.2$ Sm^{-1}, $\sigma_m = 5.0x10^{-7}$ Sm^{-1}, $d = 5$ nm, $C_m = 0.01$ Fm^{-2}).

Figure 2.2 demonstrates that the electric field strength needed to induce electroporation depends on pulse duration, cell radius, and conductivity of the extracellular medium. For physiological buffer, the electric field strength needed to induce electroporation decreases with increasing cell radii and stays relatively constant with pulse duration. For a low conductivity buffer however, the electric field strength is similar for all cell radii until pulse duration exceeds $\sim$10 μs. The required electric field strength to induce electroporation is much higher in a low conductivity buffer for

pulse durations less than $\sim 10\ \mu$s. A longer pulse duration ($\sim 100\ \mu$s) must be used to reduce the required electric field strength to a value comparable to when a physiological buffer is used.

Equation 2.25 and the results shown in Figure 2.2 only apply for a step turn-on of the electric field. To simulate a series of unipolar rectangular pulses and pulses that take on other shapes, this model can be expanded to analyze TMP in response to a series of step functions [87]. To do so, equation 2.22 is converted to the frequency domain by taking the Laplace Transform of the forcing function (**E**) and multiplying it by the Laplace Transform of equation 2.23. The equation describing the TMP can now be solved for in the frequency domain as a function of spectral variable s ($\Delta\phi_m(s)$). By taking the inverse Laplace Transform of $\Delta\phi_m(s)$, the equation for TMP can then be obtained in the time domain.

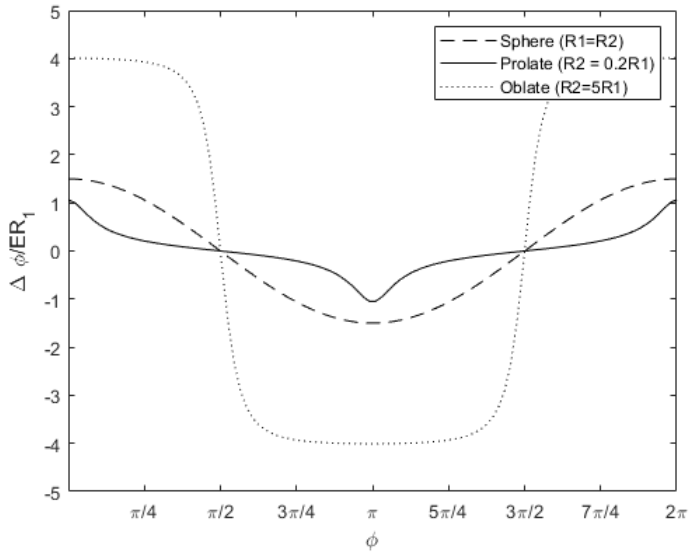

Figure 2.3: The induced transmembrane potential on a spherical cell, prolate spheroidal cell, and oblate spheroidal cell. The maximum TMP only occupies a small portion of the membrane for a prolate spheroidal cell, whereas for an oblate spheroidal cell, the max TMP occupies a majority of the membrane.

While the above mentioned models describe the TMP development on spherical cells, cells grown in 2D and 3D culture conditions will have a range of sizes and morphologies. Morphology and size can change depending on the cell type as well as the chemical and mechanical properties of the substrate the cells reside. Several analytical and numerical models have been developed to

determine the effect of cell morphology and packing density on TMP development [90, 95, 88, 96]. Kotnik et al., proposed an analytical solution for prolate and oblate spheroidal cells. To do so, it is necessary for the membrane to have a non-uniform thickness so that the geometry can be described in spheroidal coordinates. This assumption then requires that the membrane is nonconductive ($\sigma_m = 0$), meaning that the cytoplasm is perfectly shielded and has a constant potential and therefore, the TMP solely depends on the shape of the object. Figure 2.3 shows that the maximum TMP only occupies a small percentage of the membrane for a prolate spheroidal cell, whereas for an oblate spheroidal cell, the max TMP occupies a majority of the membrane. For prolate and oblate spheroidal cells, the TMP will also depend on their orientation in the electric field [95, 97]. If a prolate spheroidal cell is oriented perpendicular to the field, it will experience a much lower TMP than if it were oriented parallel to the field.

To determine the TMP on a realistic cell morphology, numerical modeling must be used. Pucihar et al., modeled the TMP of adhered Chinese hamster ovary (CHO) cells using the finite element method [96]. The cells were stained with fluorescent dye to highlight the cell's membrane and a series of images were taken in steps of 1 μm from the the bottom to the top of the cell. A 3D reconstruction was made in MATLAB and subsequently imported into FEMLAB for the finite element analysis. To avoid having to model a membrane of finite thickness which would be difficult to mesh in this case, a specific surface conductivity was assigned to the boundary between the interior and exterior of the cell. Since the conductivities of the extracellular medium and cytoplasm are much larger than the membrane, this approach is valid. By comparing the numerical model results for two CHO cells in close proximity to the analytical solution for two hemiellipsoids, it was found that the solutions differ by 10-30%. It was also found that the cells act to electrically shield each other. This effect was further modeled by Murovec et al., by calculating the TMP on a monolayer of brain endothelial cells using the finite element method [90]. It was found that an isolated cell had a larger TMP than a cell that was packed in with other cells. Additionally, the Schwan equation overestimated the TMP of the packed cell, more closely resembling that of the isolated cell's TMP. Therefore, it is important to consider the context in which cells are cultured

when studying the effects of electroporation-based treatments in vitro.

2.2.2 Pore formation dynamics

Most of the cell's structure is determined by the plasma membrane. The cell plasma membrane is composed of amphiphilic phospholipids that contain a hydrophilic head group and two hydrophobic tails. Because of their amphiphilic nature, they spontaneously form bilayers in aqueous environments which minimize the energy of the system. The bilayer structure serves to maintain homeostasis of the cell and facilitate transport of essential nutrients and molecules necessary for cell function. Nanoscale pores are regularly formed in the bilayer due to thermal fluctuations of the membrane. These nanopores create a free edge with water forming a hydrophobic pore. Once these hydrophobic pores reach a critical size (r_*), the lipid bilayer spontaneously rearranges so that the hydrophilic head groups line the pore to create an energetically favorable state (Figure 2.4 A). This reduces the surface tension and therefore reduces the energy of the system.

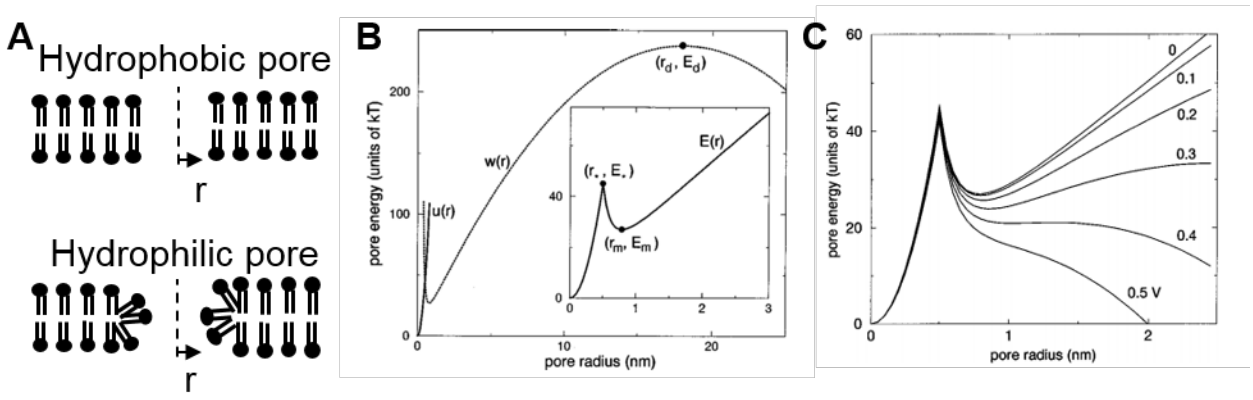

Figure 2.4: Formation of pores in the plasma membrane in response to an applied voltage. A) Thermal fluctuations naturally induce hydrophobic pore formation in the lipid bilayer. Once these pores reach a critical size, the lipids rearrange themselves to reduce the energy of the system. This creates a hydrophilic pore (Adapted from Neu et al.,[98] and Glaser et al.,[16]).**B)** Plot describing pore energy for both hydrophobic and hydrophilic pores without a transmembrane potential. **C**) Increasing transmembrane potential decreases the required energy (E_d) to expand a hydrophilic pore. Reprinted figure (B) and (C) with permission from John C. Neu and Wanda Krassowska, Phys. Rev. E, 59, 3471, 1999] Copyright (1999) by the American Physical Society.

Several continuum models using numerical techniques have been proposed to describe this phe-

nomenon and relate pore energy to transmembrane potential for electroporation applications [98, 16, 99]. The energy of hydrophobic and hydrophilic pores are given below.

$$u(r) = E_*\left(\frac{r}{r_*}\right)^2 - \pi r^2 a_p V^2 \tag{2.27}$$

$$w(r) = 2\pi\gamma r - \pi\delta r^2 - \pi r^2 a_p V^2 \tag{2.28}$$

In the first term of equation (2.27), r_* is the critical radius at which a pore transitions from hydrophobic to hydrophilic, and E_* is the energy at which this transition occurs. The second term introduces the transmembrane potential V and represents the electrical energy that motivates the transition from hydrophobic to hydrophilic where a_p is the pore specific capacitance and introduces the permittivity of the cell membrane (ε_m) and surrounding medium (ε_w) and the membrane thickness (h).

$$a_p = \frac{(\varepsilon_w - \varepsilon_m)\varepsilon_0}{2h} \tag{2.29}$$

In equation (2.28) the first term represents the pore edge energy (γ) and the second term is the membrane surface tension (δ). The constants used for these simulations are described in their respective references [98, 16]. Figure 2.4 B describes this process. For a hydrophobic pore to transition to a hydrophilic pore it must exceed a certain critical radius r_*. The minimum energy required for this transition is denoted as E_*. Beyond this radius, the pore can reach a metastable state (E_m,r_m). The expansion of a hydrophilic pore is very difficult in the absence of an elevated transmembrane potential (E_d,r_d). An increase in transmembrane potential decreases this required energy.

The above equations have been related to the distribution of pores in the membrane in response to an applied transmembrane potential providing a way to predict pore formation in response to

different applied electric fields [99]. In addition, molecular dynamics models have also been developed to describe the mechanism of electroporation and pore formation [100]. Once pores form in the membrane, transport of molecules into and out of the cell occurs, therefore disturbing the homeostasis of the cell. Based on the pulse parameters applied, the number of pores, their distribution, as well as their size can change. The larger the TMP, the more pores form and the more likely they are to merge together to form larger pores. These pores can reseal over time (reversible electroporation) or damage the cell beyond repair (irreversible electroporation). In addition to influencing pore formation, it has recently been shown that electroporation-based treatments can influence voltage gated ion channels and other structures in the membrane that influence molecular and ion transport [101].

Although it is generally thought that IRE causes a permanent loss of homeostasis, the exact mechanism of cell death in response to pore formation and transport is still largely unknown and data is conflicting in the literature. More fundamental research needs to be done to determine the biological effect electroporation treatments have on cells in treated tissues, specifically, uncovering the signaling pathways responsible for cell death.

2.3 Electroporation on a tissue level

At the tissue level, electroporation is typically delivered using two stainless-steel needle electrodes that are inserted into the tumor. One electrode is set to a specified voltage while the other serves as ground. As a result, an electric field distribution is created (Figure 2.5).

When delivering ECT, IRE and H-FIRE treatments in vivo for ablating cancerous tissues, mathematical modeling is often used to determine the pulse parameters needed to ablate the tumor while sparing healthy structures. Specifically, finite element modeling provides a powerful tool in predicting treatment margins and cell death regions for various treatment conditions. Treatment planning begins by taking magnetic resonance images (MRI) of the brain tumor and surrounding

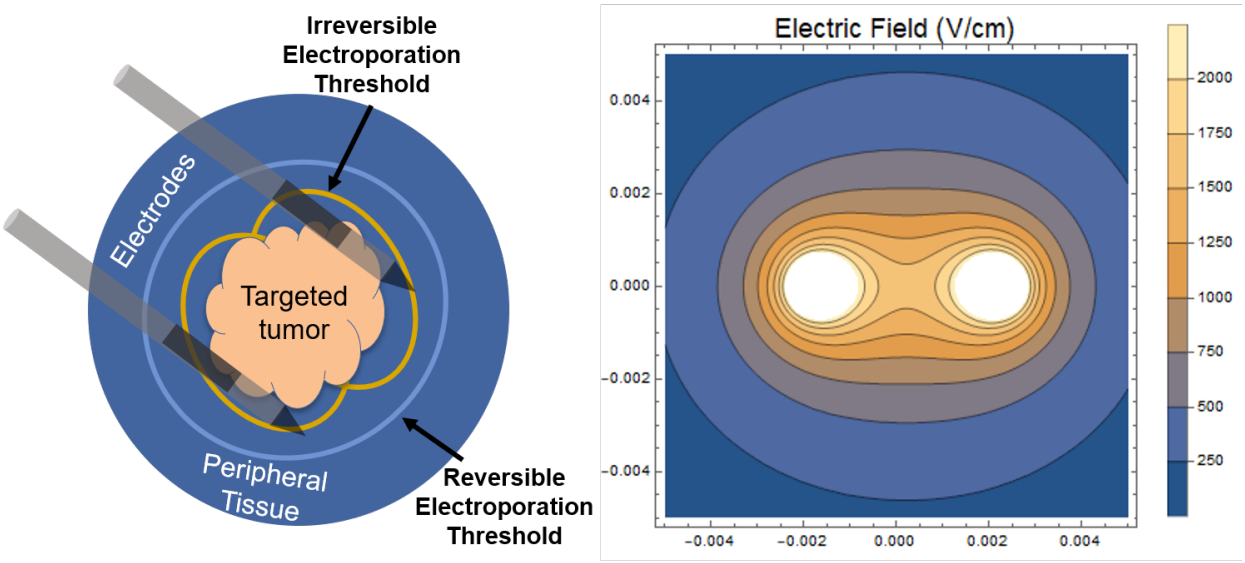

Figure 2.5: Clinical application of electroporation treatments. A) Stainless steel needle electrodes are inserted into the tumor to deliver pulsed-electric fields to the tissue. Tumor tissue will experience irreversible electroporation whereas tissue further from the electrodes experiences reversible electroporation. Numerical modeling is used to optimize treatment parameters to ensure the tumor will be adequately treated while surrounding tissue is spared. **B)** The analytical solution of Laplace's equation in an infinite 2D domain demonstrates the electric field distribution that results from two needle electrodes. The applied voltage was set to 450 V and the distance between the electrodes is 4 mm.

tissue. It is then segmented to isolate white matter, gray matter, critical structures such as blood vessels and nerves, and tumor tissue. These components are then imported into a software capable of rendering a 3D reconstruction such as OsiriX. The 3D reconstruction is then processed (holes from segmentation are filled and sharp edges smoothed) and meshed using software such as Gmsh prior to finite element analysis. Once meshed, the 3D geometry is imported into COMSOL Multiphysics (Stockholm, Sweden) and the necessary physics and material properties are applied. Simulating treatment conditions allows researchers to map the electric field distribution prior to actual treatment. Ablation volumes can be predicted using known electric field threshold values taken from previous data or in vitro experiments. This data is then used to optimize pulse parameters.

When developing a model capable of predicting treatment volumes in actual brain tissue, there are several things to consider. First, the tissue is treated as a bulk material and microscopic features are

not considered. Second, unlike the assumption made for a single cell model, tissue conductivity does not remain constant during treatment. The conductivity of tissue increases nonlinearly as it is electroporated, therefore influencing the electric field distribution [102, 103, 104]. This change is more dramatic *in vivo* than when cells are treated *in vitro* since the ratio of cell volume to extracellular fluid volume [105] is large. As cells become electroporated, the impedance of the tissue decreases, allowing current to travel through the tissue more easily. This increase in conductivity is dependent on the electric field distribution since the electric field strength dictates the extent that the tissue is electroporated. Microscopically, the electric field as well as parameters such as cell size, shape and interaction affect the transmembrane potential and therefore pore density and size in the cell membrane during electroporation. Some cells will be electroporated before others due to the parameters mentioned above, therefore a sigmoid function is used to model this nonlinear change in conductivity. As some regions of the tissue become permeabilized, the local conductivity in this region increases and regions that have not been electroporated will remain at lower conductivities. The conductivity therefore becomes heterogenous and the electric field intensity the tissue experiences will vary locally. The sigmoid curve used to describe changes in conductivity is shown below [103].

$$\sigma(E) = \frac{\sigma_1 - \sigma_0}{1 + De^{-\frac{E-A}{B}}} + \sigma_0 \tag{2.30}$$

Here σ_1 is the maximal conductivity of permeabilized tissue, σ_0 is the baseline conductivity of the tissue, and D is a sigmoid function parameter. Variables A and B depend on the irreversible threshold (E_1) and reversible threshold (E_0) and are defined as follows where C is another sigmoid function parameter.

$$A = \frac{E_0 + E_1}{2} \tag{2.31}$$

$$B = \frac{E_1 - E_0}{C} \tag{2.32}$$

These values are based upon the reversible and irreversible electroporation thresholds for brain tissue taken from experimental data in the literature. Conductivity increases by a factor of three for other organs during electroporation therefore we used this as our maximum conductivity value [103]. Joule heating in the tissue also plays a role and acts as a volumetric heat source, inducing an additional increase in conductivity. Therefore, an additional linear heating term is used when modeling thermal effects.

$$\sigma(T) = \sigma_0(1 + \alpha(T(t) - T_0)) \tag{2.33}$$

Here α, is the coefficient that describes how conductivity changes with temperature (3.2%/°C) [106] and T_0 is the initial temperature of the tissue (37°C).

When modeling electroporation treatments in vivo, we must also account for heat that is generated by the body itself. To do this, we employ the Penne's Bioheat equation.

$$\rho c_p \frac{\partial T}{\partial t} = \nabla \cdot (k \nabla T) - \omega_b c_b \rho_b (T - T_a) + q''' + \sigma |\nabla \phi|^2 \cdot \frac{d}{\tau} \tag{2.34}$$

Here ρ and c_p are the density and specific heat of brain tissue respectively, k is thermal conductivity of brain tissue, ω_b is the blood perfusion rate, c_b and ρ_b are the specific heat and density of blood, T_a is the arterial temperature (37°C), q''' is the metabolic heat generation, σ is electrical conductivity of the brain, and ϕ is electrical potential. Instead of iterating over each pulse which is computationally expensive, the total resistive heating that occurs with a treatment is determined using a duty cycle approach. This allows us to reduce computation time while still accounting for

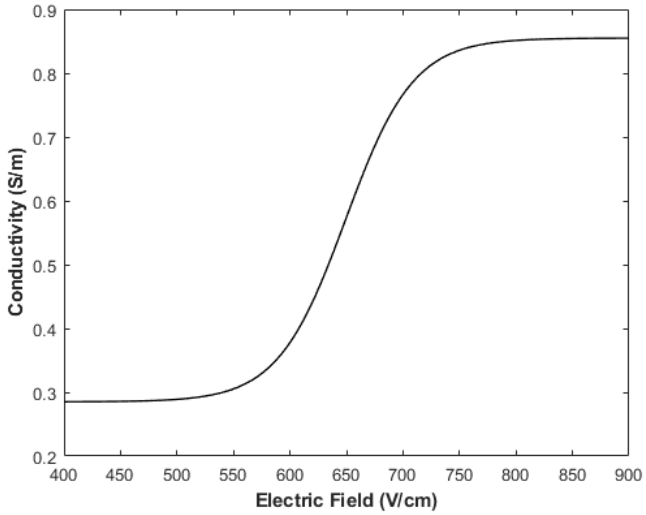

Figure 2.6: A sigmoid function is used to model the dynamic conductivity change in tissue during electroporation treatments. Conductivity increases have been measured to be $\sim$ 3x the baseline value for IRE treatment. Here baseline conductivity is 0.285 Sm^{-1} and final conductivity is 0.85 Sm^{-1}.

the heat generated during the total "on time" of the treatment. Here d is the pulse duration and τ is the pulse period. Detailed values used in these simulations can be found in Table 3.2.

In these models, we are largely ignoring the anisotropy of the brain and assuming a homogenous tissue. In the body, this is not always the case since the brain is composed of both gray and white matter. The gray matter of the brain is mostly comprised of neurons while the white matter contains myelinated axons. These axons help to distribute action potential in the brain and aid in relaying signals, but they also introduce anisotropic tissue conductivities. GBM tumors are typically located in the cortex of the brain which is the outermost layer comprised mostly of gray matter. Although tumors are mostly located in gray matter, therefore validating our homogenous assumption, it has been shown that the anisotropic conductivity can influence electric field distribution in the brain [110]. Therefore, in future studies it will be necessary to include this in our models simulating IRE and ECT treatments. In addition, although conductivity changes in response to IRE have been characterized for several organs (liver, kidney) they have not been characterized for brain tissue. The change in conductivity may differ from our proposed model, therefore this also needs to be characterized.

Table 2.1: Material properties used in numerical models to simulate vivo treatments in the brain

Material	Property	Value	Reference
Brain Tissue	Thermal conductivity (k)	0.565 $\frac{W}{mK}$	[106]
	Specific heat capacity (c_p)	3680 $\frac{J}{kgC}$	[106]
	Density (ρ)	1039 $\frac{kg}{m^3}$	[106]
	Metabolic heat generation (q''')	10437$\frac{W}{m^3}$	[107]
	Temperature coefficient (α)	0.32 C^-1	[106]
	Electrical conductivity (σ)	0.285 $\frac{S}{m}$	[106]
Blood	Specific heat capacity (c_p)	3850 $\frac{J}{kgC}$	[107]
	Density (ρ_b)	1060 $\frac{kg}{m^3}$	[108]
	Perfusion rate (ω_b)	7.15E-3	[108]
Stainless Steel Electrodes	Thermal conductivity (k)	14.9 $\frac{W}{mK}$	[109]
	Specific heat capacity (c_p)	477 $\frac{J}{kgC}$	[109]
	Electrical conductivity (σ)	2.22E6 $\frac{S}{m}$	[46]

H-FIRE treatment in tissue is a relatively new therapy and has not yet been extensively characterized. Our research group has begun to carry out these experiments by mesauring conductivity changes in response to different H-FIRE pulses for ex-vivo porcine liver [69] and rabbit kidney tissue [111]. The conductivity curves also follow a sigmoid shape and curves have been proposed for 1-5-1, 2-5-2, 5-2-5 and 10-2-10 pulses. Bhonsle et al. found that the conductivity changes during H-FIRE treatment are not as drastic as those for IRE treatment [69, 64]. Since current can travel intracellularly prior to the onset of electroporation, the total change of the impedance of the tissue will be lower than for IRE treatment [68]. This suggests that H-FIRE treatment may be more predictable in heterogenous tissues that contain anisotropy. It was shown that modeling a treatment using Laplace's equation served as a good estimate of the electric field threshold therefore tissue

geometry and overall cell size may play less of a role for H-FIRE than IRE or ECT treatment.

2.4 Conclusion

Here, we have outlined the current biophysical mechanisms and theory underlying the phenomenon of electroporation. Starting at Maxwell's equations, we arrived at the analytical expression for the transmembrane potential of a cell in response to a uniform electric field. We discussed how cell size, cell shape, as well as buffer conductivity can influence the TMP development. Next, we discussed the dynamics of pore formation in the plasma membrane in response to an applied electric field. Finally, we discussed the nonlinear conductivity changes that occur in vivo during electroporation treatments, how they are modeled and how more recent electroporation therapies may mitigate some of the challenges associated with conductivity changes. These concepts will be used to explain and discuss our experimental results in the following chapters.

Chapter 3

A simplified tumor platform to study the enhanced susceptibility of glioblastoma cells to irreversible electroporation using a calcium adjuvant

3.1 Abstract

[1] Irreversible electroporation (IRE) is a cellular ablation method used to treat a variety of cancers. IRE works by exposing tissues to pulsed electric fields which cause cell membrane disruption. Cells exposed to lower energies become temporarily permeable while greater energy exposure results in cell death. For IRE to be used safely in the brain, methods are needed to extend the area of ablation without increasing applied voltage, and thus, thermal damage. We present evidence that IRE used with adjuvant calcium (5mM $CaCl_2$) results in a nearly two-fold increase in ablation area *in vitro* compared to IRE alone. Adjuvant 5 mM $CaCl_2$ induces death in cells reversibly electroporated by IRE, thereby lowering the electric field thresholds required for cell death to nearly half that of IRE alone. The calcium-induced death response of reversibly electroporated

[1] E.M. Wasson, J.W. Ivey, S.S. Verbridge, and R.V. Davalos. The Feasibility of Enhancing Susceptibility of Glioblastoma Cells to IRE Using a Calcium Adjuvant. *Annals of Biomedical Engineering*, 45(11):2535–2547, 11 2017.

cells is confirmed by electrochemotherapy pulses which also induced cell death with calcium but not without. These findings, combined with our numerical modeling, suggest the ability to ablate up to 3.2X larger volumes of tissue *in vivo* when combining IRE and calcium. The ability to ablate a larger volume with lowered energies would improve the efficacy and safety of IRE therapy.

3.2 Introduction

Grade IV astrocytoma, also known as glioblastoma (GBM), is among the most aggressive cancers. Standard therapies such as surgical resection, radiation, and chemotherapy aim to eliminate the primary tumor in the hopes of alleviating neurological symptoms. Even with state-of-the-art treatment, the increase in median survival time is merely 14 months [112, 113].

As an alternative to standard treatments, energy-based therapies that utilize electric fields with high magnitudes (400-3000 V/cm), short durations (100 μs) and low frequencies ($\sim$1Hz) are being used to induce cell death and enhance drug delivery. These therapies rely on a phenomenon known as electroporation, which occurs when an applied electric field causes the transmembrane potential of the cell membrane to rise above a threshold limit (200-1000 mV). The rise in transmembrane potential results in the formation of nanoscale defects, allowing otherwise impermeant ions and molecules to enter. At lower voltages, this permeabilization process may allow for membrane recovery with removal of the applied field (reversible electroporation), while cell death through loss of homeostasis occurs at a higher voltage threshold (irreversible electroporation) [18].

Irreversible electroporation (IRE) has been shown to treat spontaneous gliomas in canine patients [114, 115] while sparing blood vessels and extracellular matrix [116]. An IRE treatment consists of delivering electrical pulses through two needle electrodes that are inserted into the bulk tumor [46]. Since electrical pulses are delivered at short duration and low frequencies, this causes minimal heating of the tissue, thereby ensuring ablation while mitigating thermal damage [49]. IRE treatment results in a sharp delineation between treated and untreated tissue with submillimeter res-

olution both *in vivo* [52] and *in vitro* [117], making it possible to develop finite element simulations for predicting lesion volumes before treatment.

Reversible electroporation can be achieved using lower voltage pulse parameters that cause permeabilization of the membrane, allowing molecules to enter the cell, while permitting subsequent recovery. This technique has been used in gene transfection [107], blood-brain barrier disruption [22] and drug delivery [23]. Electrochemotherapy (ECT) utilizes reversible electroporation to enhance transport of cell impermeant chemotherapy drugs [23], which has shown to be effective in treating brain tumors [35, 108, 118].

Because ECT uses lower applied electric field magnitudes and fewer pulses than IRE [119], and the extent of electroporation largely depends on pulse duration and number [120], the zone of treatment is limited. IRE is more versatile, enabling control of the ablation zone in tissue. IRE is effective as a stand-alone therapy for ablating the primary tumor without the need for chemotherapy drugs, yet still induces reversible electroporation further away from the electrodes, making cells susceptible to adjuvant therapies. Neal et al., confirmed a 2-3X larger zone of cell death *in vitro* using IRE treatment in combination with chemotherapeutic drugs compared to IRE treatment alone [121].

Our hypothesis is that IRE efficacy may be improved when combined with adjuvant calcium, for a treatment that is safer than combined treatment with chemotherapeutics. This hypothesis is motivated by results which demonstrate that ECT pulses used in conjunction with calcium cause more cell death and a greater decrease in cellular ATP than electroporation alone [41]. Frandsen et al., hypothesized that this may be due to ATP depletion resulting from calcium ATPase pumps in the plasma membrane going into overdrive to pump calcium out of the cell, although further investigation is needed to confirm this mechanism and rule out others.

The motivation for adjuvant calcium combined with IRE is based on the knowledge that electric field magnitude during an IRE treatment decreases as you travel away from the electrodes. A high electric field magnitude will develop close to the electrodes (irreversible electroporation) and a low electric field magnitude far from the electrodes (reversible electroporation). Cells in the irreversibly

electroporated zone will die through loss of homeostasis resulting from electroporation, while the influx of calcium will exacerbate cell death in the reversibly electroporated zone. Calcium IRE may accentuate the treatment margin without applying additional energy. Furthermore, it may provide an advantage over microwave and radiofrequency ablation since the mechanism is non-thermal and spares vital structures. Though efforts have been made to extend the margin of energy based treatments, to our knowledge, we are the first to investigate IRE pulses in combination with calcium.

To test our hypothesis, we cultured glioblastoma cells in 3D collagen scaffolds and tested ECT and IRE pulses in combination with two concentrations of $CaCl_2$ solution. The electric field thresholds calculated from *in vitro* results were then used to inform a numerical model that simulates an *in vivo* treatment with the purpose of predicting treatment volumes. These results suggest that using IRE with a calcium adjuvant enhances lesion size without increasing thermal damage.

3.3 Materials and Methods

3.3.1 Cell culture

U251 malignant glioma (MG) cells (Sigma Aldrich) were cultured in Dulbecco's Modified Eagle Medium (Life Technologies) containing 10% fetal bovine serum (Atlanta Biologicals), 1% penicillin/streptomycin (Life Technologies) and 0.1% non-essential amino acids (Life Technologies). Cells were routinely passaged at 70-90% confluence and kept in a humidified incubator at 37°C and 5% CO_2. Prior to fabricating the 3D collagen scaffolds, cells were removed from their flask using trypsin (Life Technologies) and centrifuged at 120g for five minutes. Cells were re-suspended in fresh medium and added to the collagen solution for a final concentration of $1x10^6$cells/mL.

3.3.2 Collagen scaffold fabrication

3D cell cultures are now recognized as more appropriate tumor models than 2D monolayer cultures [122]. This technique has been used previously by Arena et al. [117] and Ivey et al. [65] to study the effects of IRE on different tumor cell lines using similar matrix composition and stiffness. Concentrated collagen stock solutions (10 mg/mL) were created using rat tail collagen type I as described previously [123]. While the brain consists of relatively low amounts of fibrous proteins, collagen provides a convenient scaffold material that produces relevant 3D geometry, integrin engagement with surrounding extracellular matrix, and appropriate cell-cell interactions. Collagen stock solution was mixed with 10X DMEM (10% of total solution volume) and 1N NaOH (2% of total collagen volume) until homogenous and adjusted to obtain a pH of 7.0-7.4. Cells in media were mixed into the collagen solutions to produce a final collagen concentration of 5 mg/mL. Collagen was injected into Polydimethylsiloxane (PDMS) wells of controlled geometry (10 mm diameter, 1 mm height) to ensure uniformity of the electric field distribution across experiments. Injected collagen was molded flat in the PDMS wells and placed in the incubator to polymerize at 37 °C and 5% CO_2 for 20 minutes. Fresh media was added to the wells and they were cultured in the incubator for 24 hours before treatment. The electrical conductivities of the gel-cell mixtures were measured with a conductivity meter to ensure similar electrical properties. Collagen hydrogels without cells had a conductivity of 1.08 $\pm$ 0.06 S/m (n=4). Collagen hydrogels with cells seeded in the bulk had a conductivity of 1.17 $\pm$ 0.08 S/m (n=4).

3.3.3 Electroporation protocol

Concentrations of 1 mM and 5 mM $CaCl_2$ were used in our study to determine the effect of a range of $CaCl_2$ concentrations on lesion size *in vitro*. These concentrations have shown effect on cell viability [41]. Media was aspirated from each well and a concentration of 1 mM or 5 mM $CaCl_2$ in HEPES buffer was added for 30 min at room temperature to ensure complete diffusion into the collagen scaffold. Calcium solutions were then aspirated from each well and scaffolds washed

with new $CaCl_2$ solution to ensure all cell culture media had been replaced. Fresh calcium solutions were added immediately prior to pulsing. A control solution of NaCl in HEPES buffer was used, as it has similar conductivities and osmotic concentrations to the $CaCl_2$ solutions (Table 3.1). All solutions were within the isotonic range of 260-320 mOsm/L and had pH values between 7.0-7.2 to better emulate a slightly acidic tumor microenvironment [124, 125, 126]. Sham treatments were carried out by adding the NaCl and $CaCl_2$ solutions to each well and inserting the electrodes without pulsing.

Table 3.1: Properties of solutions used in experiment

Concentration	Solution	Conductivity (S/m)	Osmolarity (mOsm/L)
1 mM	$CaCl_2$	0.053 ± 0.017	276.52 ± 2.12
	NaCl	0.106 ± 0.026	282.5 ± 3.53
5 mM	$CaCl_2$	0.078 ± 0.005	288.0 ± 9.90
	NaCl	0.122 ± 0.009	290.5 ± 4.95

Hollow stainless steel, blunt tip needles (Howard Electronic Instruments) with diameters 0.914 mm (OD) and 0.635 mm (ID) were used as electrodes. A custom-made part housed the electrodes to ensure uniform spacing (4 mm center-to-center) and placement in each collagen scaffold (Figure 3.2A). IRE pulses were delivered using an ECM 830 pulse generator (Harvard apparatus) and consisted of eighty 450 V pulses, frequency of 1 Hz and pulse duration of 100 μs. ECT pulses consisted of the same parameters except eight pulses were delivered. After treatment, $CaCl_2$ and NaCl solutions were removed from each well, replaced with cell culture media and the well plate was returned to the incubator.

3.3.4 Determining area of cell death in collagen scaffolds

Scaffolds were kept in the incubator for 24 hours after treatment. It has been reported that this is sufficient time to allow transient pores formed in the cell membrane to recover [127] and evaluate

the effects of calcium electroporation [41, 43]. Scaffolds were incubated with 2 μM Calcein AM (Invitrogen) and 15 μM propidium iodide (Life Technologies) in PBS for 30 minutes at room temperature. Calcein AM labels living cells green while propidium iodide labels cells lacking membrane integrity red. Images were taken of each well using an inverted DMI 6000B microscope (Leica Microsystems) with a 5x objective. A custom algorithm developed in MATLAB was used to measure lesion area, descibed below.

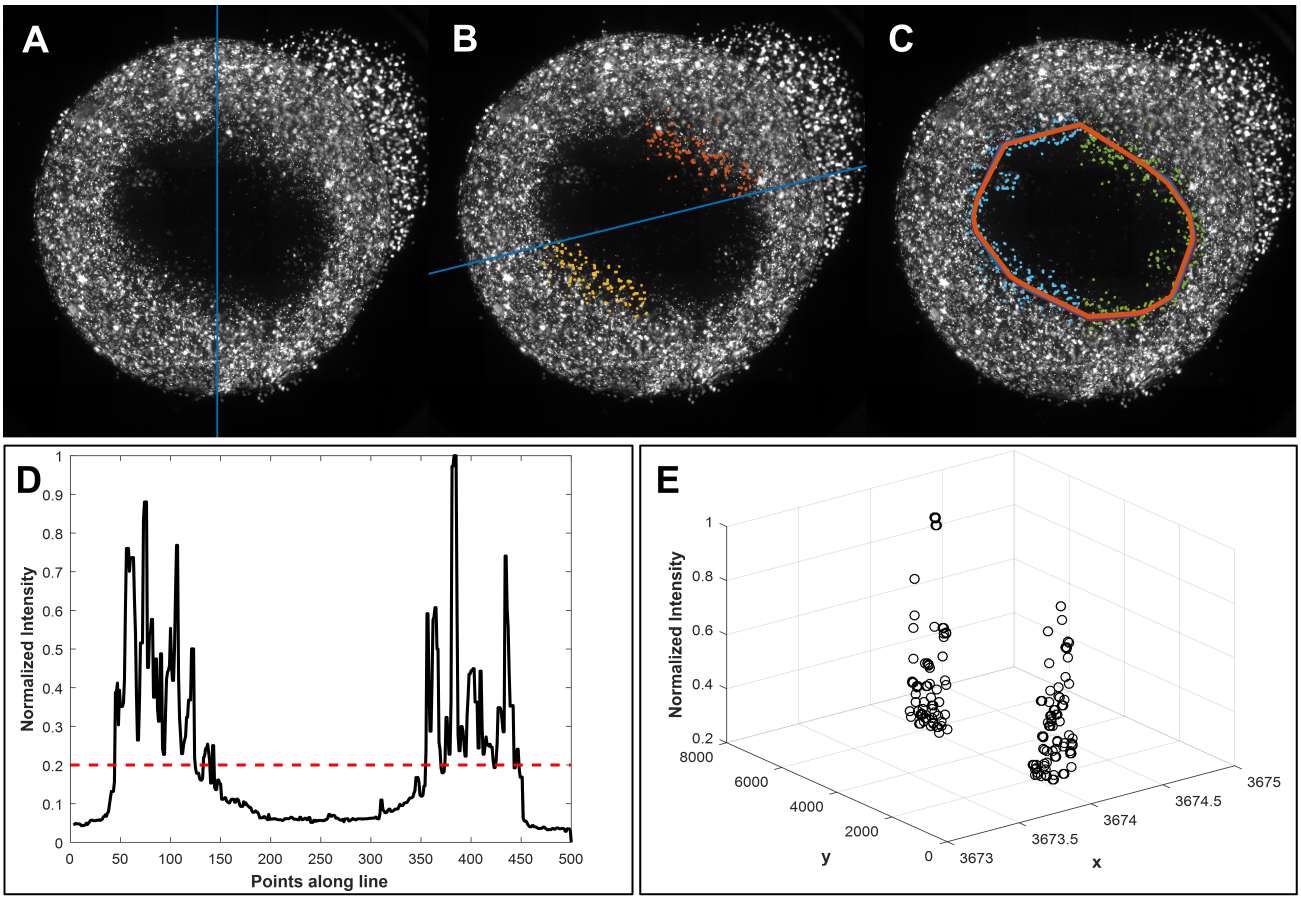

Figure 3.1: Sweeping a line ROI across an experimental image and analyzing intensity values along this line determines lesion area. **A)** Line ROI at = 0° **B)** Line ROI at = 76° **C)** Convex hull operation encloses the points, eliminating the electrodes from the measurement. The convex hull and least squares iteration can eliminate any outliers and converge on an area. **D)** Normalized intensity values along the line at = 0° (shown in A). A 20% threshold is used to separate live and dead regions. **E)** Plotting the values that are above the set threshold (live region) highlights the lesion length along the line. This gap in intensity values is used to find the coordinate points that outline the boundary of the lesion.

The green channel of images was used for analysis since intensity was more apparent. Contrast of

the images was enhanced using the imadjust command to highlight differences between live and dead regions. A line region of interest (ROI) was plotted directly on the image and swept through various angles to analyze the image in increments of 0.5 degrees (Figure 3.1A). A total of 720 points (360/0.5) were used to accurately define the lesion boundaries. Intensity values along each respective line were analyzed.

First, background intensities on the upper left corner of each image were averaged and subtracted from all intensity values calculated along the line to shift intensity down to a baseline level, making it easier to apply a threshold. The intensity values were smoothed using a median filter and were then normalized to the maximum intensity value, giving a range between zero and one (Figure 3.1D). This resulted in two peaks where the line crosses regions of high intensities (live region) and a region of low intensities where the lesion was located. Setting a threshold based on 20% of the maximum intensity value was chosen ($I > 0.2$) since this successfully separated the live and dead regions for all images.

Plotting the coordinate points that lie above the threshold (live region) versus their respective intensity values, reveals a gap in values (Figure 3.1E). We performed a difference operation on the vector of coordinate points which provided the change in distance sequentially from point to point. The maximum of this difference indicated the length of the gap (i.e. our lesion). The (x,y) coordinates at the beginning and end of this gap were plotted over the experimental image for each line therefore tracing the perimeter of the lesion (Figure 3.1B).

The region inside of the plotted coordinate points was enclosed using a convex hull operation which eliminated the electrodes from the measurement. The convex hull operation also served to remove outliers in the coordinate points that might skew the area measurement since it returns the point indices that define the hull (Figure 3.1C). An iterative process was used to remove outlier coordinate points using the convex hull operation and then smooth the distribution of points using a Savitzky-Golay filter. This filter utilizes least squares fitting to fit successive data points to a low order polynomial. This resulted in an iterative process which would converge when the change

in area of the enclosed fit of points differed by less than 6% for two consecutive iterations. This criterion was chosen because some images contained a considerable number of outliers. Initially, the change in area between successive iterations decreased, but as outliers were eliminated from subsequent measurements, the change in area increased. A change in area of less than 6% was sufficient to accurately determine lesion area while also avoiding errors due to insufficient points available for the convex hull operation. The final resulting area of the enclosed region was calculated using polyarea, a built-in MATLAB function. The code successfully measured 80% of experimental images. Because of artifacts such as bubbles that form in the collagen, the remaining were measured by hand. Figure 3.1C demonstrates the accuracy of the MATLAB image processing code to detect the boundaries of cell death after treatment using IRE and 1 mM $CaCl_2$.

3.3.5 Numerical model of electric field distribution in collagen scaffolds

The electric field distribution in the collagen scaffolds was determined using finite element analysis (COMSOL Multiphysics 5.2, Burlington, MA). The finite element model consisted of a cylinder to represent the scaffold, and two stainless steel cylinder electrodes as described above. We are able to use the quasi-electrostatic approximation since the pulse duration is much larger than the charging time of the plasma membrane. As shown previously by Arena et al. [117], the conductivity of the scaffolds is assumed constant since the concentration of cells we are using in our collagen scaffolds is not high enough to induce a change in bulk conductivity that significantly affects electric field distribution during electroporation. In addition, temperature increase due to electroporation in collagen scaffolds using similar pulse parameters and bulk conductivities was not sufficient to cause thermal damage, therefore we neglected heating effects in our current study. This reduced our governing equation to Laplace's equation.

$$0 = \nabla^2 \phi \tag{3.1}$$

where ϕ is electric potential and the electric field can be described as $\mathbf{E} = -\nabla\phi$. The surface of one electrode was considered charged ($\phi = 450\ V$), one grounded ($\phi = 0\ V$) and the remaining boundaries defined as electrically insulative ($\partial\phi/\partial n = 0$). The mesh was refined until there was less than a 2.0% change in the electric field magnitude at the surface of the collagen scaffold between the electrodes. The extra fine mesh used in the studies consisted of 103,297 tetrahedral elements.

3.3.6 Determining the cell death electric field threshold

The numerical model of the electric field distribution in the collagen scaffold was integrated along its surface to determine the affected area for a range of electric field thresholds. Values close to the boundaries of the collagen scaffold were eliminated from the curve fit since these areas were not relevant to our measurements. A relationship between lesion area and electric field magnitude was determined using least squares fitting resulting in a sixth order polynomial equation (Figure 3.5). The cell death threshold for each experimental condition was calculated using this equation.

3.3.7 Numerical model to simulate lesion volumes in the brain

A simplified finite element model of the brain was created using COMSOL Multiphysics 5.3 to simulate the increased lesion size that would occur in vivo using IRE and calcium. The brain was modeled as a 3D domain with dimensions sufficiently large to mitigate any boundary effects that may influence lesion size and shape (12 cm X 12 cm X 12 cm). This assumption provided us with an ideal case to separate the effectiveness of treatment from any influences geometry and boundary conditions may have on lesion size. Two stainless steel, cylinder electrodes (1 mm diameter), spaced 2.0 cm apart (center-to-center) with a length of 1.5 cm were inserted into the center of the 3D domain. The governing equation that determines potential distribution in a material is defined below:

$$0 = \nabla \cdot (\sigma \nabla \phi) \tag{3.2}$$

Here, ϕ is electric potential and σ is the electrical conductivity of the brain. We were unable to assume constant conductivity since it has been shown that conductivity of tissue increases more dramatically after electroporation than cells in suspension due to the large ratio of cell volume to extracellular fluid volume [105]. As the cells are electroporated, resistance of the tissue decreases as there are more paths for current to travel. Joule heating effects also increase conductivity and act as a volumetric heat source. To model this change in conductivity, we employed a smoothed Heaviside function that is dependent on electric field [114]. We can indirectly relate the change in conductivity to the applied electric field since the extent to which the tissue is electroporated depends on this magnitude. Conductivity also depends on the change in temperature that occurs in the tissue, so an additional linear heating term is used. Here α, is the coefficient that describes how conductivity changes with temperature (3.2%/°C) [106] and T_0 is the initial temperature of the tissue (37°C). To ensure the solution will converge, we smoothed the function using a continuous second derivative. The function used to define conductivity is shown below as it was written in COMSOL.

$$\sigma(E,T) = \sigma_0[1 + 2 \cdot flchs(E_{norm} - E_{delta}, E_{range}) + \alpha(T - T_0)] \tag{3.3}$$

Here E_{norm} is the magnitude of the electric field, E_{range} is the range over which the function transitions (± 120 V/cm), E_{delta} is the electric field value at which this transition occurs (580 V/cm) and σ_0 is a baseline conductivity value for grey matter (0.285 S/m) [106, 114]. In using this function, we assumed that conductivity increases by a factor of three since this was reported for other organs during electroporation [103]. We must also account for metabolic heat generation, conduction, and convection due to blood perfusion. We included the Penne's Bioheat equation with a modified Joule heating term to account for resistive losses [128].

$$\rho c_p \frac{\partial T}{\partial t} = k\nabla^2 T - \omega_b c_b \rho_b (T - T_a) + q''' + \sigma |\nabla \phi|^2 \cdot \frac{d}{\tau} \tag{3.4}$$

Here ρ and c_p are the density and specific heat of brain tissue respectively, k is thermal conductivity of brain tissue, ω_b is blood perfusion rate, c_b and ρ_b are the specific heat and density of blood, T_a is the arterial temperature (37°C), q''' is the metabolic heat generation, σ is electrical conductivity of the brain, and ϕ is electrical potential. We approximated the total resistive heating that occurs with a treatment using a duty cycle approach, as opposed to iterating over each pulse, to reduce computation time while still accounting for the heat generated during the total "on time" of the treatment. Here d is the pulse duration (50 μs) and τ is the pulse period (1 s).

Table 3.2: Material properties used in the *in vivo* numerical model of the brain

Material	Property	Value	Reference
Brain Tissue	Thermal conductivity (k)	0.565 $\frac{W}{mK}$	[106]
	Specific heat capacity (c_p)	3680 $\frac{J}{kgC}$	[106]
	Density (ρ)	1039 $\frac{kg}{m^3}$	[106]
	Metabolic heat generation (q''')	10437 $\frac{W}{m^3}$	[107]
	Temperature coefficient (α)	0.32 C^-1	[106]
	Electrical conductivity (σ)	0.285 $\frac{S}{m}$	[106]
Blood	Specific heat capacity (c_p)	3850 $\frac{J}{kgC}$	[107]
	Density (ρ_b)	1060 $\frac{kg}{m^3}$	[108]
	Perfusion rate (ω_b)	7.15E-3	[108]
Stainless Steel Electrodes	Thermal conductivity (k)	14.9 $\frac{W}{mK}$	[109]
	Specific heat capacity (c_p)	477 $\frac{J}{kgC}$	[109]
	Electrical conductivity (σ)	2.22E6 $\frac{S}{m}$	[46]

For treatments in the brain, it is preferred to use 50 µs pulses as opposed to 100 µs to mitigate

thermal damage [114]. The surface of one electrode was treated as energized, one grounded, and remaining boundaries as insulated. 3000 V was simulated giving an applied electric field magnitude of 1500 V/cm which is typical of IRE treatments delivered in the brain [114, 115]. 1000 and 2000 V were also tested to establish a relationship between applied voltage and lesion volume. All boundaries were treated as thermally insulative ($\partial T/\partial n = 0$) to account for the case of maximum heating in the tissue. Material properties were defined as stainless steel for the electrodes and grey matter for brain tissue (Table 3.2). Standard IRE and ECT treatment were simulated in the numerical model of the brain and the electric field contour corresponding to its in vitro treatment threshold was located. The volumes within these boundaries were numerically integrated. It was assumed that homogenous concentrations of $CaCl_2$ and NaCl solutions would be achieved in vivo. The mesh was refined until there was less than a 2.0% change in calculated volumes.

3.3.8 Statistical analysis

All IRE, ECT, and sham conditions were tested ten or eleven times (n = 10, n = 11) as determined by a power analysis. The discrepancy between these repetitions resulted from collagen detachment during treatment. Statistical analyses were performed with a confidence level of $\alpha = 0.05$ (JMP Pro 13). Two-way ANOVA was used to test for differences in cell death area and cell death threshold. Tukey post-hoc comparisons were used to examine differences among treatment groups. Results are shown as arithmetic means ± standard deviation.

3.4 Results

3.4.1 Experimental setup and numerical model simulating IRE pulses in collagen scaffolds

Figure 3.2 shows our experimental platform. The electrode housing enabled precise positioning of electrodes into the collagen scaffold, eliminating variability that may occur in the electric field distribution due to varying exposure lengths or boundary effects if the electrodes were not centered.

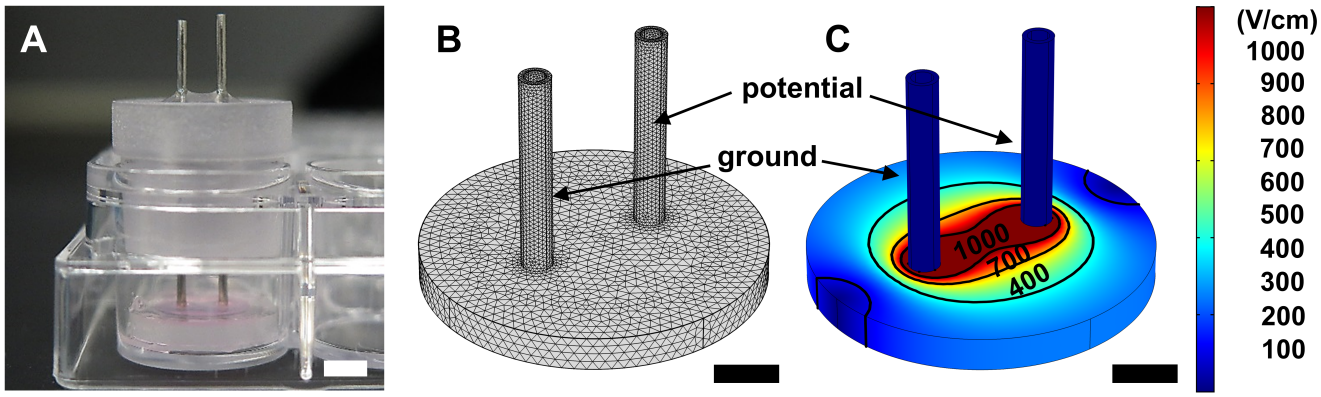

Figure 3.2: Calcium IRE experimental setup. **A)** Custom made electrodes inserted into the collagen scaffold platform prior to pulsing with electrode spacing of 4.0 mm (scale bar 4 mm). **B)** Geometry of the finite element model used to simulate treatment of the hydrogel platform (scale bar 2 mm). The extra fine mesh consisted of 103,297 tetrahedral elements. **C)** Electric field distribution in the scaffold after an IRE treatment (450 V, 1 Hz, 100 μs pulse width, 80 pulses) showing the region of collagen affected by different electric field thresholds (scale bar 2 mm).

Our numerical model was used to predict the field distribution in the collagen scaffolds during a typical treatment. The experimental platform enabled us to visualize a range of electric field magnitudes as opposed to a single value that is applied when testing cells in suspension using plate electrodes (Figure 3.2C). This represents what occurs in vivo during a typical IRE or ECT treatment since cells in the tumor will experience a gradient of field magnitudes depending on their distance from the electrodes. For ECT treatments, reversible electroporation occurs at an electric field magnitude around 300 V/cm whereas IRE occurs above 500-600 V/cm [107]. In our numerical model of the collagen scaffolds, these zones can be distinctly visualized. By bounding regions of

different electric field magnitudes using a contour plot, the model allowed us to determine the field threshold that causes an equivalent area of cell death for each of our treatments. This highlights our ability to precisely predict ablation sizes.

3.4.2 Experimental results

Our experimental results confirmed our hypothesis that calcium IRE results in larger lesions than IRE alone. Sham treatments resulted in no cell death therefore confirming that the $CaCl_2$ and NaCl solutions themselves do not affect cell viability (Figure 3.3). Similarly, treating with ECT pulses and NaCl solutions did not result in cell death. Due to the small number of pulses used in an ECT treatment, the cells become permeabilized, but subsequently recover.

On the other hand, when we applied IRE pulses in the presence of NaCl solutions, we see a small region of dead cells formed in the collagen scaffold. This area experiences a higher electric field magnitude for a longer duration of time, therefore electroporating the cells to a greater extent and rendering them incapable of recovering.

Since NaCl and $CaCl_2$ solutions have comparable conductivities, it can be concluded that the larger lesions observed for $CaCl_2$ treatments are due to the action of calcium and not additional heating effects that may occur due to the conductivities of our buffer solutions.

It should be noted that in some of our experimental images, the propidium iodide staining is difficult to see. This effect has also been seen in previous experiments using the same platform [65] and although the exact mechanism is not known, it seems as if the cells may be broken up and are unable to take up and maintain the dye 24 hours after treatment. Since Calcein AM only fluoresces when in the presence of intracellular esterases, we can conclude that cells in the dark region are dead and those stained green with Calcein AM are alive.

Combining all area measurements from the image processing algorithm shows that 1 mM and 5 mM $CaCl_2$ treatments lead to an increase in lesion size of nearly double that of their respective

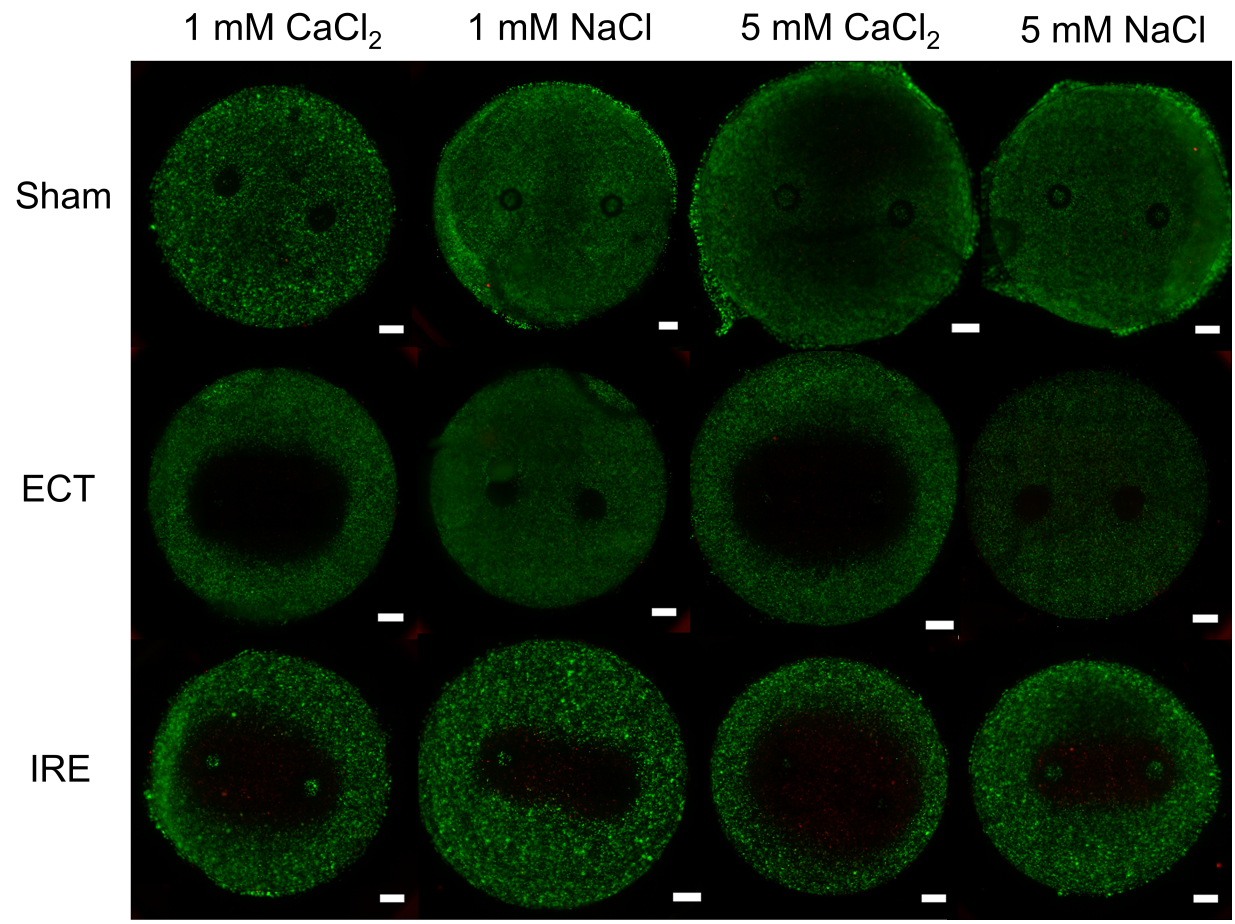

Figure 3.3: $CaCl_2$ treatments produce larger cell death lesions than NaCl controls for both IRE and ECT pulses (scale bar 1mm). Collagen scaffold experiments consisted of 4.0 mm electrode spacing, 100 μs pulse width, 1 Hz frequency and 450 V. IRE treatments were delivered with a total of 80 pulses (n = 11) while ECT treatments were delivered with 8 pulses (n = 11,n =10). 24 hours after treatment, hydrogels were stained with Calcein AM (stains live cells green) and propidium iodide (stains dead cells red).

NaCl controls when using IRE pulses (Figure 3.4). The 1 mM $CaCl_2$ treatment combined with IRE, resulted in an average lesion area of 25.1 $\pm$ 3.9 mm^2 whereas its NaCl control resulted in an average lesion area of 14.4 $\pm$ 2.9 mm^2. Combinatorial treatment using 5 mM $CaCl_2$ solution with IRE resulted in an average lesion area of 32.5 $\pm$ 2.0 mm^2 whereas 5 mM NaCl combined with IRE resulted in an average lesion area of 13.2 $\pm$ 3.6 mm^2. Comparing 1 mM $CaCl_2$ and 5 mM $CaCl_2$ concentrations in combination with IRE resulted in a significant difference in lesion area. There was no significant difference between 1 mM NaCl and 5 mM NaCl treatments (p = 0.9553).

For ECT pulses, it is evident that calcium treatments also had a significantly larger lesion area than

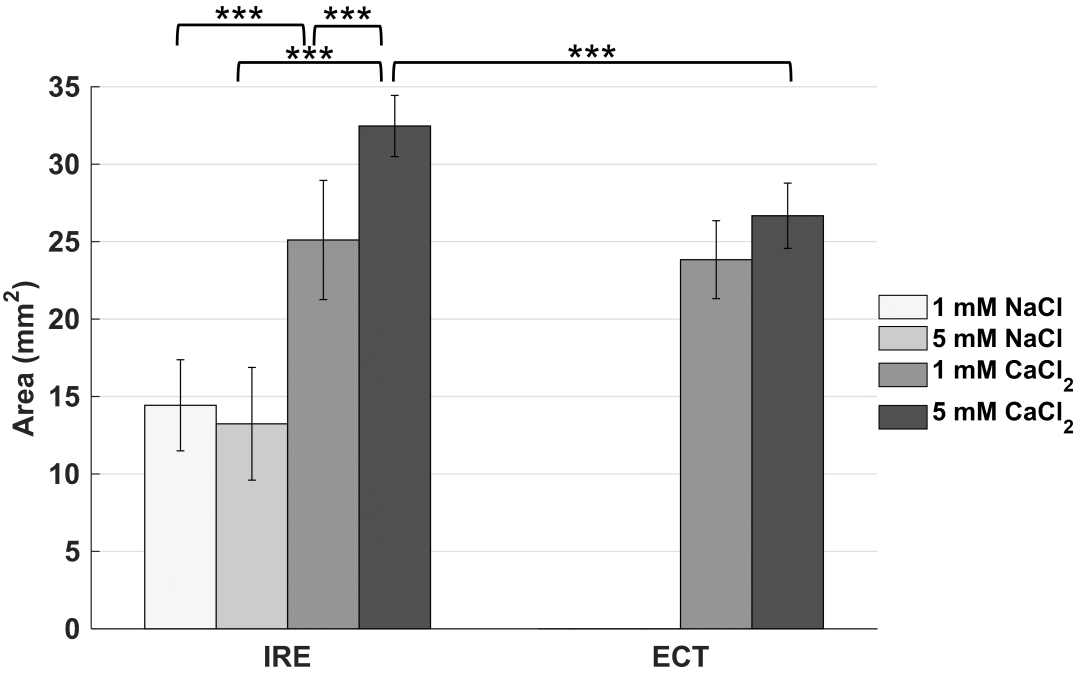

Figure 3.4: Lesion sizes measured in collagen scaffold experiments demonstrate that $CaCl_2$ treatments lead to significantly larger lesion sizes than their NaCl controls. Collagen scaffold experiments consisted of 4.0 mm electrode spacing, 100 μs pulse width, 1 Hz frequency and 450 V. For IRE treatments, 80 pulses were delivered while for ECT treatments, 8 pulses were delivered. Scaffolds had a total area of 78.54 mm^2 and thickness of 1 mm. U251 MG cells were seeded at a concentration of $1x10^6$ cells/mL. ECT treatments with NaCl solutions are not shown due to no lesion being present. (***p<0.0001).

their NaCl controls for both 1 mM $CaCl_2$ and 5 mM $CaCl_2$. Lesion areas were not significantly different for 5 mM $CaCl_2$ and 1 mM $CaCl_2$ treatments (p = 0.1926). Data for both NaCl concentrations are not shown in figure 3.4 for ECT treatments since these pulses did not result in a lesion and were treated as having zero area.

When comparing ECT pulses to IRE pulses, for the 1 mM $CaCl_2$ solution, there was no significant difference between lesion areas (p = 0.9451) whereas for the 5 mM $CaCl_2$ solution, there was a significant difference. As mentioned previously, an IRE treatment of 80 pulses leads to an average lesion area of 32.5 ± 2.0 mm^2, whereas an ECT treatment of eight pulses lead to an average lesion area of 26.7 ± 2.1 mm^2 for the 5 mM $CaCl_2$ solution.

3.4.3 Calculating electric field threshold required for cell death

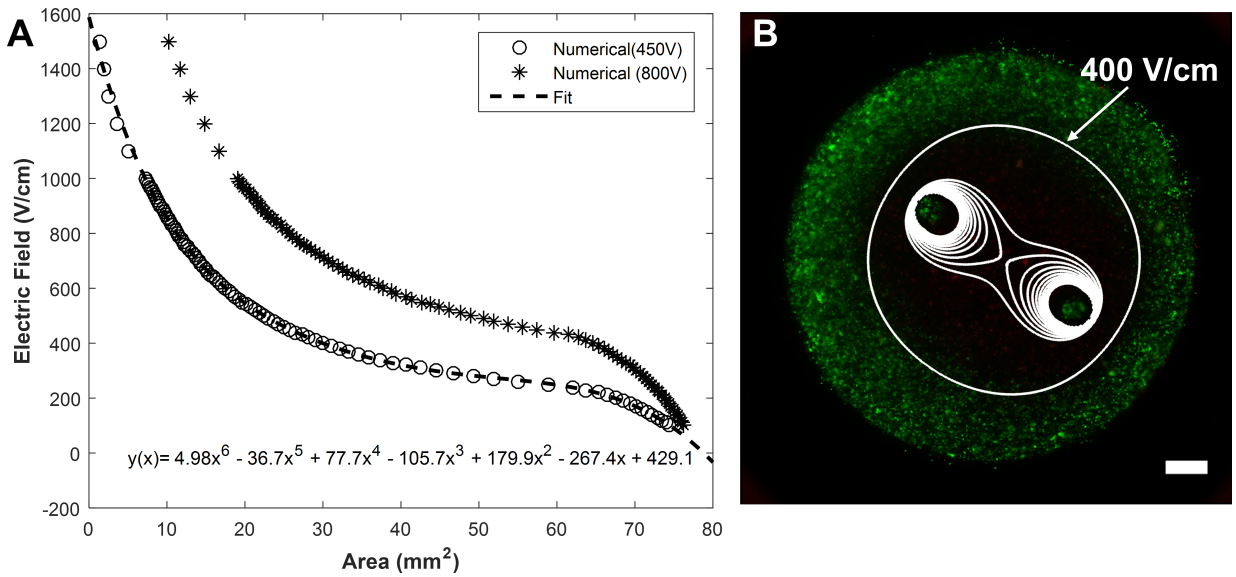

Figure 3.5: The numerical model of the experimental setup is used to determine the area of collagen exposed to various electric field thresholds for applied voltages of 450 V and 800 V. A) Numerically integrating the finite element model of the collagen scaffold for different electric field thresholds allowed us to construct a plot that related the two variables. **B)** Overlaying the electric field contour lines taken from our numerical model with an image of a 5 mM $CaCl_2$ treatment demonstrated the accuracy of the finite element model (scale bar 1 mm). The scaffold has a total area of 78.54 mm^2.

From our numerical model of the collagen scaffold, we determined a relationship between lesion area and electric field magnitude by performing numerical integration on the surface of the scaffold for a range of electric field magnitudes (100-1500 V/cm). We constructed a curve and fit this data using least squares fitting in MATLAB. This resulted in a sixth order polynomial equation shown in figure 3.5. Despite this equation not having relevance to the physics in our model, we were able to use it to accurately back out the electric field thresholds for each treatment condition without needing to manually determine them using COMSOL. Least squares fitting resulted in a maximum relative error of 4.7%.

Increasing the applied voltage from 450 V to 800 V demonstrates that it is possible to increase the lesion area by applying a higher voltage during treatment, however, the applied voltage in our experiment was limited by the size of the scaffold. If we were to apply 800V in combination with

5 mM $CaCl_2$, the lesion size and shape may be influenced by the electrically insulated boundaries of the collagen scaffold and an accurate area may be difficult to measure. An applied voltage of 450 V was chosen because it provides a wide range of electric field magnitudes over a broad range of areas. Figure 3.5B shows electric field contours taken from the numerical model of the collagen scaffold, overlaid onto a treatment using IRE in combination with 5 mM $CaCl_2$ solution. Electric field lines of high magnitude are plotted to locate the electrodes in the image and place the overlaying solution accurately. The average field threshold using least squares fitting was calculated to be 377 ± 18.6 V/cm. An electric field contour of 400 V/cm demonstrates the accuracy of the numerical solution in predicting cell death thresholds.

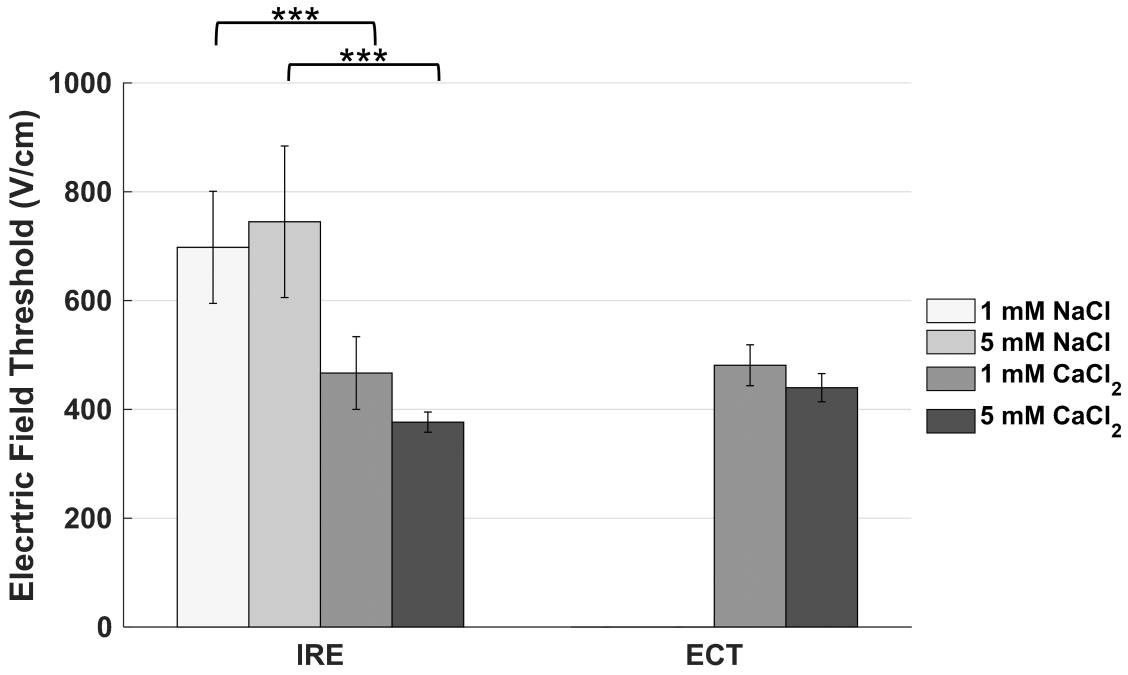

Figure 3.6: Calculated electric field thresholds for collagen scaffold experiments demonstrate that $CaCl_2$ treatments lead to significantly lower cell death thresholds than their NaCl controls. 3D collagen experiments consisted of 4.0 mm electrode spacing, 100 μs pulse width, 1 Hz frequency and 450 V. For IRE, 80 pulses were delivered while for ECT, 8 pulses were delivered. Collagen scaffolds had a total area of 78.54 mm^2 and thickness of 1 mm. U251 MG cells were seeded at a concentration of $1x10^6$ cells/mL. ECT treatments with NaCl solutions are not shown due to no lesion being present. (***$p<0.0001$).

Figure 3.6 shows the electric field thresholds that were calculated using the polynomial equation. IRE treatments used in combination with $CaCl_2$ solutions had significantly lower field thresholds

than their NaCl controls. A treatment using IRE and 1 mM $CaCl_2$ resulted in a field threshold of 467 $\pm$ 67 V/cm whereas IRE used in combination with 1 mM NaCl resulted in a threshold of 698 $\pm$ 103 V/cm. Increasing the amount of calcium in our solution to a 5 mM concentration resulted in a further reduced threshold of 377 $\pm$ 19 V/cm. This threshold was significantly lower than its control using 5 mM NaCl (745 $\pm$ 139 V/cm). IRE treatments using 5 mM $CaCl_2$ resulted in a lower threshold than ECT treatments using 5 mM $CaCl_2$ (440 $\pm$ 26 V/cm), but the difference was not statistically significant (p = 0.3853). The same is true for a $CaCl_2$ concentration of 1 mM, which resulted in an average threshold value for an ECT treatment of 481 $\pm$ 38 V/cm (p = 0.9997).

3.4.4 Simulating lesion volumes for an in vivo treatment in the brain

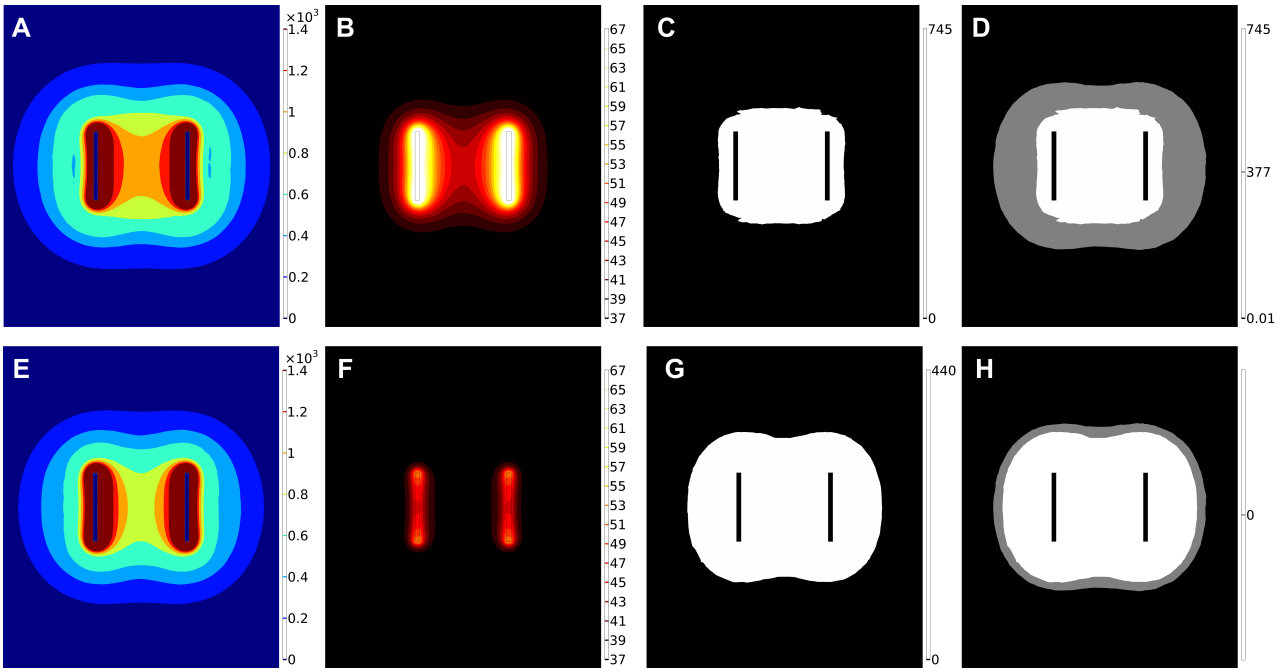

Figure 3.7: Our numerical model simulating an *in vivo* treatment indicates IRE has a larger increase in lesion size than ECT when used in combination with 5 mM $CaCl_2$ (xz plane). **A)** Electric field distribution (V/cm) after IRE treatment (3000 V, 2.0 cm electrode spacing, 50 pulses). **B)** Temperature distribution after IRE treatment (°C) **C**) Lesion size after IRE with 5 mM NaCl control (white) **D)** Comparing lesion size for IRE with 5 mM NaCl control (white) and 5 mM $CaCl_2$ (gray). **E)** Electric field distribution (V/cm) after ECT treatment (3000 V, 2.0 cm electrode spacing, 8 pulses). **F)** Temperature distribution after ECT treatment (°C) **G)** Lesion size after ECT treatment with 5 mM $CaCl_2$. **H)** Comparing lesion size for ECT (white) and IRE (gray) treatments in combination with 5 mM $CaCl_2$.

Calculating the field threshold for an in vitro calcium IRE treatment enabled us to estimate what will occur during an in vivo treatment. Figure 6 shows the results of our numerical simulation of ECT and IRE calcium treatments in a 3D model of the brain. Here, we have accounted for dynamic changes in conductivity of the tissue due to electroporation and changes in temperature that result due to Joule heating. Figures 3.7A and 3.7E indicate the electric field distributions in the tissue after an IRE and ECT treatment respectively along a cut plane in the xz axis. For an ECT treatment, the electric field magnitude between the electrodes does not reach as high a value as an IRE treatment. This is due to the low number of pulses applied (8 instead of 50). ECT pulses are designed to reversibly electroporate tissue and therefore the majority of the tissue does not reach a large enough magnitude to kill cells. The reversible regime of electroporation also covers a smaller area than an IRE treatment does.

Figure 3.7C shows the ablation zone for an IRE treatment without $CaCl_2$ (5 mM NaCl control). The ablation zone is greatly increased when 5 mM $CaCl_2$ is added (Figure 3.7D). An ECT treatment on the other hand, only has an ablation when $CaCl_2$ is used (Figure 3.7G). Comparing ECT and IRE ablations when 5 mM $CaCl_2$ is used (Figure 3.7H) shows that the calcium IRE lesion is larger. These results are also reflected in Table 3.

Table 3.3 shows lesion volumes calculated using the numerical model of the brain for applied voltages of 2000 and 3000 V. For 3000 V, the lesion volume for a 1 mM $CaCl_2$ treatment using IRE pulses is 2.10X larger than lesion size for a 1 mM NaCl treatment. The increase is even more substantial for a 5 mM $CaCl_2$ treatment using IRE pulses. At an average lesion volume of 29.80 ± 1.57 cm^3, this extends well beyond the bulk tumor margin.

Figure 3.8 reveals the relationship between applied voltage and lesion volume for the 3D model of the brain. As voltage increases with constant electrode spacing, the difference between a 5 mM $CaCl_2$ treamtent using ECT and IRE pulses grows substantially. When used in combination with IRE pulses, a concentration of 5 mM $CaCl_2$ results in an increase in lesion volume 1.4X an ECT treatment using the same concentration of calcium solution. This drastic increase can be

Table 3.3: Lesion volume for each experimental condition calculated using a numerical model of the brain with different applied voltages (electrode spacing of 2.0 cm).

Pulse	Treatment	Volume at 2000 V (cm^3)	Volume at 3000 V (cm^3)
IRE	1 mM $CaCl_2$	11.54 ± 2.96	23.56 ± 3.83
	1 mM NaCl	2.77 ± 1.50	11.20 ± 4.69
	5 mM $CaCl_2$	15.30 ± 0.88	29.80 ± 1.57
	5 mM NaCl	2.35 ± 1.93	9.34 ± 5.09
ECT	1 mM $CaCl_2$	10.17 ± 1.40	18.90 ± 1.82
	1 mM NaCl	No lesion	No lesion
	5 mM $CaCl_2$	11.68 ± 0.91	20.93 ± 1.42
	5 mM NaCl	No lesion	No lesion

attributed to the fact that both the irreversibly and reversibly electroporated regions are growing as the number of pulses delivered increases. The degree to which the tissue is electroporated increases dramatically with increased voltage, highlighting our ability to modulate pulse parameters to optimize treatment.

3.5 Discussion

The overall goal of our study was to determine if using calcium in combination with IRE resulted in larger lesions than IRE alone and ECT pulses combined with calcium. During an IRE treatment, there will be four zones of electroporation: 1) small zone of cell death caused by thermal damage (Joule heating), 2) medium sized zone of necrotic tissue in which cells are electroporated, lose homeostasis and are unable to recover, 3) large zone of apoptotic cell death in which defects in the membrane close, but cells are unable to recover, and 4) reversibly electroporated cells that recover and survive [18]. Use of calcium IRE intensifies this cell death phenomenon and takes advantage of the reversibly electroporated zone of cells by driving them to cell death using calcium, therefore

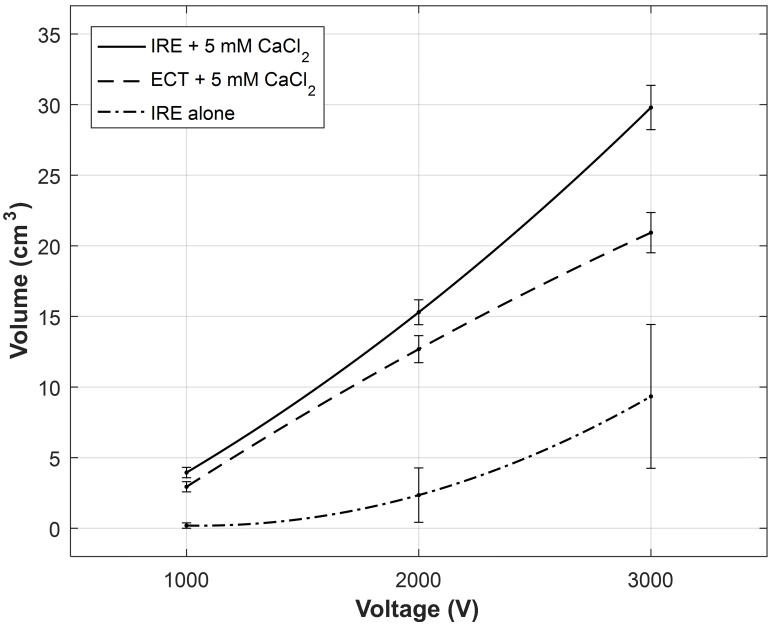

Figure 3.8: Numerical modeling predicts larger lesion volume in vivo for an IRE calcium treatment when compared to an ECT calcium treatment or IRE alone. The model consisted of two electrodes spaced 2.0 cm apart in a 3D domain of brain tissue. Three different applied voltages were tested (1000 V, 2000 V, 3000 V).

enhancing our zone of ablation.

Lee et al., have discussed the role that calcium can play in cell death after electroporation [18]. This was evidenced when cells were electroporated with a 450 ms pulse with 150 V/cm magnitude and a sharp increase in intracellular calcium levels was observed. Instead of a rapid drop in calcium concentration after the pulse was removed, the authors saw sustained elevated levels for 10 minutes. A sudden influx of calcium ions may lead cells to consume their supply of ATP to pump excess calcium across the cell membrane. This depletion of ATP after calcium electroporation has been shown by Frandsen et al., after electroporating Chinese hamster lung fibroblast cells with ECT pulses and 1 mM calcium [41]. Intracellular ATP levels decreased markedly and remained at 10.3% of control values eight hours after treatment. Furthermore, evidence has shown that elevated levels of intracellular calcium may activate proteases and phospholipases that further damage the cell and membrane, preventing pores from resealing after electroporation [129].

The possibility of enhancing ablation size by using calcium to drive cells in the reversibly electroporated zone to undergo cell death is supported by our experimental results and numerical modeling. In Figure 3.3, ECT treatments using NaCl solutions resulted in no cell death. Cells exposed to this ECT treatment are reversibly electroporated and are therefore able to recover and maintain viability. As evidenced by both ECT and sham treatments, the saline solution does not lead to cell death. Scaffolds exposed to IRE pulses in NaCl solutions, on the other hand, form a small region of cell death extending beyond the immediate vicinity of the electrodes (13.2 ± 3.6 mm^2 for 5 mM NaCl). It can be concluded that these cells experience irreversible electroporation (zone 2 described above). For both ECT and IRE treatments using $CaCl_2$, a large zone of cell death formed in the scaffold. Since a comparable lesion was not observed for NaCl treatments using the same applied pulses, it can be concluded that the region of cell death extending beyond what was seen with NaCl is due to the action of calcium and not the buffer or additional heating effects due to changes in conductivity of the scaffold. A 1 mM $CaCl_2$ treatment results in a lesion area of 25.1 ± 3.9 mm$_2$ for IRE and 23.8 ± 2.5 mm^2 for ECT. A 5 mM $CaCl_2$ treatment resulted in much larger lesion areas for both IRE (32.5 ± 2.0 mm^2) and ECT (26.7 ± 2.1 mm^2). The fact that 1 mM $CaCl_2$ results in a smaller lesion area than 5 mM $CaCl_2$ suggests that some cells in the periphery of the reversibly electroporated zone can recover from treatment. Using a higher concentration (5 mM $CaCl_2$) further exacerbates the effects of calcium, rendering the cells unable to recover from the treatment, causing additional cell death. The lesion area of our treatments may be influenced by the lower conductivity of our medium, as shown previously by Pucihar et al [130]. Our lesion area results are consistent with the findings of Frandsen et al., when comparing calcium ECT treatment to NaCl controls in vitro [41] using three cell lines. The half maximal effective concentration of calcium (EC_{50}) was found to be 0.57 mM. At 1 mM calcium, viability for all three cell lines ranged from 10-30% and at 3 mM calcium, viability for all three cell lines was below 20%. Cell death saturated at 5 mM calcium with viability for all three cell lines being below 10%. We have extended the implications of that study to provide further evidence that calcium can also be used to enhance lesion boundaries when used in combination with IRE pulses.

Calcium treatments decreased the required electric field threshold for cell death. When treating with IRE alone, we obtained a field threshold of 745 $\pm$ 139 V/cm whereas for 5 mM $CaCl_2$, we obtained 377 $\pm$ 19 V/cm, just over half of its control. This result is similar to findings of Hansen et al., where SW780 human bladder cancer cell lines were treated using ECT pulses with varying applied electric field magnitudes [43]. This suggests that it may be possible to increase lesion size without increasing the applied voltage, mitigating concern of additional thermal damage with higher energy IRE treatment.

Our numerical model that simulates a treatment in the brain, predicts an efficacy enhancement for IRE and calcium therapy that may be expected in a clinically relevant in vivo setting. A 5 mM $CaCl_2$ IRE treatment resulted in an increase in lesion volume three times that of its NaCl control. Comparable results were found in a mouse model, when tumors treated with 168 mM $CaCl_2$ and electroporation dramatically decreased in volume immediately after treatment and continued to decrease in size up to 28 days after treatment [41]. We have previously demonstrated the safety and efficacy of IRE treatment for brain cancer in canine patients that presented with spontaneous gliomas [131, 115, 114]. Rossmeisl et al., demonstrated that IRE did not lead to neurotoxicity in six out of seven canine patients, increasing Karnofsky Performance Scale in all patients [63]. It has also been previously reported that non-thermal IRE treatment spares critical structures such as nerves [132, 133, 134], therefore we do not have reason to believe that neuron function will be impaired following IRE treatment. In future studies, it will be necessary to better characterize the effect of treatment on neurons and the increase in conductivity due to electroporation in human brain tissue. Treatments will also need to be simulated using 3D models reconstructed from patient MR images in order to ensure maximum accuracy and efficacy.

It should be noted that despite most tissues having extracellular calcium concentrations around 1 mM, calcium ions are often bound by other macromolecules and only a small fraction are free in the extracellular fluid. Therefore, when treating tumors in vivo using calcium electroporation, administration of exogenous calcium will be required for effect. Ensuring uniform distribution of calcium in the tissue to be treated may be difficult to achieve due to leaky vasculature, high

interstitial pressure and convective forces that drive fluid out of the tumor. The potential challenges associated with delivery of calcium needs to be investigated in future research. Previously, Frandsen et al., has demonstrated that direct tumor injection in combination with ECT has been successful in treating mice that were injected with human small cell lung cancer cells [41]. $CaCl_2$ solutions were injected into the tumor at a volume that was 50% of tumor volume and the needle was moved around the tumor to ensure uniform injection. Using this technique, 89% of treated tumors ($\sim$1 cm^3) were eliminated. It may also be possible to have co-delivery of the treatment with a needle electrode system, although this may present a challenge in and of itself and will be left for future work.

Calcium IRE may provide an advantage over calcium ECT for in vivo treatment of tumors since IRE treatment ensures that the bulk of the tumor will be killed whereas ECT does not. While the bulk tumor is destroyed, the reversibly electroporated region extending beyond the tumor margin will experience an influx of calcium, exacerbating cell death and enhancing the ablation margin.

3.6 Conclusion

We have demonstrated that $CaCl_2$ treatment used in combination with IRE therapy leads to larger lesions than IRE alone. Consequently, the electric field threshold needed to kill the cancer cells is reduced by nearly half, suggesting that larger lesions are attainable without an increase in applied energy. Results from our numerical models indicate calcium IRE treatment in vivo can lead to treatment volumes that are 1.4X larger than calcium ECT treatments and 3.2X larger than IRE alone. While this study focused on calcium IRE treatment of brain cancer cells, the implications of these results are applicable to many types of cancer that are unresectable and invasive. Since calcium buffer solutions are regularly used in clinical settings and are known to be nontoxic to cells with intact cell membranes, calcium IRE may provide a safe and effective way to increase treatment volumes without inducing additional thermal damage.

Chapter 4

Understanding the role of calcium-mediated cell death in high-frequency irreversible electroporation

4.1 Abstract

[1] High-frequency irreversible electroporation (H-FIRE) is an emerging electroporation-based therapy used to ablate cancerous tissue. Treatment consists of delivering short, bipolar pulses (1-10 μs) in a series of 80-100 bursts (1 burst/s, 100 μs on-time). Reducing pulse duration leads to reduced treatment volumes compared to traditional IRE, therefore larger voltages must be applied to generate ablations comparable in size. We show that adjuvant calcium enhances ablation area *in vitro* for H-FIRE treatments of several pulse durations (1, 2, 5, 10 μs). Furthermore, H-FIRE treatment using 10 μs pulses delivered with 1 mM $CaCl_2$ results in cell death thresholds (771 $\pm$ 129 V/cm) comparable to IRE thresholds without calcium (698 $\pm$ 103 V/cm). Quantifying the reversible electroporation threshold revealed that $CaCl_2$ enhances the permeabilization of cells compared to a NaCl control. Gene expression analysis determined that $CaCl_2$ upregulates expression of *EIFB5* and 60S ribosomal subunit genes while downregulating *NOX1/4*, leading to increased signaling in pathways that may lead to necroptosis. The opposite was found for control treatment without

[1] E.M. Wasson, N. Alinezhadbalalami, R.M. Brock, I.C. Allen, S.S. Verbridge, R.V. Davalos. Understanding the role of calcium-mediated cell death in high-frequency irreversible electroporation. *Bioelectrochemistry*, 131, 2020.

$CaCl_2$ suggesting cells experience an increase in pro survival signaling. Our study is the first to identify key genes and signaling pathways responsible for differences in cell response to H-FIRE treatment with and without calcium.

4.2 Introduction

Irreversible electroporation (IRE) treatment is an alternative to standard cancer therapies and has been shown to successfully treat the most aggressive, and sometimes unresectable tumors such as pancreatic adenocarcinoma and hepatocellular carcinoma in human patients [58, 135, 57, 59] as well as glioblastoma in canine patients [115, 63, 115, 131]. In a typical electroporation treatment, needle electrodes are inserted into the tumor and a series of electrical pulses are delivered to the tissue. The applied electric field induces a rise in the cells' transmembrane potential (TMP). This rise in TMP lowers the energy needed for hydrophilic pores to form in the membrane [16, 17] in a phenomenon known as electroporation. These pores allow the exchange of otherwise impermeable molecules and ions into and out of the cell. Additionally, recent studies have shown that voltage gated channels may affect transport during electroporation [101], also allowing exchange of molecules that may lead to a loss of cellular homeostasis. Pulse parameters that are applied (field strength, pulse duration, and number of pulses) can be varied to elicit different cellular responses. Below a critical energy threshold, cells can recover from the loss of homeostasis and the pores may reseal over time. The cells are then said to experience reversible electroporation. Taking advantage of the enhanced cell membrane permeability and transport into the cell, reversible electroporation has commonly been used in gene transfer [136, 137] as well as for the treatment of tumors in a technique known as electrochemotherapy (ECT) [23, 37, 118, 138]. However, if the applied energy surpasses the critical threshold, cells cannot recover from the loss of homeostasis induced by the electrical field. The permanent loss of homeostasis results in cell death and cells are said to experience irreversible electroporation. IRE has been shown to cause minimal thermal damage to tissue [49], unlike techniques such as radiofrequency and microwave ablation, therefore

sparing critical structures such as vasculature and nerves [55, 63].

Despite the promising outlook of IRE for treatment of unresectable tumors [56], clinical application of IRE is known to cause muscle contractions in human and animal patients, requiring the use of neuroparalytic agents [62, 60]. We have developed a second generation modality of IRE treatment known as high-frequency irreversible electroporation (H-FIRE) to address these limitations [64]. While traditional IRE treatment uses square, unipolar pulses of 100 μs, H-FIRE treatment uses bipolar pulses that are much shorter in duration (1-10 μs) and are delivered in a series of 80-100 bursts (1 burst/s), as in the case of IRE (1 pulse/s). It has been hypothesized that delivering pulses at a higher frequency diminishes the dependence of IRE on cell size and tissue geometry [139, 90, 96]. Nonlinear changes in tissue conductivity occur to a lesser degree than in IRE treatment [69, 111] and therefore ablations using H-FIRE have been shown to be more predictable and uniform [68, 70]. H-FIRE treatment also mitigates muscle contractions seen with IRE treatment [64]. However, reducing pulse duration in H-FIRE treatment leads to a reduction in treatment volume compared to traditional IRE. This limitation necessitates the use of much larger applied voltages to generate ablations comparable in size. Higher voltages may increase thermal damage and the likelihood of inducing muscle contractions [70, 71, 72], therefore negating some of the benefits that H-FIRE treatment has over traditional IRE.

It has been shown that utilizing ECT pulses in combination with adjuvant calcium results in ATP depletion of cancer cells for as long as eight hours after treatment, compared to only one hour after electroporation treatment alone, leading to enhanced cell death [42, 41, 44, 43, 140]. Motivated by these studies, we have previously demonstrated that using adjuvant calcium in combination with IRE treatment induces a larger zone of cell death without the need to increase the energy applied to the tissue [141]. We hypothesize that using adjuvant calcium will enhance the lethality of H-FIRE treatment. Utilizing adjuvant calcium with H-FIRE treatment will allow us to retain its clinical advantages while eliminating the need to use higher voltages to produce ablations similar in size to traditional IRE treatment.

We investigated our hypothesis using a simplified collagen hydrogel model of a tumor that allowed visualization of treatment ablations. Cancer cells were seeded in collagen scaffolds and treated using H-FIRE waveforms of varying pulse durations (1, 2, 5, and 10 μs) with and without calcium. Reversible and irreversible electroporation thresholds were quantified and compared to our previously tested calcium IRE treatments [141] to elucidate differences in cell death response to extracellular calcium. Finally, we began work to uncover the biological effects on cells in response to H-FIRE treatment with and without calcium, which to our knowledge, has not been previously investigated. Our results show that adjuvant calcium enhances ablation size for all H-FIRE treatments. Furthermore, 10 μs pulses delivered with calcium result in ablations comparable in size to IRE treatment without calcium. Additional mechanistic studies identified signaling pathways associated with NADPH oxidase activity, ROS production, and the translation of stress related mRNA that were differentially dysregulated under $CaCl_2$ and no $CaCl_2$ conditions, impacting cell death.

4.3 Materials and Methods

4.3.1 Cell culture

U251 malignant glioma cells (Sigma Aldrich) were maintained at 5% CO2 and 37°C in Eagle's Minimum Essential Medium (Sigma Aldrich) supplemented with 1% penicillin/streptomycin (Life Technologies), 10% fetal bovine serum (Atlanta Biologicals), 1% non-essential amino acids (Sigma Aldrich) and 1 mM sodium pyruvate (Sigma Aldrich). Cells were routinely passaged at 80-90% confluence.

4.3.2 Collagen scaffold preparation

Sterile polydimethylsiloxane (PDMS, SYLGARDTM 184, Dow Corning) wells (10 mm diameter, 1 mm height) were placed in a 24 well plate to ensure uniform scaffold geometry and electric field

distribution between each replicate. PDMS wells were treated with 1% PEI for 10 minutes (Acros Organics), 0.1% glutaraldehyde (Fisher Scientific) for 20 minutes, and then washed twice with deionized water prior to collagen seeding to ensure collagen adhesion during treatment. Commercial rat tail collagen type I (BD Biosciences) was neutralized using a solution of 10X Dulbecco's Modified Eagle Medium (10% total volume, Sigma Aldrich), 1 N NaOH (2% collagen volume, Sigma Aldrich), and 1X Dulbecco's Modified Eagle Medium (Sigma Aldrich) to a final concentration of 5 mg/mL. U251 cells were detached from flasks using 0.25% trypsin/EDTA (Thermo Fisher Scientific) solution and added to the neutralized collagen solution at a concentration of $1x10^6$ cells/mL. The collagen/cell solution was dispensed into PDMS tops molded the collagen flat while they polymerized in a cell culture incubator for 20 minutes. PDMS tops were then removed and cell culture media was added. Collagen scaffolds were maintained in the incubator for 24 hours prior to treatment.

4.3.3 Electroporation treatment

After 24 hours, the media was aspirated from scaffolds and replaced with either $CaCl_2$ (Fisher Scientific) or NaCl (Fisher Scientific) solutions (1 mM or 5 mM). Each solution contained the same base components; 250 mM sucrose (Fisher Scientific), 1 mM $MgCl_2$ (Sigma Aldrich) and 10 mM HEPES buffer (Sigma Aldrich) in deionized water with pH of 7.2-7.4. Table 4.1 lists the osmolarity and conductivity of buffers used in this study.

Solutions incubated in the wells at room temperature for 30 minutes, were aspirated, and then replaced with fresh $CaCl_2$ or NaCl solutions for another 10 minutes to ensure that all media was removed. Fresh solutions were added immediately prior to pulsing. A custom-designed electrode housing was used to ensure precise placement (4 mm center-to-center spacing) of two hollow, stainless-steel blunt tip needles with 0.914 mm outer diameter and 0.635 mm inner diameter (Howard Electronic Instruments) into the collagen scaffold. To investigate whether enhanced cell death was unique to calcium, other ions that are involved in removing calcium from the cell were

Table 4.1: Properties of solutions used in experiment

Concentration	Solution	Conductivity (S/m)	Osmolarity (mOsm/L)
1 mM	$CaCl_2$	0.075 ± 0.004	307 ± 25.5
	NaCl	0.056 ± 0.001	302 ± 27.4
	KCl	0.064	289
	$CaCl_2$ + NaCl	0.065	287
5 mM	$CaCl_2$	0.131	300
	NaCl	0.089	291

tested, namely KCl (1 mM, Alfa Aesar) and a combination of $CaCl_2$ and NaCl (1 mM each). These treatments followed the same protocol described above.

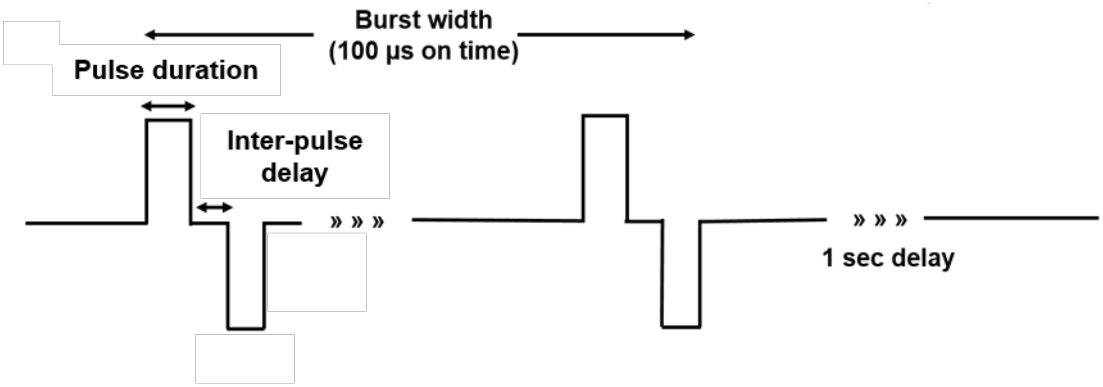

Figure 4.1: Schematic of bi-polar H-FIRE waveforms. The same inter-pulse delay (1 μs) and varying pulse durations (1, 2, 5, 10 μs) were investigated in this study. A series of 80 bursts were delivered at the frequency of one burst/s and amplitude of 800 V for a total on time of 100 μs. H-FIRE waveforms are described in this study by the following name scheme (positive pulse duration – inter-pulse delay - negative pulse duration).

Several H-FIRE pulses were investigated in this study and delivered using a custom-built pulse generator (EPULSUS®-FBM1-5, EnergyPulse Systems). Waveforms were captured using a voltage probe (BTX, Harvard Apparatus) and oscilloscope (DPO 2012, Tektronix). An H-FIRE waveform can be described by pulse duration, inter-pulse delay, number of pulses, number of bursts, and frequency of burst delivery (Figure 4.1). Here, we describe the treatment delivered by the param-

eters of one bipolar pulse (positive pulse duration, inter-pulse delay, and negative pulse duration). Inter-pulse delay was kept constant at 1 μs while pulse duration was varied (1, 2, 5, and 10 μs). 80 bursts with a total on-time of 100 µs (100, 50, 20 and 10 pulses respectively) were delivered at a frequency of 1 burst/s and a voltage of 800 V. For irreversible threshold experiments, $CaCl_2$ and NaCl solutions were aspirated and replaced with cell culture media and scaffolds were returned to the incubator for 24 hours prior to live/dead staining. For reversible threshold experiments, scaffolds were imaged immediately after treatment as described below.

4.3.4 Analysis of ablation area

To visualize ablations, scaffolds were stained with calcein AM and propidium iodide (PI). It has been previously determined that 24 hours post treatment is sufficient to allow any reversibly electroporated cells to recover as pore resealing happens on the order of minutes [142, 143], therefore, staining the cells immediately after treatment and 24 hours later allows us to quantify both the reversible zone of electroporation and irreversible zones of ablation. To stain the scaffolds, media was removed and replaced with phosphate buffered saline (PBS) containing 2 µM calcein AM (Invitrogen) and 23 µM PI (Invitrogen) and incubated at room temperature for 30 minutes. Scaffolds were then washed twice with PBS prior to imaging using an inverted microscope (DMI 6000B, Leica Microsystems) with a 5x objective and an EM-CCD camera (Hamamatsu C9100). The appropriate filters were used to image Calcein AM (Ex:460-500, DC: 505, EM: 570-640) and propidium iodide (EX:545/26, DC:565, EM:605/70). To determine the reversible zone of electroporation, treatment followed the same electroporation protocol described above, but calcein AM and PI were added to the $CaCl_2$ and NaCl solutions at all steps prior to pulsing. Scaffolds were then imaged immediately after treatment. For analysis, images were separated into two channels (green – calcein AM, red – PI) and ablation areas for the green channel were analyzed for irreversible thresholds and red channels for reversible electroporation thresholds using a custom algorithm written in MATLAB as previously described [141]. In cases where the algorithm was

unable to accurately measure ablations, coordinate points from the algorithm outlining the ablation area were used as a guide to manually trace and measure the area in ImageJ.

4.3.5 Numerical model simulating H-FIRE treatment enables determination of reversible and irreversible electroporation thresholds

Lesion area measurements were then mapped to a finite element model of the experimental setup to determine the corresponding electric field threshold. The electric field and temperature distributions were simulated in the collagen scaffold using COMSOL Multiphysics (v5.3, Burlington, MA). It has been previously determined that H-FIRE ablations can be predicted by solving Laplace's equation for potential distribution in tissue [68], therefore the spatial distribution of electric potential (ϕ) can be expressed as:

$$0 = \nabla^2 \phi \tag{4.1}$$

where the electric field can be defined as ($E = -\nabla\phi$) with an electro-quasistatic approximation. In addition, it has been shown that a constant conductivity solution matches well with a simulated H-FIRE treatment including an empirically determined non-linear conductivity equation [69], therefore in this study, a constant conductivity is used to simplify the simulation. One electrode was set to ground ($\phi = 0V$) while the other was set to the applied voltage used ($\phi = 800V$). The remaining boundaries were treated as electrically insulated ($\partial\phi/\partial n = 0$).

The temperature distribution in the scaffold can be described by the following governing equation:

$$\rho c_p \frac{\partial T}{\partial t} = k\nabla^2 T + \sigma |E|^2 \cdot \frac{d}{\tau} \tag{4.2}$$

where ρ is density, c_p is specific heat capacity, k is thermal conductivity and σ is electrical conductivity, all defined for both the collagen scaffold and electrodes (Table 4.2). Since collagen

Table 4.2: Material properties used in numerical model

Parameter	Units	Collagen scaffold [51]	Electrodes [109]
Thermal conductivity (k)	$Wm^{-1}K^{-1}$	0.6	14
Density (ρ)	kgm^{-3}	997.8	477
Specific heat capacity (c_p)	$Jkg^{-1}K^{-1}$	4181.8	7900
Electrical conductivity (σ)	Sm^{-1}	0.131 (measured)	2.22x10^6

hydrogels have a large water content, all thermal parameters were chosen to be the same as water [144, 145]. The equation for temperature distribution includes a joule heating term to simulate the electrical power that is dissipated into the scaffold during treatment. Instead of simulating each pulse which is computationally expensive and offers little benefit [146, 64], we have taken a duty cycle approach and scaled the joule heating term by the total on time of the burst ($d = 100\mu s$) and frequency of burst delivery ($\tau = 1$ burst/sec).

The $CaCl_2$ solution with the highest conductivity (σ = 0.131 S/m) was used in the model to account for the maximum amount of heating that would occur in the scaffold. The exposed electrodes as well as the surface of the collagen scaffold were modeled as convective boundaries with ambient air (h = 25 W/mK) and initial temperature set to 22 °C. All other boundaries were treated as thermally insulated ($\partial T/\partial n = 0$) and thermal properties were assumed constant. The mesh of the model was refined until there was < 1% change in the electric field and temperature values along a cutline between the electrodes on the surface of the scaffold. Refinement resulted in a mesh that consisted of 83,881 tetrahedral and 18,734 triangular elements. Integrating along the surface of the collagen scaffold geometry determined the area encompassed by a range of electric field magnitudes (1-3200 V/cm). Least squares fitting was used to determine a relationship between area and electric field magnitude resulting in a sixth order polynomial equation. The reversible and irreversible electroporation thresholds were calculated using this equation.

4.3.6 Gene expression analysis

Collagen scaffolds, prepared as previously described, were subjected to 5 mM $CaCl_2$ (n = 10) or 5 mM NaCl (n = 10) solutions as described above. Wells were treated with either 2-1-2 or 10-1-10 H-FIRE waveforms while submerged with solution buffers. Treated wells were rested for 24 hours in media and then underwent collagenase digestion for cell retrieval. 0.5% collagenase (Thermo Fisher) and 1% fetal bovine serum (Atlanta Biologicals) in Hanks Buffered Salt Solution (HBSS) (Lonza) were added to each well. The samples were then incubated at 37°C for 2 hours. Recovered cells were washed with ice cold PBS. Scaffolds were pooled by group and RNA extracted using TRIzol (ThermoFisher). RNA was converted to cDNA via RT2 Firststrand (Qiagen). Following cDNA generation, gene expression was profiled for 89 genes using a Qiagen Calcium Signaling RT2 Profiler PCR Array and data was evaluated utilizing the ΔΔCt. Method. The resulting fold changes in gene expression were used to determine the effects of H-FIRE treatment parameters on biological functions and complex signaling networks using Ingenuity Pathway Analysis (IPA), as previously described [147, 148, 149]. Results were normalized respectively to untreated cells. The gene list for each array and functional categories for each gene are available through the manufacturer. Ingenuity Pathways Analysis (IPA) and the manufacturer's array software (Qiagen) was used to analyze gene expression data. IPA data were ranked and evaluated based on z-score.

4.3.7 Statistical analysis

Irreversible experiments were repeated 6-12 times for each condition. Reversible experiments were repeated at least six times. Discrepancies in the number of replicates between conditions were due to bubbles or other defects that may have changed the electric field distribution or prohibited a reliable measurement of ablation area. These scaffolds were excluded from analysis. Two-way ANOVA was used to test for differences in cell death area due to the different applied solutions and pulse waveforms. Tukey post-hoc comparisons were used to examine differences among treatment groups. Statistical analyses were performed with a confidence level of $\alpha = 0.05$ (JMP Pro 14).

Results are shown as means ± standard deviation.

4.4 Results

4.4.1 Collagen scaffold allows testing a range of electric field magnitudes and determination of electroporation thresholds using finite element analysis

Our numerical model allows simulation and visualization of the electric field and temperature distribution in the collagen scaffold (Figure 4.2). Using surface integration, we can determine the area encompassed by different electric field magnitudes, enabling us to determine the electric field threshold that results in different ablation areas for each treatment. This platform provides measurements that are more relevant to in vivo treatments on tissue since the cells experience a 3D environment and are exposed to a range of electric field magnitudes. Simulating treatment resulted in a maximal temperature increase of 4.4 °C.

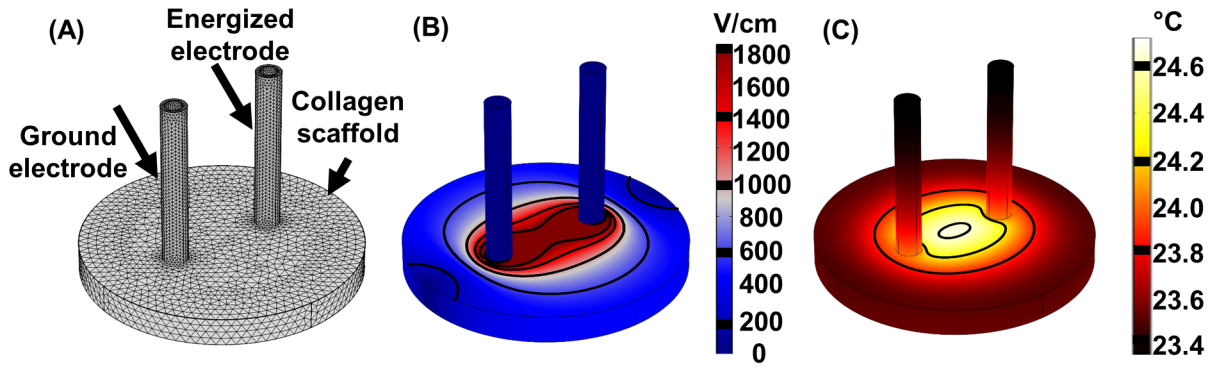

Figure 4.2: Simulating H-FIRE treatments using the finite element method allows us to determine the electric field and temperature distribution in the collagen scaffold. **(A)** The mesh was refined until there was < 1% change in electric field and temperature values along a cutline between the electrodes. The mesh consisted of 102,615 total elements. **(B)** Solving for the electric field distribution and quantifying area of electroporation allows us to determine the electric field threshold for each treatment. 800 V was applied with an electrode spacing of 4 mm (center-to-center). **(C)** Using the highest conductivity buffer (σ = 0.131 S/m) in the simulation led to a predicted increase in temperature of 4.4 °C in the collagen scaffold.

4.4.2 Adjuvant calcium increases ablation size for all conditions and is necessary to produce ablations for short pulse durations (<10 µs)

We tested a range of H-FIRE pulse durations (1, 2, 5, 10 μs) and calcium concentrations (1 mM and 5 mM) on cells seeded in collagen scaffolds to quantify cell death with and without calcium. Figure 4.3 shows that the ablations produced in the collagen scaffolds by calcium H-FIRE treatment are larger than NaCl controls for all pulse parameters tested. For short pulse durations (<10 μs), it seems that the cells treated with NaCl can recover from the treatment and no ablations are produced. Only in the presence of $CaCl_2$ or when longer pulse durations (>10 μs) are used, do continuous ablations form. Results suggest that the cell death response to $CaCl_2$ is dose dependent since treatments with 5 mM $CaCl_2$ result in larger ablations than those using 1 mM $CaCl_2$. As IRE and H-FIRE were delivered at different voltages, we directly compared the electric field thresholds evaluated by first quantifying ablation areas using ImageJ and a custom algorithm previously developed in MATLAB [141].

Figure 4.3 clearly demonstrates enhanced ablation area in response to calcium H-FIRE treatment. The increase of ablation area for 1 mM $CaCl_2$ compared to its NaCl control is nearly 2.13x for the 1-1-1 waveform, 2.79x for the 2-1-2 waveform, 5.69x for the 5-1-5 waveform, and 3.3x for the 10-1-10 waveform. For 5 mM $CaCl_2$, the 1-1-1 waveform results in a 3.47x increase in ablation area, for the 2-1-2 waveform there is a 4.37x increase, for the 5-1-5 waveform there is a 5.23x increase, and for the 10-1-10 waveform there is a 2.69x increase. As pulse duration increases, the area of ablation for $CaCl_2$ increases dramatically while for NaCl, ablation areas increase moderately. The 5-1-5 waveform results in the largest increase of ablation area between $CaCl_2$ and NaCl treatments. For 1 mM $CaCl_2$, the 5-1-5 resulted in a 5.69x increase in ablation area compared to NaCl and for 5 mM $CaCl_2$, the 5-1-5 resulted in a 5.23x increase in ablation area. Differences seen between calcium concentrations is more pronounced for shorter pulse durations (1 and 2 μs).

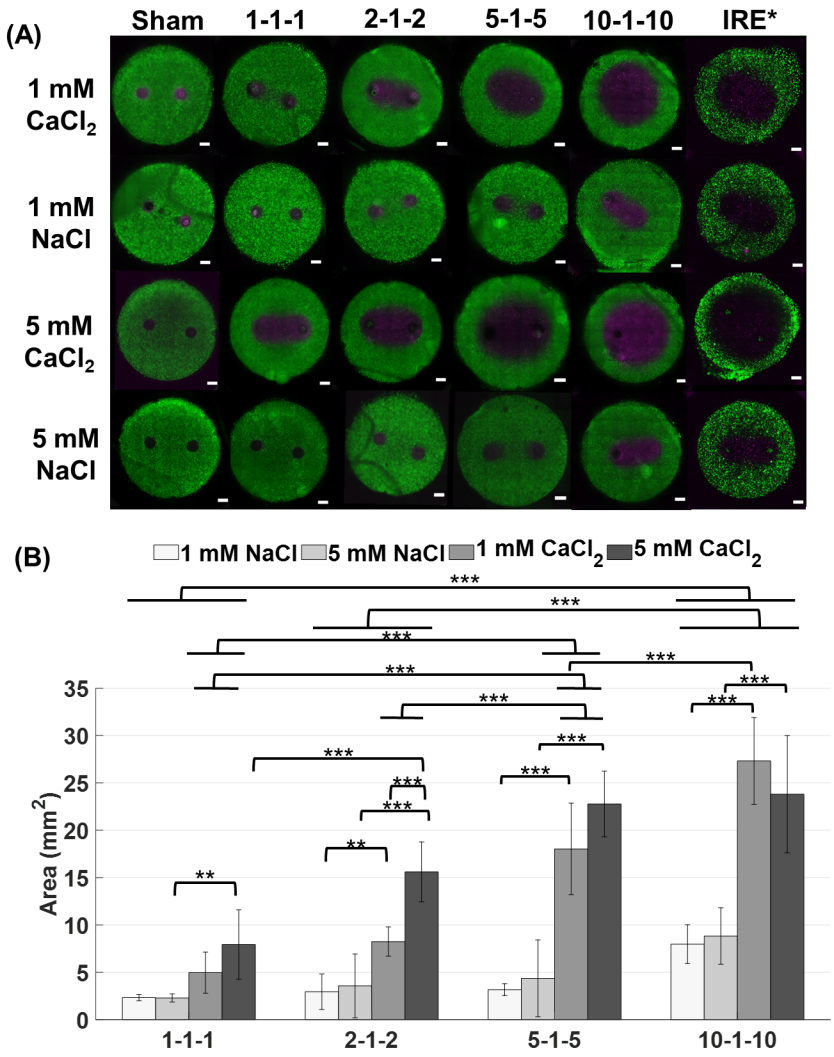

Figure 4.3: Ablation areas for $CaCl_2$ are significantly larger than ablations for NaCl for all pulse durations. Pulse durations below 10 μs, need $CaCl_2$ to produce an ablation larger than 5 mm^2 (*p < 0.001, **p < 0.05, scale bar 1mm). (A)** In vitro collagen scaffolds consisted of 5 mg/mL rat tail collagen type I and U251 malignant glioma cells (1x10^6 cells/mL). Electrodes were spaced 4 mm apart (center-to-center). For IRE treatments, 80, 100 μs pulses were delivered at 450 V and 1 Hz frequency. For H-FIRE treatments, 80 bursts of various pulse durations were delivered at 800 V at a frequency of 1 burst/s for a total on time of 100 μs. Live cells are stained with calcein AM (green) while dead and/or membrane compromised cells are stained with propidium iodide (magenta). Propidium iodide stains cells red, but the images are shown in magenta for visualization purposes (n $\geq$ 6 for all conditions). **(B)** Ablations were measured using a custom algorithm developed in MATLAB and ImageJ. The total area of the scaffold was 78.54 mm^2 (10 mm diameter) with a thickness of 1 mm. Results are shown as mean $\pm$ std. IRE* data was taken from a previous study (Wasson et al., 2017) [141].

4.4.3 Reversible electroporation zones using $CaCl_2$ are larger than NaCl controls

To investigate how $CaCl_2$ and NaCl treatments affect permeabilization of the cells, we characterized areas for reversible electroporation and their corresponding reversible electric field thresholds. Reversible electroporation thresholds for H-FIRE treatment have not been extensively characterized, making our study one of the first to quantify reversible thresholds for a range of unexplored pulse durations [150]. Figure 4.4 shows that both NaCl solutions had smaller reversible areas than their $CaCl_2$ counterparts, therefore the buffers used seemed to affect the extent that the cells were being permeabilized. In addition, it appeared that the difference between NaCl and $CaCl_2$ reversibly electroporated zones was similar for all waveforms. To compare the reversible zones more quantitatively, area was measured using our custom MATLAB algorithm. Figure 4.4B shows that for 1 mM $CaCl_2$, the reversible zone was 1.56x larger than the 1 mM NaCl zone for the 2-1-2 waveform, 1.7x larger for the 5-1-5 waveform, and 1.42x larger for the 10-1-10 waveform. For 5 mM $CaCl_2$, the reversible zone was 1.66x larger than the 1mM NaCl zone for the 2-1-2 waveform, 1.73x for the 5-1-5 waveform, and 1.46x larger for the 10-1-10 waveform. There was no statistically significant difference between 1 mM and 5 mM treatments for the reversible case, although, after 24 hours, the 5 mM $CaCl_2$ areas are larger than the 1 mM $CaCl_2$ for shorter pulse durations suggesting that cells exposed to lower levels of calcium recover to some extent.

Figure 4.5 shows that reversible electroporation zones were larger than irreversible zones for all conditions tested. For the 2-1-2 waveform, reversible zones were 4.68x larger than irreversible zones for 1 mM NaCl, 3.88x for 5 mM NaCl, 2.62x for 1 mM $CaCl_2$, and 1.47x for 5 mM $CaCl_2$. For the 5-1-5 waveform reversible zones were 5.58x larger than irreversible zones for 1mM NaCl, 3.94x for 5 mM NaCl, 1.67x for 1 mM $CaCl_2$, and 1.3x for 5 mM $CaCl_2$.

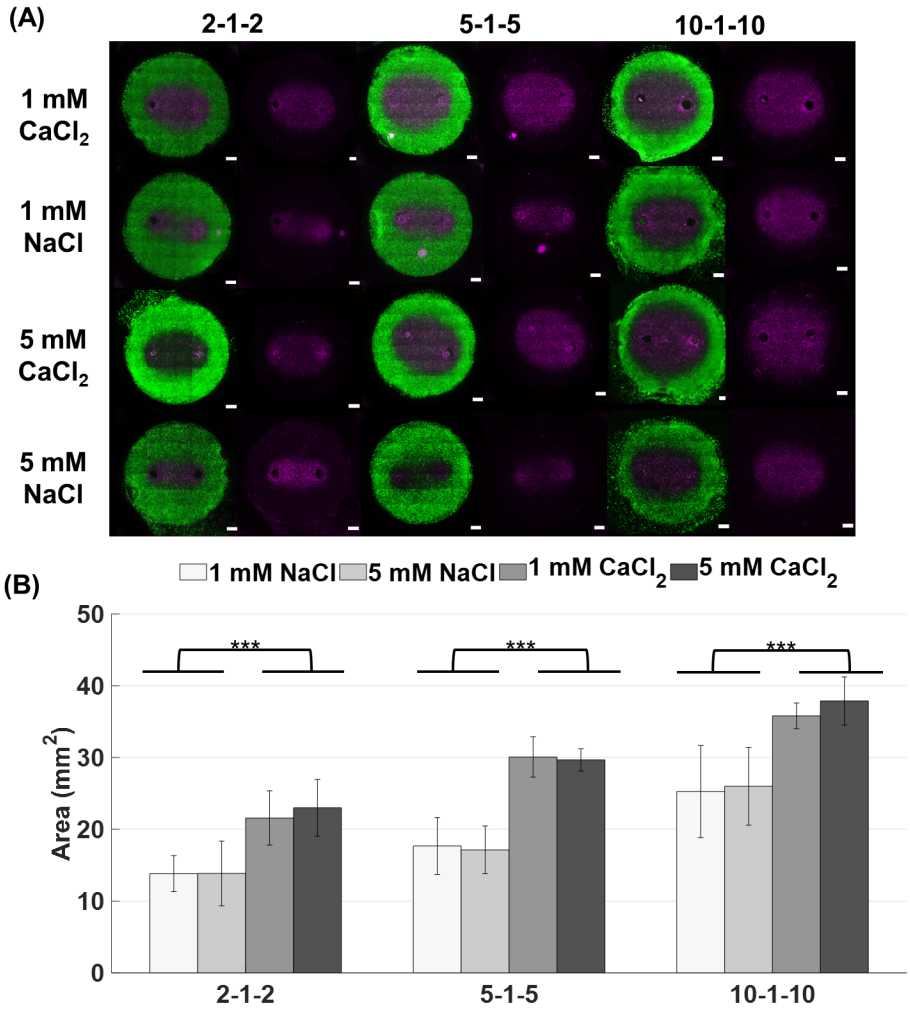

Figure 4.4: Reversible electroporation areas show that the NaCl buffer produces a smaller affected area than the $CaCl_2$ buffer indicating the cells are electroporated to a lesser extent. The NaCl buffer may provide protection against cell death whereas the $CaCl_2$ solution does not (* p < 0.001, scale bar 1 mm). (A)** The image on the left of each panel shows both the unpermeabilized (green) and permeabilized (violet) regions of cells while the image on the right (violet alone) shows permeabilized cells alone. In vitro collagen scaffolds consisted of 5 mg/mL rat tail collagen type I and U251 malignant gliomas ($1x10^6$ cells/mL). H-FIRE treatments consisted of delivering 80 bursts of pulses with various durations at 800 V and a frequency of 1 burst/s for a total on time of 100 μs. The total area of the scaffold was 78.54 mm^2 (10 mm diameter) with a thickness of 1 mm. **(B)** Reversible electroporation areas were measured using ImageJ and a custom algorithm developed in MATLAB. Electrodes were spaced 4 mm apart (center-to-center). Results are shown as mean $\pm$ std ($n \geq 6$ for all conditions).

For the 10-1-10 waveform, reversible zones were 3.17x larger for 1 mM NaCl, 2.94x larger for 5 mM NaCl, 1.32x larger for 1 mM $CaCl_2$, and 1.59x larger for 5 mM $CaCl_2$ when compared to

irreversible zones.

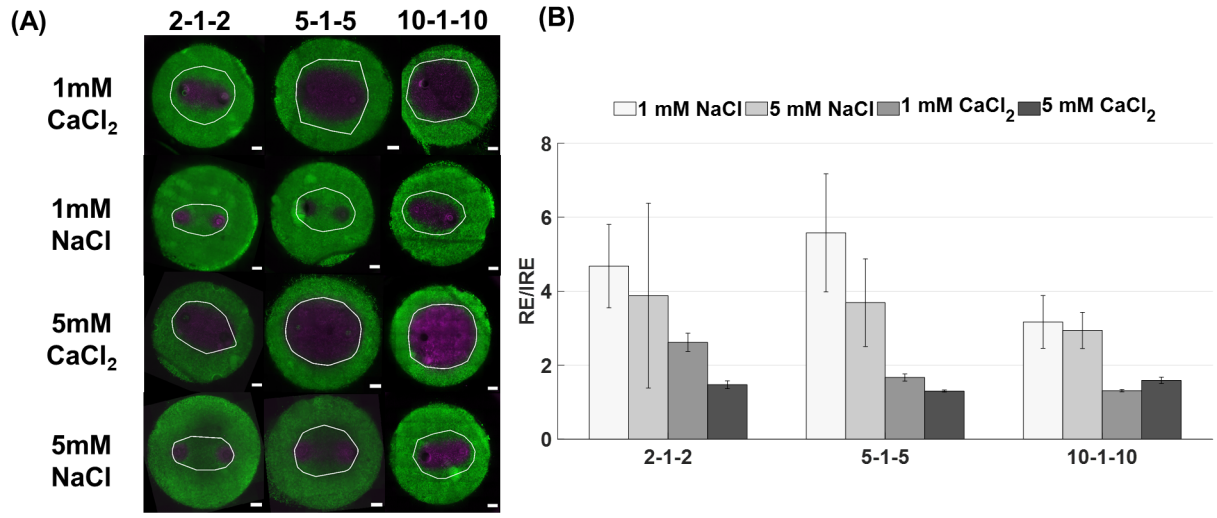

Figure 4.5: $CaCl_2$ reduces the difference between reversible and irreversible electroporation areas. (A) Reversible electroporation zones are overlaid (white) onto irreversible ablation images to demonstrate the effect that calcium has on enhancing the ablation margin. In vitro collagen scaffolds consisted of 5 mg/mL rat tail collagen type I and U251 malignant gliomas ($1x10^6$ cells/mL). H-FIRE treatments consisted of delivering 80 bursts of pulses with various durations at 800 V and a frequency of 1 burst/s for a total on time of 100 µs. The total area of the scaffold was 78.54 mm^2 (10 mm diameter) with a thickness of 1 mm. **(B)** The ratio of reversible electroporation (RE) to irreversible ablation areas (IRE) and the propagated uncertainty were calculated. Results are shown as mean $\pm$ std.

In Figure 4.5, the difference between reversible and irreversible electroporation areas was largest for NaCl solutions. When $CaCl_2$ was used, the difference between reversible and irreversible electroporation areas decreased. As pulse duration increased, the difference between reversible and irreversible electroporation areas also decreased for all conditions.

4.4.4 Using adjuvant calcium in combination with a 10-1-10 H-FIRE treatment reduces the irreversible electroporation threshold to that of an IRE treatment

Using our finite element model of H-FIRE treatment in the scaffold, we were able to find the corresponding electric field thresholds for each ablation area. Table I shows that using adjuvant

calcium reduces the electric field threshold in all experimental conditions. When compared to the NaCl control, 1 mM $CaCl_2$ reduces the electric field threshold 1.24x for the 1-1-1 waveform, 1.48x for the 2-1-2 waveform, 2.05x for the 5-1-5 waveform, and 2.19x for the 10-1-10 waveform. When comparing 5 mM NaCl to 5 mM $CaCl_2$, the electric field threshold is reduced 1.46x for the 1-1-1 waveform, 1.91x for the 2-1-2 waveform, 2.43x for the 5-1-5 waveform, and 1.83x for the 10-1-10 waveform. It seems the maximum effect for $CaCl_2$ is seen with 5 mM $CaCl_2$ for the 5-1-5 waveform and with 1 mM $CaCl_2$ for the 10-1-10 waveform. Using a 10-1-10 waveform with 1 mM $CaCl_2$ results in an electric field threshold of 771 $\pm$ 129 V/cm, reducing the threshold to less than half its value with NaCl (1641 $\pm$ 159 V/cm). It is important to note that 1 mM $CaCl_2$ also reduces the threshold to a level that is comparable to an IRE treatment with NaCl (698 $\pm$ 103 V/cm).

Table 4.3: Electric field threshold for both H-FIRE and IRE treatments. Results are presented in V/cm as mean $\pm$ std (n $\geq$ 6 for all conditions). Boxes highlight that the 10-1-10 H-FIRE treatment with calcium results in comparable electric field thresholds to standard IRE treatment.

		1-1-1	2-1-2	5-1-5	10-1-10	IRE
1 mM NaCl	Irreversible	2481 $\pm$ 87	2382 $\pm$ 275	2282 $\pm$ 134	1641 $\pm$ 159	698 $\pm$ 103
	Reversible		1299 $\pm$ 119	1124 $\pm$ 175	839 $\pm$ 217	524 $\pm$ 85
1 mM $CaCl_2$	Irreversible	2003 $\pm$ 270	1607 $\pm$ 112	1111 $\pm$ 208	771 $\pm$ 129	467 $\pm$ 67
	Reversible		954 $\pm$ 159	657 $\pm$ 67	577 $\pm$ 4	409 $\pm$ 57
5 mM NaCl	Irreversible	2494 $\pm$ 111	2331 $\pm$ 389	2197 $\pm$ 377	1597 $\pm$ 229	745 $\pm$ 139
	Reversible		1298 $\pm$ 206	1149 $\pm$ 148	804 $\pm$ 165	437 $\pm$ 88
5 mM $CaCl_2$	Irreversible	1702 $\pm$ 315	1222 $\pm$ 157	903 $\pm$ 145	871 $\pm$ 265	377 $\pm$ 19
	Reversible		900 $\pm$ 143	658 $\pm$ 36	578 $\pm$ 7	351 $\pm$ 53

4.4.5 The enhanced cell death effect is unique to calcium

There are several ion channels in the plasma membrane that act to pump calcium out of the cell. One of these pumps is the Na^+ - Ca^{2+} exchanger. The exchanger works to allow Na^+ to be transported into the cell while pumping Ca^{2+} out of the cell. To investigate whether NaCl would be able to aid the cells in pumping the excess Ca^{2+} out, we tested a solution that contained 1 mM of both ions. We also tested a solution of KCl to determine whether the enhanced cell death effect is unique to calcium. Figure 4.6 shows that the $CaCl_2$ solution and the combined solution of NaCl and $CaCl_2$ did not result in significantly different ablation sizes ($p < 0.001$), therefore, NaCl does not rescue the cells from the effect of excess Ca^{2+} and does not provide a protective mechanism (Figure 4.6). In addition, testing a 1 mM KCl solution did not result in statistically significant ablation size than the NaCl control, again confirming that the enhanced ablation areas were unique to calcium.

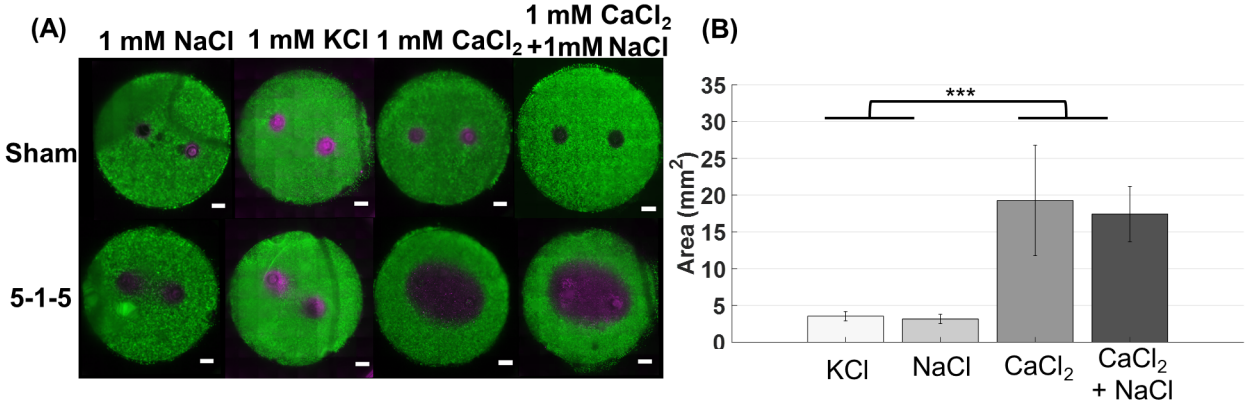

Figure 4.6: Enhanced cell death using H-FIRE treatment with pulse durations below 10 μs is unique to $CaCl_2$. Experiments were completed using a 5-1-5 waveform (*p < 0.001). (A)** In vitro collagen scaffolds consisted of 5 mg/mL rat tail collagen type I and U251 malignant glioma cells (1x10^6 cells/mL). Electrodes were spaced 4 mm apart (center-to-center). 80 bursts consisting of 5 μs pulses were delivered at 800 V, frequency of 1 burst/s for a total on time of 100 μs. Live cells are stained with calcein AM (green) while dead and/or membrane compromised cells are stained with propidium iodide (magenta). Propidium iodide stains cells red, but the images are shown in magenta for visualization purposes. **(B)** Using a combined solution of 1mM $CaCl_2$ and 1 mM NaCl (n = 5) results in ablations similar in size to $CaCl_2$ alone (n = 9), therefore NaCl is unable to rescue the cells from the effect of $CaCl_2$. Replacing $CaCl_2$ with KCl (n = 8), results in an ablation that is similar to NaCl alone.

4.4.6 NaCl condition leads to upregulated expression of *NOX1* and *NOX4* while calcium upregulates expression of *EIF5B*

To better define the mechanisms underlying calcium-mediated cell death following H-FIRE, we profiled gene expression patterns following the treatment of cells in either $CaCl_2$ or NaCl supplemented buffer. Our IPA evaluation identified 4 key signaling components that were significantly impacted by the adjuvant calcium (Figure 4.7). *NOX1* and *NOX4* were significantly upregulated in the NaCl treatment group compared to the downregulation observed in the $CaCl_2$ exposed cells (Figure 4.7A). Conversely, *EIF5B* and 60S Ribosomal Subunit signaling was significantly up-regulated in the $CaCl_2$ treatment group and significantly down-regulated in the NaCl exposed cells (Figure 4.7A). Both *NOX1* and *NOX4* encode NADPH oxidases that are best known for their roles in the generation of reactive oxygen species (ROS). The *EIF5B* gene encodes the Eukaryotic Translation Factor 5B that functions in translation initiation and interacts with the 60S Ribosomal Subunit. A heatmap was generated using the Average Linkage Euclidean Distance Measurement Method to better visualize the global changes in gene expression (Figure 6B). These data demonstrate the global changes in gene expression across treatment groups, with multiple differences observed between $CaCl_2$ and NaCl (Figure 4.7B).

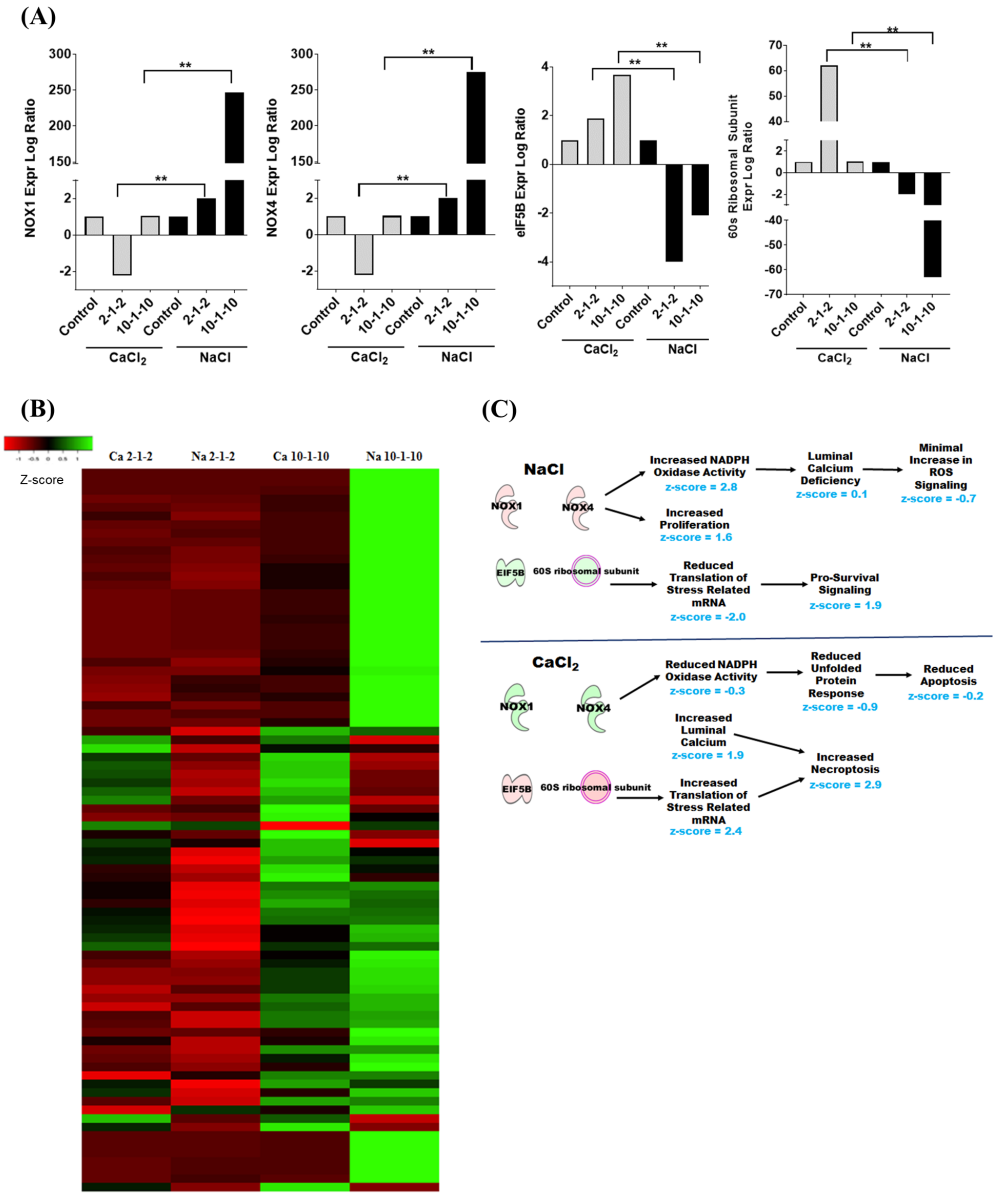

Figure 4.7: Signaling pathways associated with *NOX1/4* and *EIF5B* are differentially regulated following H-FIRE depending on $CaCl_2$ or NaCl environment. Gene expression profiling analysis identified biological functions specifically associated with *NOX1*, *NOX4*, *EIF5B* and the 60S ribosomal subunit that were significantly dysregulated following H-FIRE treatment and correlated with $CaCl_2$ or NaCl containing buffer. **(A)** Individual expression of each of these genes was significantly and differentially regulated based on $CaCl_2$ or NaCl. **(B)** Heatmap analysis reflects global changes in gene expression and revealed significant dysregulation among genes associated with NADPH oxidase activity, proliferation, cell death, calcium signaling, and cellular stress. Red is downregulated genes and green signifies upregulated genes. **(C)** Ingenuity pathway analysis of gene expression profiling data revealed differentially activated pathways, quantified by associated z-score, associated with increased proliferation and survival under NaCl conditions and increased necroptosis under $CaCl_2$ conditions following H-FIRE. Here, red represents upregulated genes and green signifies downregulated genes. $^{**}p < 0.01$.

Based on the significant correlation between changes in *NOX1*, *NOX4*, *EIF5B*, and the 60S ribosomal subunit signaling with NaCl and $CaCl_2$ and the diverse changes in global gene expression, IPA analysis identified a specific group of related biological functions impacted by H-FIRE treatment under the two cation conditions tested (Figure 4.7). Under NaCl conditions, H-FIRE induces as significant up-regulation in *NOX1* and *NOX4* expression. This upregulation results in an increase in genes associated with NADPH Oxidase activity (Figure 4.7C). However, consistent with the limited Ca^{2+} in the media, we observed gene expression changes consistent with a defect in luminal calcium signaling. Because NOX proteins require Ca^{2+} for ROS generation, these data are also consistent with the attenuation of ROS production observed in the NaCl conditions (Figure 4.7C). Together, these data suggest that the increase in *NOX1* and *NOX4* expression may be compensatory changes associated with the Ca^{2+} limited conditions in the NaCl buffer and likely signal attempts by the cell to generate ROS following H-FIRE treatment. Concurrently with the defect in ROS signaling, we also observed a significant decrease in *EIF5B* and the 60S Ribosomal Subunit signaling (Figure 4.7C). Consistent with these observations, IPA identified a significant decrease in pathways associated with the translation of stress related mRNA and a significant increase in signaling pathways associated with pro-survival (Figure 4.7C). Together, these data suggest that low Ca^{2+} conditions in the NaCl buffer provides a protective effect to minimize cell death following H-FIRE treatment.

Compared to our findings for the NaCl buffer, we observed opposite effects under the $CaCl_2$ conditions. Our results show a significant decrease in *NOX1* and *NOX4* associated signaling pathways, reduced unfolded protein response signaling, and attenuated apoptosis signaling (Figure 4.7C). Together, these data would suggest less cell death under these conditions. However, we also observed a significant increase in luminal calcium signaling pathways that were significantly correlated with increased cell death and a concurrent increase in signaling pathways associated with the translation of stress related mRNA (Figure 4.7C). These data are consistent with the increase in *EIF5B* and 60S Ribosomal subunit signaling that was also observed (Figure 4.7C). The increases in these pathways resulted in an increase in necroptosis signaling, rather than apoptosis, in the $CaCl_2$ conditions

following H-FIRE (Figure 4.7C).

4.5 Discussion

We have demonstrated that adjuvant calcium used in combination with H-FIRE treatment enhances ablation areas and reduces both reversible and irreversible electroporation thresholds. Pulse durations shorter than 10 μs require the use of adjuvant calcium to produce ablations larger than 5 mm^2 in vitro (Figure 4.3). It has been shown that shorter, bipolar pulses are less efficient at permeabilizing cells compared to longer, monopolar pulses [72, 151]. Longer pulse durations cause an increase in the number and/or size of pores that are created in the membrane [72, 71, 100], enhancing permeabilization and potentially cell death. Interestingly, the 5-1-5 waveform resulted in the largest increase of ablation area between $CaCl_2$ and NaCl treatments. The 5-1-5 waveform may be maximizing permeabilization, while minimizing cell death from irreversible electroporation in the absence of calcium. To confirm this, it was necessary to characterize the reversible ablation areas and thresholds.

When $CaCl_2$ was used, the difference between reversible and irreversible electroporation areas decreased for all waveforms (Figure 4.5). This result further supports our hypothesis that cells which are reversibly electroporated are driven to undergo cell death in the presence of adjuvant calcium, therefore enhancing the area of irreversible electroporation. As pulse duration increased, the difference between reversible and irreversible electroporation areas also decreased for all conditions, suggesting that there is a transition to a higher number of cells dying. The difference between irreversible and reversible electroporation was highest for 1 mM NaCl and the 5-1-5 waveform confirming that permeabilization was maximized while cell death was minimized.

Results suggest that the cell death response to $CaCl_2$ is dose dependent for shorter pulse durations (1-5 μs). Figure 4.5 shows that for 5 mM $CaCl_2$, irreversible ablation areas are almost the same as reversible electroporation areas whereas for 1 mM $CaCl_2$, the irreversible areas are much smaller.

Cells may also be able to pump lower concentrations of calcium out through the plasma membrane ATPase pump [18, 41]. In addition, Ciobanu et al., demonstrated that cells electroporated in the presence of calcium (< 0.5 mM) had a lower relative fluorescence emission when exposed to PI five minutes post pulse [152] than cells that were electroporated without calcium, suggesting that low levels of calcium may aid in the resealing process [153]. The dose dependence seen in our results seems to diminish as pulse duration increases. When a 10-1-10 waveform is used, the cells may be electroporated to an extent that they cannot recover and the difference in ablation area for the two calcium concentrations decreases, suggesting that there is a transition to a higher number of cells being irreversibly electroporated.

Using a 10-1-10 waveform with $CaCl_2$ decreases the cell death threshold (771 $\pm$ 129 V/cm) to a value comparable to an IRE treatment without $CaCl_2$ (698 $\pm$ 103 V/cm). This finding may allow researchers to ablate areas similar in size to traditional IRE treatments, while eliminating some of the side effects associated with IRE such as conductivity changes and dependence on tissue geometry [111]. It has been shown that decreasing pulse duration as well as the use of bipolar pulses leads to a decrease in nerve excitation [154], however elimination of muscle contractions using a 10-1-10 waveform is yet to be confirmed. In addition, using a 10 μs waveform may eliminate the need for custom built electronics to deliver the pulses, therefore reducing the complexity of pulse generator design and cost of H-FIRE treatment.

We found that $CaCl_2$ buffer lowers the electroporation threshold, causing larger reversible electroporation zones compared to NaCl buffer (Figure 4.4). These results match the findings of Pakhomova et al. where the authors found that cells treated in a sucrose and NaCl buffer were rescued from cell swelling and early cell death while showing increased caspase activation [155, 156]. The authors hypothesized that sucrose is unable to enter pores formed during nsPEF treatment, therefore preventing cell uptake of water and subsequent rupture of the membrane. When buffer contained both $CaCl_2$ and sucrose, blebbing of the membrane was suppressed initially, followed by sudden bleb formation and massive uptake of propidium iodide leading to necrosis. Sucrose prevented cell swelling initially, but over time as more $CaCl_2$ entered the cell, existing pores either

expanded or new large pores formed, allowing sucrose and PI to enter the cell. Therefore, the authors concluded that $CaCl_2$ causes cell death through a non-osmotic mechanism, although they did not specify the biological mechanism responsible. It is important to note that Pakhomova et al., used trapezoidal pulses with a duration of 300 ns whereas our pulses are square wave with longer duration (1-10 μs). It is known that pulse shape as well as duration affects pore formation during electroporation, therefore it is possible that the dynamics of $CaCl_2$ and sucrose/NaCl uptake are different during H-FIRE treatment. However, we do see similar results in terms of $CaCl_2$ causing more permeabilization than the NaCl/sucrose solution. This similarity may suggest that pore formation during H-FIRE treatment may be similar to nsPEF treatment, however, to directly compare our results we would need to monitor cell swelling and uptake in response to H-FIRE treatment.

To investigate the differences in cellular response to $CaCl_2$ and NaCl conditions, we analyzed the regulation of calcium signaling genes. The genes chosen were pre-selected and validated by the vendor (Qiagen) to provide the broadest overview of calcium signaling pathways using a commercially available array. When the data are processed and evaluated using the vendors software and Ingenuity Pathway Analysis (also from Qiagen), the 89 genes selected are optimized to identify biological pathways and functions impacted by treatment. Our gene expression profiling identified several distinct biological functions that were significantly altered and correlated with NaCl or $CaCl_2$ environments. Under the NaCl conditions, the U251 cells were more resistant to cell death than cells treated in $CaCl_2$ conditions due in part to the downregulation of *EIF5B* and the eventual reduction in stress associated mRNA translation following H-FIRE in the NaCl conditions. The increase in *NOX1* and *NOX4* signaling should have increased cell death through increased ROS in these cells under these conditions. However, we paradoxically observed minimal ROS signaling, indeed even an attenuation (Figure 4.7). This is likely due to the requirement for Ca^{2+} for *NOX1* signaling. In the absence of calcium, it is likely that the cell death effects associated with *NOX1* and ROS production are minimized [157]. Thus, we are likely observing increased gene transcription of *NOX1* as a compensatory mechanism following H-FIRE in cells attempting to initiate ROS signaling. This is also likely associated with the increase in *NOX4* transcription. Unlike *NOX1*,

NOX4 is constitutively active and likely upregulated at the expression level as compensation for the low calcium conditions where it can ultimately compensate for the defect in *NOX1* signaling [157]. However, this delay in *NOX4* signaling would be predicted to stall apoptosis in our models, as reflected in the reduced levels of cell death following H-FIRE treatment. In addition to its roles in cell death, increased expression of *NOX1* also plays a role in cell proliferation where it has been demonstrated to mediate cell growth and transformation when overexpressed [158]. *NOX1* regulation also targets cyclin D1 and ERK1/2 activity [159]. Thus, in addition to reduced cell death in the NaCl conditions, we are also likely observing some differences associated with increased cell proliferation and pro-survival signaling. Interestingly, Pakhomova et al. did not observe a cell sparing 24 hours after treatment with NaCl and sucrose buffer, which does not appear consistent with our findings. Perhaps the pulse parameters or cell type that we have chosen to study are responsible for this contradiction. Previous research has shown that the mechanism of cell death may differ between cell types as well as pulse strength and duration [150, 82].

Conversely, the U251 cells were more sensitive to H-FIRE treatment in the $CaCl_2$ conditions than they were in the NaCl conditions. This is due, in part, to the upregulation of *EIF5B* and the eventual induction of necroptosis. *EIF5B* represents a regulatory node in cancer cells, whereby under some conditions increased gene expression is associated with cell evasion of apoptosis by promoting the translation of pro-survival proteins, while under other conditions overexpression promotes cell cycle defects resulting in cell death in response to stress [160, 161]. Our data is consistent with the later findings, whereby in conditions of calcium enrichment followed by cellular stress and damage associated with H-FIRE, we observe significantly increased cell death. Likewise, the anti-apoptotic functions of *EIF5B*, associated with the upregulation of *XIAP* and *BCL-XL*, may function as a significant driver of the increased necroptosis signaling as the predominate form of early cell death in the U251 cells following H-FIRE in the $CaCl_2$ conditions (Figure 4.7). Finally, it should be noted that dysregulated increases in intracellular calcium can promote cell death through necrosis following cellular damage and/or stress [162]. One limitation of our study is that we analyzed gene expression of cells that were exposed to a range of electric field magnitudes which may be

experiencing differential gene expression. To accommodate for this limitation, we normalized our results to sham controls to observe general trends. However, in future work it may be useful to investigate gene expression in response to a uniform electric field magnitude. Such investigations would allow for precise characterization of cell response for different electric field strengths. Our results can be used to inform future studies as to which electric field magnitudes may be of interest for future investigations into H-FIRE treatment with and without calcium.

While the exact mechanism distinguishing cell death for NaCl and $CaCl_2$ still needs further investigation, several molecular dynamics studies have shown that calcium interacts with and can even bind to the lipid head groups of the membrane [91]. These interactions may influence pore formation, pore lifetime, and pore resealing [91, 163]. It has also recently been demonstrated that lipid composition varies between cell type and can further influence pore formation and interaction of ions with the membrane [164]. Furthermore, previous studies have shown that an excess of intracellular calcium may activate proteases and phospholipases which further contribute to the lifetime of pores and exacerbate membrane damage, subsequently preventing resealing of the membrane [129].

4.6 Conclusion

We have demonstrated successful enhancement of H-FIRE ablations using adjuvant calcium. Utilizing a 10-1-10 H-FIRE waveform with 1 mM $CaCl_2$ reduces the irreversible electroporation threshold to a value comparable to standard IRE treatments without calcium, therefore enhancing the efficacy of H-FIRE without increasing the applied voltage. This finding may potentially allow clinicians to use commercially available generators instead of custom-made generators for treatment, simplifying translation to the clinic. We have also uncovered several distinct biological functions that were significantly altered and correlated with NaCl or $CaCl_2$ environments.

Calcium electroporation has recently been investigated in several clinical trials for cutaneous

metastases, colon as well as head and neck cancer [165, 166, 44]. We envision using calcium H-FIRE treatment in vivo in a similar fashion to enhance ablation size by injecting calcium chloride directly into the tumor and delivering H-FIRE pulses through needle electrodes inserted into the tumor. However, translating to the clinic still presents challenges such as optimizing $CaCl_2$ concentration as well as injection volume as to avoid necrosis of surrounding tissue and hypercalcemia.

Following our observation that sucrose and NaCl may prevent cell death, we also envision injecting a buffer that contains sucrose and lacks calcium to control electroporation treatments in vivo, therefore preserving tissue that is outside of the desired ablation zone. This sucrose buffer could be injected into blood vessels near tumors prior to treatment to prevent electroporation of the endothelial cells in the vessel. Spatial control over ablations and sparing of blood vessels may be beneficial for treatments such as blood-brain barrier disruption. Electrodes may be designed to inject $CaCl_2$ into the tumor during treatment while also delivering NaCl and sucrose buffer on the tumor borders to protect surrounding tissue. Venofer is an Iron Sucrose solution (300 mg/ml sucrose w/v) that is administered intravenously and utilized to treat anemia. Side effects are relatively minor and include muscle cramps, nausea, vomiting, and dizziness. Most side effects are associated with the speed of administration. However, it would be reasonable to utilize something like Venofer to increase sucrose concentrations as supported by the data provided here.

In addition, these results suggest that adding calcium to electroporation buffers prior to gene transfection procedures may enhance permeabilization and therefore cell uptake [41]. Our study is the first to demonstrate enhancement of H-FIRE ablations using adjuvant calcium, in addition to identifying key genes and signaling pathways responsible for differences in cell death with and without calcium.

Chapter 5

Development of fibrin microgels for single cell analysis and tissue engineering applications

5.1 Abstract

[1] Droplet microfluidics has enabled creation of micron scale hydrogels (microgels) for single cell analysis, long-term cell culture, and tissue engineering applications. Here, we have shown successful encapsulation of mouse mammary gland cancer and human cerebral endothelial cells in fibrin microgels using a flow-focusing microfluidic device. Microgels were monodisperse and their diameter tuned to range from 56 μm to 85 μm with nearly 80% of cells surviving up to 3 days following encapsulation. Creating a thin shell of oil (11 $\pm$ 3.0 μm) around fibrin microgels using a double emulsion device prevented them from clumping in cell culture media, keeping them dispersed for 7 days. Microgel microstructure was varied using transglutaminase and was shown to prevent fibrin degradation in the presence of aggressive cancer cells. Microgels were also fabricated using Matrigel and a fibrin-alginate blend, demonstrating their versatility. The ability to fabricate fibrin microgels in a tunable, controlled, and high-throughput fashion may enable their use for a wide range of single cell analysis studies as well as tissue engineering applications.

[1]This work was performed under the auspices of the U.S. Department of Energy by Lawrence Livermore National Laboratory under Contract DE-AC52-07NA27344.LLNL-MI-798105

5.2 Introduction

Single cell analysis has become a key technique for understanding the origins and behavior of tumors. As Robert Weinberg described in his "Hallmarks of Cancer" [1], genetic mutations can kick off a cascade of events that result in altered gene expression, altered protein structure and function, as well as altered signaling pathways. These alterations can vary from cell to cell even within the same tumor, let alone patient, producing a degree of complexity that is difficult to sort out using methods that rely on bulk samples. Furthermore, intratumoral heterogeneity leads to therapy resistance since there exists different tumor cell populations within one tumor, making it difficult to establish a unified target. In recent years, genomic, transriptomic, and proteomic tools have been created that allow researchers to begin this characterization at the single cell level, revealing key features of tumor evolution and diversity [167, 168].

Single cell analysis is challenging. One challenge lies in separating single cells from large tissue samples such as those taken during biopsies or surgical resection. Typical methods rely on fluorescence activated cell sorting (FACS), micropipetting, and serial dilution. Micro-pipetting and serial dilution are labor intensive and low throughput whereas FACS provides higher-throughput sorting, but requires specialized equipment and may be expensive [169]. In addition, cells contain minute levels of DNA (6-12 pg) and RNA (10-50 pg), requiring amplification to produce enough material for analysis [167]. Performing this amplification in microtiter plates requires a large amount of reagents, making high-throughput studies costly.

Droplet microfluidics provides an alternative to these methods for single cell analysis [170, 171, 172, 173]. Platforms such as the inDrops [174, 175], Drop-seq [176], and 10X Genomics Chromium microfluidic systems utilize droplets to carry out single cell RNA-seq. These systems allow for high efficiency cell encapsulation, the use of less reagents and therefore lower costs, as well as high-throughput generation of sequencing libraries. Furthermore, droplets can be produced at high rates, their size easily tuned, and downstream splitting and sorting is possible.

Although droplet microfluidics has proven to be a powerful tool for omics studies, there are several

limitations. Once cells are lysed inside the droplets and DNA or RNA content released, it is difficult to perform washing steps to rid the droplet of cell debris. It is also not possible to carry out long-term studies of adherent cells in their native 3D microenvironment [177]. Utilizing micron scale hydrogels (microgels) provides a solution. Bigdeli et al., encapsulated cells in alginate microgels for direct PCR and whole genome amplification [178]. Rakszewska et al., utilized functionalized hydrogel beads to capture mRNA that is released from lysed cells.

Microfluidic droplets have also been utilized for single cell electroporation. Zhang et al., developed a microfluidic platform capable of electroporating cells at a range of applied electric field magnitudes (2000-3500 V/cm) and durations (0.37-21.6 ms). As applied voltage increased from 4.1V to 7.1V, viability of Chinese Hamster Ovary (CHO) cells decreased from 68% to 14%. CHO cells were also succesfully transfected with a plasmid vector coding enhanced green fluorescent protein (EGFP).

In addition to single cell analysis, microgels have also been used for cell culture [179, 180, 181, 182], spheroid formation [182], stem cell differentiation [183, 184, 185], drug studies [171], and other tissue engineering applications. Allazetta et al., demonstrated that microgel composition can be easily tuned by adjusting device flow rates, creating a library of different microenvironments with which to culture and study cells [186]. Brouzes et al., developed an on chip cell cytoxicity screen by optically encoding different concentrations of the drug mitomycin C with the dye Alexa Fluor 680 R-phycoerythrin [171]. A dose-response curve was generated by binning each drug concentration by its corresponding dye concentration.

Griffin et al., developed a method to anneal microgels together to create a porous, injectable scaffold that promoted faster wound closure (40% in 7 days) and re-epithelialization in mice than a nonporous control scaffold (10% in 7 days) [187]. Void spaces that formed between the annealed microgels allowed enhanced perfusion of the tissue and enhanced proliferation and retention of stem cells in a mouse model when compared to a control bulk gel [188]. The material of the microgels can also be tuned to enhance stem cell function in addition to decoupling pore size and

scaffold stiffness [189]. Microgels have also been shown to uncouple a tissue's micro- and macro environments [190] enabling the creation of multimaterial tissue models. Poly(ethylene glycol) diacrylate (PEGDA) microgels were incorporated into different bulk materials (collagen, alginate, alginate-GelMA, PEGDA) using several techniques such as photolithography, emulsification, injection molding, extrusion printing, and wet spinning. Matsunaga et al., utilized cell coated collagen microgels to create millimeter thick tissues that showed no signs of necrosis after 30 hours [191].

Here, I have shown successful encapsulation of cancer and endothelial cells in fibrin microgels. Fibrin has been shown to be an excellent biomaterial due to its permissive nature and degradability. Fibrin can be easily modified to incorporate growth factors as well as change its structure and mechanical properties for specific applications such as stem cell differentiation [192, 193, 194], nerve regeneration [195], angiogenesis [196], and cancer [197]. To my knowledge, fibrin microgels have not been fabricated using microfluidics previously. Therefore, *I hypothesize that the ability to fabricate fibrin microgels in a tunable, controlled, and high-throughput fashion may enable their use for a wide range of single cell analysis studies as well as tissue engineering applications.*

5.3 Materials and Methods

5.3.1 Microfluidic device design

Two microfluidic devices were used in this investigation. Device 1 encapsulates cells in fibrin microgels and the device consists of three stages (Figure 5.1A). In the encapsulation stage, two aqueous inlets (fibrin components) converge into a flow-focusing orifice, 30 μm in width, where they intersect an immiscible, continuous oil phase. Microgel size is dictated by pressure, surface tension, inertial, and viscous forces and can be tuned by either adjusting the flow rates of the different phases, or by changing the geometry of the orifice. There are several regimes of droplet production in microfluidic flow-focusing devices. At slower flow rates, droplets fill the orifice,

blocking downstream flow which results in a pressure buildup in the droplet. The Laplace pressure at the neck of the droplet is larger than at the front of the droplet since the diameter here is smaller and Laplace pressure varies inversely with diameter [198]. As a result of this pressure imbalance, fluid rushes into the front of the droplet, causing it to break off. This is known as the squeezing regime. Here, the oil flow rate and orifice geometry determine droplet diameter. At higher flow rates, viscous forces deform the interface of the droplet, carrying it downstream where it then breaks off due to capillary wave instabilities, resulting in smaller droplets. This regime is known as the dripping regime and droplet diameter is smaller than in the squeezing regime.

The fibrin components (fibrinogen and thrombin) in the microgels are then mixed by chaotic advection induced by a section of curved channel (mixing stage) that is 30 μm in width and consists of 10 turns. Since the microgels are in contact with the walls of the device, the fibrinogen and thrombin recirculate in the droplet, reducing the length scale over which diffusion must act (known as striation length) exponentially with each turn from $\sim$ 30 μm to $\sim$ 0.029 μm. Scaling analysis has been previously used to define the mixing time in droplets in a curved channel as $t_{mix} = \frac{aw}{U} log(Pe)$ where w is the cross-sectional dimension of the channel, a is the length of the droplet normalized to w, U is velocity of the droplet and Pe is the Peclet number. For the flow rates used in this study, t_{mix} is $\sim$ 0.008 seconds. Calculating the residence time for the curved section of our device gives $t_{residence} \sim 0.216$ seconds, therefore microgels will be adequately mixed upon exiting the curved section.

Gelation of microgels is then initiated in a serpentine section with a residence time of 0.838 seconds. Although this is not enough time for the fibrin to fully gel, it allows the microgels to become more stable and resistant to deformation before being collected in a microcentrifuge tube where gelation is completed. All other channels are 60 µm wide and the entire device is 30 µm tall.

Device 2 was used to prevent hydrophobic interactions between microgels that caused them to clump in cell culture media by creating a thin droplet of oil around the fibrin in a water-oil-water (w/o/w) double emulsion. Here, fibrin is the internal phase, a thin shell of oil encapsulates the fibrin

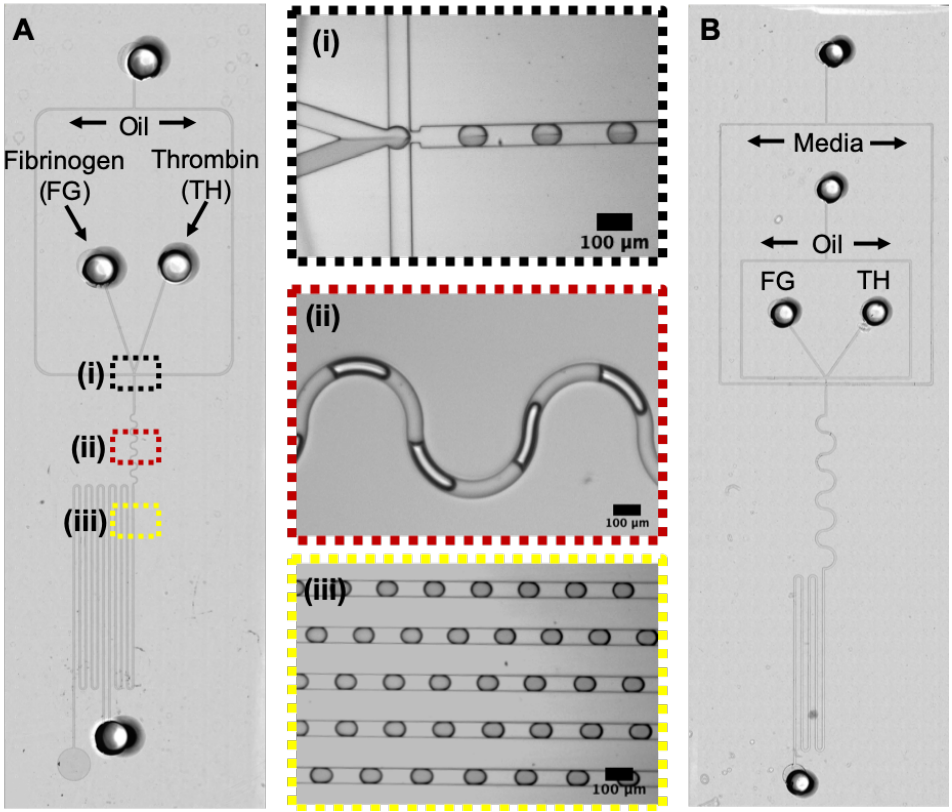

Figure 5.1: Design of encapsulation and double emulsion microfluidic devices used in this study. A) Device 1 encapsulated cells in fibrin microgels for cell viability testing and the device consists of three stages: (i) encapsulation stage, (ii) mixing stage, (iii) gelation stage. **B)** Device 2 was used to create a water-oil-water (w/o/w) double emulsion of fibrin microgels surrounded by a thin oil shell to prevent the microgels from sticking and clumping while cultured in cell media.

and both are surrounded by cell culture media (Figure 5.1B). The design of this device follows a previously published paper that was used to create a double emulsion in a one and two-step process [199]. The dimensionless numbers that dictate droplet breakup are the Weber number of the inner phase ($We_{in} = \rho v_{in}^2 l/\gamma$) and the Capillary number of the outer phase ($Ca_{out} = \mu v_{out}/\gamma$) where ρ is the density and v_{in} is the velocity of inner fluid, l is the diameter of the channel, μ is the viscosity and v_{out} is the velocity of the outer fluid, and γ the surface tension. When $(We_{in}, Ca_{out}) < 1$, a dripping instability occurs and the the inner phase will break into drops creating a double emulsion in a two-step process. When $(We_{in}, Ca_{out}) > 1$, inertial and viscous forces dominate and the inner phase will create a coaxial jet which is then pinched into a double emulsion by the oil phase in a one-step process. The first orifice used to form the fibrin microgels was 30 μm wide and the

second, used to create the oil shell, was 50 μm wide. The mixing and serpentine sections of the double emulsion device were designed to match residence and mixing times of the encapsulation device. All other channels had a width of 100 μm and the height of the device was 50 μm.

5.3.2 Device fabrication

Silicon molds used to create polydimethylsiloxane (PDMS, SYLGARDTM 184, Dow Corning) devices were fabricated in a cleanroom using photolithograhy. Four inch, 525 μm thick silicon wafers were cleaned using O_2 plasma ash for 2 min at 150W. Wafers were then coated with Omnicoat ^{TM} for increased adhesion at 2750 rpm for 30 seconds and then baked at 200°C for 1 minute to dehydrate. SU-8 2025 was then spin coated onto the wafers at 1750 rpm for 30 seconds and baked at 65°C for 90 seconds, then at 95°C for 7 minutes. Wafers were exposed using a Heidelberg Maskless Aligner at a dose of 320 mJ/cm^2. Wafers were then baked at 65°C for 1 minute, then 95°C for 6 minutes and 10 seconds followed by developing with SU-8 developer for 5 min, agitating every 30 seconds. Finally, wafers were surface treated with silane to prevent surface adhesion prior to casting PDMS.

PDMS was mixed at a 10:1 ratio of polymer base to curing agent and degassed in a vacuum chamber for 30 minutes. PDMS was then poured onto the wafers and cured in an oven at 65°C for three hours. After curing, devices were cut out and inlets punched using a 1 mm biopsy punch (Integra^{TM} Miltex®). Devices were cleaned by blowing nitrogen gas across them and into the punched holes. Packaging tape was then used to lift off any remaining debris. Devices were then plasma bonded to a flat piece of PDMS by exposing to air plasma for 30 seconds (Harrick Plasma, PDC-001-HP). Devices were kept in an oven at 60°C until use.

Device design 2 was selectively surface treated using 1% polyvinyl alcohol (87-90% hydrolyzed 30,000-70,000 MW, Sigma Aldrich) solution to render the media channel hydrophilic following a previously published protocol [200]. Polyvinyl alcohol (PVA) solution was made by dissolving 1g in deionized water at room temperature for 30 minutes using a magnetic stir bar. The solution

was then heated to 90°C and stirred overnight. The PVA solution was filtered using a 0.22 μm filter to remove any insoluble particles. To treat the devices, the fibrinogen and thrombin inlets were blocked with a plug of PDMS while the PVA solution was injected through the outlet at a flow rate of 1 μL/min using a 1 mL syringe. To prevent the PVA solution from entering the oil channel and orifice, air was injected manually into the oil inlet using a 5 mL syringe. PVA solution was allowed to flood the media channel for 10 minutes before ejecting it using air from the 5 mL syringe. Devices were then heated to evaporate any remaining PVA for 5 minutes at 110°C. This process was repeated 3x and devices were stored at room temperature for one day prior to use.

5.3.3 Cell culture

Human cerebral microvascular endothelial cells (hCMEC/D3, Millipore Sigma, SCC066) were used for cell encapsulation and viability studies. Cells were maintained in EndoGRO ^{TM}-MV complete growth media (Millipore Sigma, SCME004) supplemented with 1 ng/mL FGF-2 (Millipore Sigma, GF003) at 37°C and 5% $C0_2$. Cells were routinely passaged when 80-90% confluent following the vendor's protocol.

The 4T1 mouse mammary gland cancer immortalized cell line (ATCC, CRL-2539) was used to study degradation of fibrin gels and cell encapsulation in the w/o/w double emulsions. Cells were maintained in RPMI-1640 (ATCC, 30-2001) supplemented with 10% fetal bovine serum (ATCC, 30-2020) and 1% penicillin-streptomycin (Gibco). Cells were routinely passaged at 80-90% confluence.

5.3.4 Fibrin microgel formation

To form fibrin microgels without cells, 20 mg/mL fibrinogen (Millipore Sigma, F8630) and 2 U/mL thrombin (Millipore Sigma) were injected into the encapsulation device using 1 mL Luer-Lock syringes (Becton Dickinson) at a flow rate of 1 μL/min (Harvard Apparatus, Pump 11 Elite).

These concentrations ensured that the final concentration of fibrin within each microgel consisted of 10 mg/mL fibrinogen and 1 U/mL thrombin. Fluorescently labeled fibrinogen (Alexa Fluor 594, ThermoFisher Scientific) was incorporated into the fibrinogen solution at 1% (w/w) concentration to enable tracking of microgels downstream. Fibrinogen was suspended in phosphate buffered saline without calcium or magnesium (PBS, Gibco) and thrombin was suspended in a 5 mM $CaCl_2$ solution. The $CaCl_2$ solution was made in deionized water with 250 mM sucrose, 1 mM $MgCl_2$, and 10 mM HEPES buffer. Flangeless fittings (Cheminert, CFL-1G) were used to secure Tygon tubing (Cole Parmer) with 1/50" inner diameter and 1/16" outer diameter to the syringe with a Leur Lock adapter (IDEX). 2% Pico-surf^{TM} 1 in Novec 7500 (Sphere Fluidics) was used as the continuous phase fluid and was injected using a 1 mL syringe at 4 μL/min. Microgels were collected using a microcentrifuge tube filled with 500 μL Pico-surf.

To characterize microgel size for different flow rates, the continuous phase (oil) flow rate (Q_c) was increased while the dispersed phase (fibrinogen and thrombin) flow rate (Q_d) was held constant. Microgel formation was visualized on a Nikon Eclipse TE2000-U inverted microscope using a 20x objective and high-speed camera (Photron Fastcam SA-X2). Videos were recorded at 12,500 fps and microgel diameters were measured using ImageJ (National Institutes of Health, Bethesda, Maryland). Fifty microgels from 3 separate devices were measured for each condition.

5.3.5 Cell encapsulation in fibrin microgels

To prepare cells for encapsulation, cells were passaged according to the vendor's instructions and resuspended in media. Cells were then centrifuged at 200g for 5 min. The media was aspirated and cells were resuspended in PBS with 2% bovine serum albumin (BSA, ThermoFisher Scientific). Cells were washed with 2% BSA in PBS twice to ensure removal of all media prior to adding the cells to the fibrinogen to prevent clumping of the cells and premature gelation of the fibrinogen. After washing, cells were passed through a 40 μm nylon cell strainer (VWR) to break apart any remaining clumps. Cells were then counted and resuspended in 20 mg/mL fibrinogen at a con-

centration of 8.0x10^6 cells/mL. The process of encapsulating cells in microgels was the same as the previously described protocol (see section 1.3.4) except all devices and tubing were autoclaved to ensure sterility before use. In addition, a 2 mm x 2 mm microstir bar (VWR) was added to the syringe containing the fibrinogen-cell solution. Cells were kept suspended in the fibrinogen solution by manually moving the micro stir bar around in the syringe with a larger stir bar outside of the syringe. Devices were run for 30 minutes on a Olympus IX83 inverted microscope using a high-speed camera (MotionPro X4) to monitor microgel production.

To remove microgels from the oil phase, microgels were washed 3x with fresh Novec 7500 without surfactant. Presence of surfactant can make it more difficult to remove the oil phase when resuspending the microgels in cell culture media. Next microgels were dispensed onto a 40 μm cell strainer that was positioned over a 50 mL conical tube. The microgels were washed with 2 mL of media to remove the oil. The cell strainer was then inverted and microgels were washed and suspended in 2 mL of cell culture media. Microgels were then dispensed into a 96 non-adherent well plate (Corning, CLS3474).

To determine the efficiency of cell encapsulation, two different cell concentrations were tested (4.0x10^6 cells/mL and 8.0x10^6 cells/mL). Optiprep^{TM}, a density gradient medium, was added to the fibrinogen solution at a 20% (v/v) concentration to match the cells' density (1.11 g/mL) to keep them suspended in the fibrinogen solution and prevent them from settling in the tubing and syringe. Microgel production was recorded using a high-speed camera (Photron Fastcam SA-X2). The number of cells encapsulated in microgels was counted along with the total number of microgels. Results were compared to the Poisson distribution expected for the corresponding concentration of cells.

$$P(X = x) = \frac{e^{-\lambda}\lambda^{x}}{x!} \tag{5.1}$$

Here, P is the probability of finding x number of cells in a microgel (0,1,2, etc.) and λ is the mean number of cells in the volume of a microgel, based on the concentration of cells used and the size

of the microgels.

5.3.6 Cell viability

Three days after encapsulation, cell viability was evaluated using 4 μM calcein AM (Life Technologies) and 4 μM ethidium homodimer (ThermoFisher Scientific). Calcein AM is cell permeant and upon entering a live cell, is cleaved by esterases in the cytosol forming non-permeant fluorescent calcein. Ethidium homodimer is cell impermeant and only binds to nucleic acids in cells whose membranes have been compromised, indicating cell death. Microgels were collected from the well plate and placed in a conical tube and the dyes were added. This minimized handling of the microgels since they deform and clump when centrifuged, therefore making it difficult to remove media and stain them in PBS. The staining solution was incubated for 30 min in a cell culture incubator. Microgels were then imaged on a Olympus IX83 inverted microscope using a 4x objective and CCD camera (Olympus XM-10). The total number of live and dead cells were counted.

5.3.7 Encapsulating fibrin microgels in bulk hydrogels

Microgels were then encapsulated in three different bulk hydrogel materials to demonstrate the capability of introducing heterogeneity in tissue engineered models. The same protocol described above (see section 1.3.5) was used to remove the microgels from oil, but instead of washing with cell culture media, microgels were washed and suspended in 2 mL of either 20 mg/mL fibrinogen or 1.2% sodium alginate.

To form fibrin and alginate gels, 125 μL of thrombin or 1.1% $CaCl_2$ solution was dispensed into the wells of a 48 well plate. Then, 125 μL of the microgel-fibrinogen or microgel-alginate solution was added to each well and mixed by pipetting up and down 6 times. Gels were allowed to polymerize for 15 minutes before the addition of 300 μL cell culture media to prevent dehydration.

5.3.8 Fabricating matrigel and fibrin-alginate microgels

Stock Matrigel solution was diluted using PBS to a 5 mg/mL concentration and injected into the encapsulation device at a flow rate of 1.0 μL/min. The oil flow rate used was 4.0 μL/min. The Matrigel solution was kept cold by applying an ice pack to the syringe to prevent premature gelation.

To create fibrin-alginate microgels, sodium alginate and fibrinogen stock solutions were made in a buffer that consisted of 500 mM NaCl, 50 mM KCl, 1 mg/mL glucose, and 2.5M HEPES buffer. Fibrinogen and sodium alginate were mixed at a 1:1 (v/v) ratio to give a final concentration of 20 mg/mL fibrinogen and 1.2% sodium alginate. This solution was injected into the encapsulation device at a flow rate of 1.0 μL/min. Thrombin (2 U/mL) was made in a 1.1% $CaCl_2$ solution and injected into the device at a flow rate of 1.0 μL/min. The oil flow rate was 4.0 μL/min.

5.3.9 Double emulsion microgel formation

Fibrinogen (20 mg/mL) and thrombin (2 U/mL) were injected into the double emulsion device at flow rates of 1.5 μL/min. The continuous phase (2% Picosurf ^{TM} in Novec 7500) was injected at a flow rate of 4.5 μL/min and cell culture media with 0.5% PVA was injected at 8.0 μL/min. The w/o/w emulsions were captured in a microcentrifuge tube filled with 500 μL cell culture media with 0.5% PVA. The double emulsions were visualized using a high speed camera (Photron Fastcam SA-X2) mounted on a Nikon Elipse TE2000-U inverted microscope. Encapsulating cells in the double emulsion device followed the same procedure described in section 1.3.5. Microgel and oil droplet diameters were measured using ImageJ on day 1 and day 7. The data was not normally distributed, so means were compared using the nonparametric Mann-Whitney test ($\alpha = 0.05$) using GraphPad Prism 8.

5.3.10 Impedance correlation spectroscopy analysis of fibrin microstructure

Transglutaminase (TG) is an enzyme known to crosslink proteins in the body. Transglutaminase was added to fibrin to alter microstructure without changing bulk mechanical properties. Impedance correlation spectroscopy is an image processing technique that uses the autocorrelation function to determine number, size, and orientation of structures in an image [201, 202, 203]. The autocorrelation function relies on convolution of the image with itself. In the frequency domain, this calculation can be done by taking the Fourier transform of the image and multiplying it by its complex conjugate. This is the power spectrum of the image and taking the inverse Fourier transform of this gives the autocorrelation function ($G(a,b) = F^{-1}[F(i(x,y) * F(i^*(x,y))]$) where i is the image. The autocorrelation function is then fit to a 2D Gaussian function using nonlinear optimization in MATLAB and parameters such as the amplitude and major and minor axis standard deviations of the Gaussian function can be extracted. Different regions of the autocorrelation function can be fit to the 2D Gaussian function, to analyze the number and size of structures at different scales. It has been shown that amplitude of the autocorrelation (A) varies inversely with the number of structures in the image, whereas the standard deviations give a characteristic length along the major and minor axes of the image. By taking the average of the two standard deviations, an estimation of the size of structures in the image (R) can be determined.

Two fibrin formulations were tested. Fibrin with TG consisted of 10 mg/mL fibrinogen, 1 U/mL thrombin, and 2 mg/mL TG (n = 9). Fibrin without TG consisted of 10 mg/mL fibrinogen and 1 U/mL thrombin without TG (n = 11). Fluorescent fibrinogen at 1% (w/w) was added to the formulations to visualize fibrin microstructure. Images were taken on a Zeiss LSM 700 confocal microscope with a 63x, oil immersion objective. The number of structures (A) and their size (R) were compared statistically. Data was not normally distributed, so the Mann-Whitney nonparametric test ($\alpha = 0.05$) was used to compare the means at the fiber length scale: 8-15 pixels (0.8-1.5 μm).

5.3.11 Rheological characterization

Fibrin with TG (fibrin 1) and fibrin without TG (fibrin 2) were characterized using oscillatory shear rheology. First, isothermal time sweeps were carried out at 24°C, 0.5% strain and 1 Hz frequency. The linear viscoelasitc regime was verified by conducting a strain sweep (0.01% - 100%) at 1 Hz and frequency sweeps were also conducted (0.01-1000 Hz) at 0.5% strain. Time to gelation was calculated as the time when the change in storage modulus was <1%. Storage modulus was determined from frequency sweeps at 1 Hz. Results are presented as means $\pm$ std. A two sample t-test was used to test for significance between means ($\alpha = 0.05$).

5.3.12 Quanitfying fibrin degradation

4T1 mouse mammary gland cancer cells were cultured in fibrin with (n = 4) and without TG (n = 4) at a concentration of 1.5×10^5 cells/mL. Fluorescent fibrinogen (Alexa Fluor 594, ThermoFisher Scientific) was incorporated into both formulations at 1% (w/w) concentration to monitor degraded fibrinogen that has been released from the bulk gel. Fluorescent fibrinogen and spectrophotometry have been previously used to quantify degradation *in vitro* [192, 204, 205]. As fibrin is hydrolyzed, fibrinogen is released into the surrounding media which can be quantified by measuring its absorbance using a spectrophotometer. Acellular fibrin hydrogels served as a negative control (n = 4) while acellular fibrin hydrogels cultured with 4 μg/mL plasmin in the surrounding media served as the positive control (n = 4). The supernatant from each gel was collected every day. Fluorescent content was measured using a spectrophotometer (BioTek Synergy HT) and a 590nm/617nm (excitation/emission) filter set. Background fluorescence (cell culture media) was subtracted from all absorbance measurements, which were then normalized to the negative control (acellular gels). A two-way ANOVA was used to analyze statistical significance followed by Tukey's post hoc analysis to compare significance across groups ($\alpha = 0.05$).

5.4 Results

5.4.1 Microgel fabrication characterization

Microgel fabrication was characterized using device 1 for cell encapsulation. By varying the flow rate ratio between the oil phase (Q_c) and fibrinogen/thrombin (Q_d), microgel size can be tuned (Figure 5.2A). As the ratio between the two flow rates increases, microgel diameter decreases as expected in the squeezing regime of droplet formation. In addition, as the fibrinogen/thrombin flow rate (Q_d) increased, microgel diameter decreased, indicating a transition to the dripping regime of droplet formation. With the device geometry and the flow rates that were used, it was possible to create microgels ranging in diameter from 56 μm to 85 μm. Although there is slight variation across devices, microgels were monodisperse within each device for the two fibrinogen/thrombin flow rates tested (Figure 5.2B). A flow rate ratio of 2 (Q_d = 2.0 μL/min, Q_c = 4.0 μL/min) produced microgels 74 $\pm$ 8 μm in diameter and were selected for cell viability analysis to allow room for the cells to grow and proliferate.

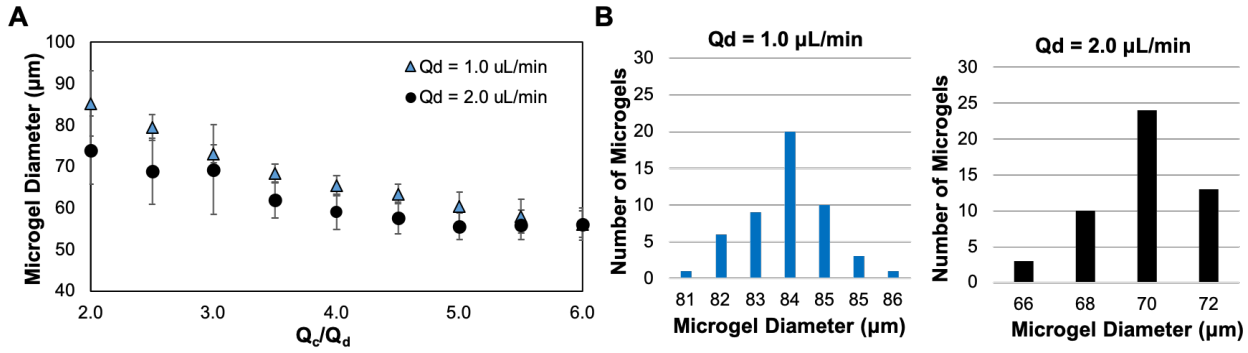

Figure 5.2: Microgels are monodisperse and their size can be tuned. A) Microgel diameter was characterized for different flow rates. Data is shown as means $\pm$ std. **B)** Microgels are monodisperse in diameter for both fibrinogen/thrombin flow rates tested at a flow rate ratio (Q_c/Q_d) of 2. One device from each flow rate group is shown here.

The efficiency of cell encapsulation was lower than predicted by Poisson distribution (Table 5.1). Despite using Optiprep^{TM}, cells began settling in the syringe after 25-30 minutes. In addition, cells tended to clump at the inlet of the device, preventing a dispersed solution of cells from entering

the orifice and instead clumps of cells were encapsulated. Future efforts to enhance encapsulation efficiency will be examined in more detail in the discussion section.

Table 5.1: Experimental and predicted cell encapsulation efficiency

	$4.0x10^6$ cells/mL				$8.0x10^6$ cells/mL			
	0 cell	1 cell	2 cells	3 cells	0 cell	1 cell	2 cells	3 cells
Experimental	94.6 %	4.5%	0.71%	0.24%	76.5%	12.2%	4.8%	2.5%
Predicted	42.8%	36.3%	15.4%	4.4%	18.3%	31.1%	26.4%	14.9%

5.4.2 Cell viability

Human cerebral microvascular endothelial cells (hCMEC/D3) were encapsulated in fibrin microgels and cultured for three days. A live-dead assay was performed to quantitfy the number of cells that survived the encapsulation process. Approximately 80% of the cells survive the process (Figure 5.3), however, quantifying viability was challenging since the endothelial cells grew into spheroids after 3 days making it difficult to count single cells. Instead, clusters of cells were counted as one cell, therefore this result serves as a conservative estimate of the number of live cells.

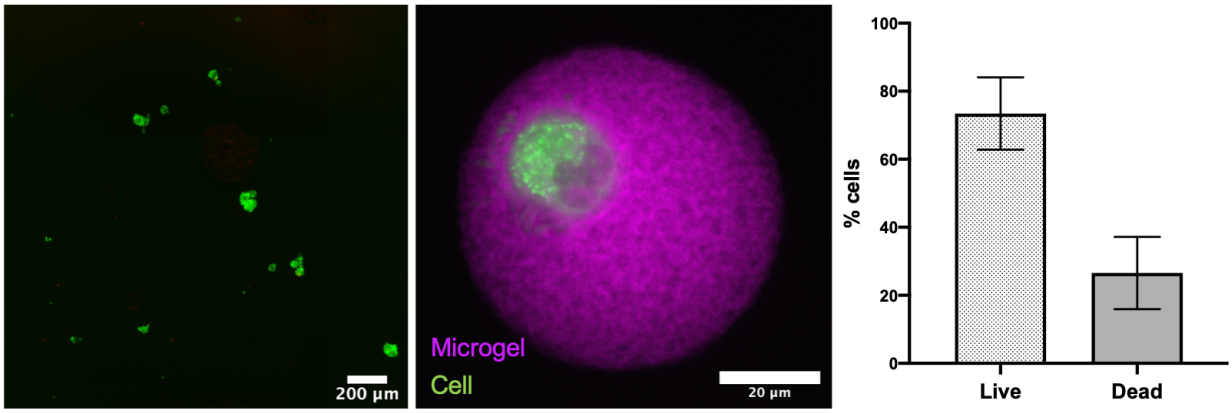

Figure 5.3: Viability analysis demonstrates that the majority of cells survive the encapsulation process. Human cerebral microvascular endothelial cells (hCMEC/D3) were encapsulated at a concentration of 8.0×10^6 cells/mL (n = 3). Cell viability was quantified after 3 days in culture using calcein AM (green) and ethidium homodimer (red, shown here in violet for visualization purposes). Live and dead cells were counted manually. Nearly 80% of cells survived the encapsulation process.

5.4.3 Double emulsion microgels enable easier handling

Culturing the fibrin microgels long-term proved difficult as they tended to clump and stick to each other when placed in cell culture media. Figure 5.4 shows the w/o/w double emulsion that was created to circumvent this problem. Microgels were 56.5 $\pm$ 5.6 μm in diameter while the oil droplets surrounding them were 78.7 $\pm$ 4.1 μm in diameter. The oil layer was 11.1 $\pm$ 3.0 μm thick. In this w/o/w emulsion, it was possible to keep the fibrin microgels in media for 7 days without clumping. Fibrin microgels maintained their size over the 7 days (56.1 $\pm$ 1.8).

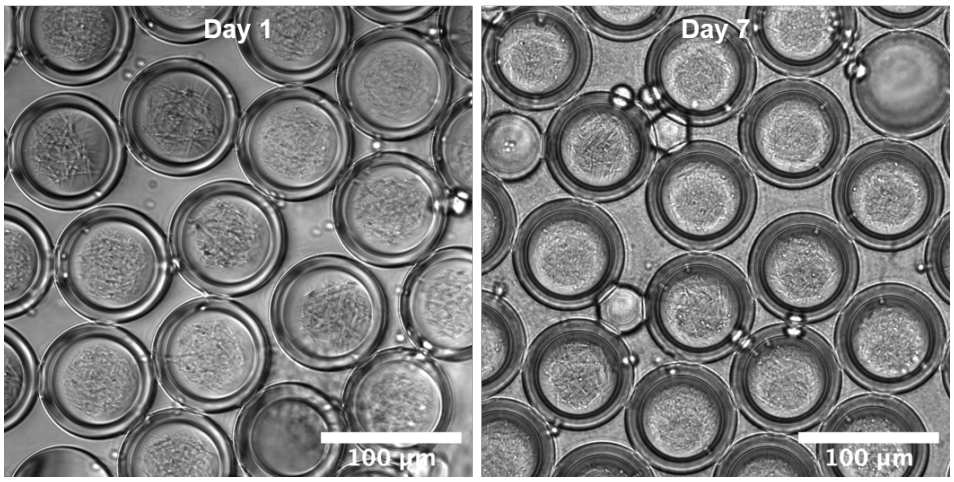

Figure 5.4: Creating a water-oil-water (w/o/w) double emulsion prevents clumping of microgels enabling storage in cell media for 7 days.

4T1 mouse mammary gland cancer cells were successfully encapsulated in the w/o/w double emulsion (Figure 1.5A). However, the double emulsions were not uniform in size due to periodic wetting of the fibrinogen and thrombin at the oil orice (Figure 1.5B).

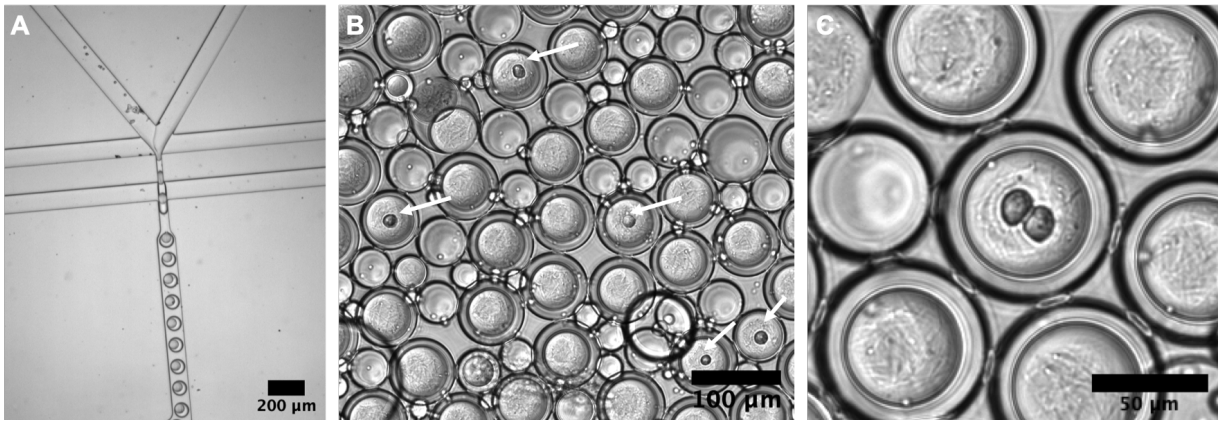

Figure 5.5: 4T1 mammary gland cancer cells encapsulated in w/o/w double emulsion. A) Cell encapsulation process in the double emulsion device. **B)** Cells encapsulated in the double emulsions. The double emulsions were not uniform in size due to wetting of the fibrinogen/thrombin phase at the oil orice. Cell viability needs to be quantified in future work.

5.4.4 Versatility of microgel technology

It was also possible to incorporate fibrin microgels within other biomaterials such as bulk fibrin (Figure 5.6A) and bulk alginate (Figure 5.6B). Alternatively, microgels can be made with materials other than fibrin such as Matrigel (Figure 5.6C) or a blend of materials such as fibrin and alginate (Figure 5.6D). Fibrin-alginate microgels were polydisperse due to the concentration of calcium chloride used (1.1%) which initiated gelation prematurely. This caused a thread of gel material to form between droplets, making it difficult for them to pinch off uniformly.

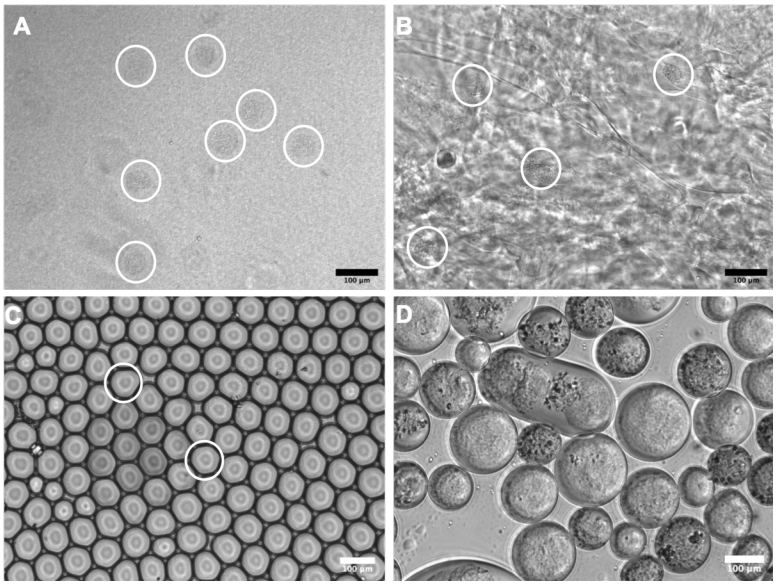

Figure 5.6: Microgels are versatile, allowing for incorporation of different materials (scale bar: 100 μm.) Fibrin microgels were successfully incorporated into bulk hydrogel materials such as fibrin (**A**) and alginate (**B**), demonstrating the ability to introduce heterogeneity in tumor engineered models. White circles indicate the areas where fibrin microgels are located within the bulk hydrogel. Microgels were also made using Matrigel (**C**) and a blend of fibrin-alginate (**D**) demonstrating the diversity of materials that can be used.

5.4.5 Transglutaminase alters microstructure while keeping bulk mechanical properties constant

Transglutaminase (TG) alters fibrin microstructure while keeping bulk mechanical properties constant. Fibrin with TG consisted of large, sparsely packed fibers (Figure 5.7A) while fibrin without

TG contained smaller, more densely packed fibers (Figure 5.7C). This is reflected in the ICS analysis (Table 5.2) which shows that the amplitude (A) of the autocorrelation function was larger for fibrin with TG compared to fibrin without TG at the fiber length scale, 0.8-1.5 μm ($p < 0.0001$). A higher amplitude signifies that there is a lower density of structures and more distinct regions of intensity values in the image. The size of structures (R) was also larger for fibrin with TG than fibrin without TG ($p = 0.0074$). The microstructure differences were preserved when the two formulations were used to create microgels (Figure 5.7 C&F).

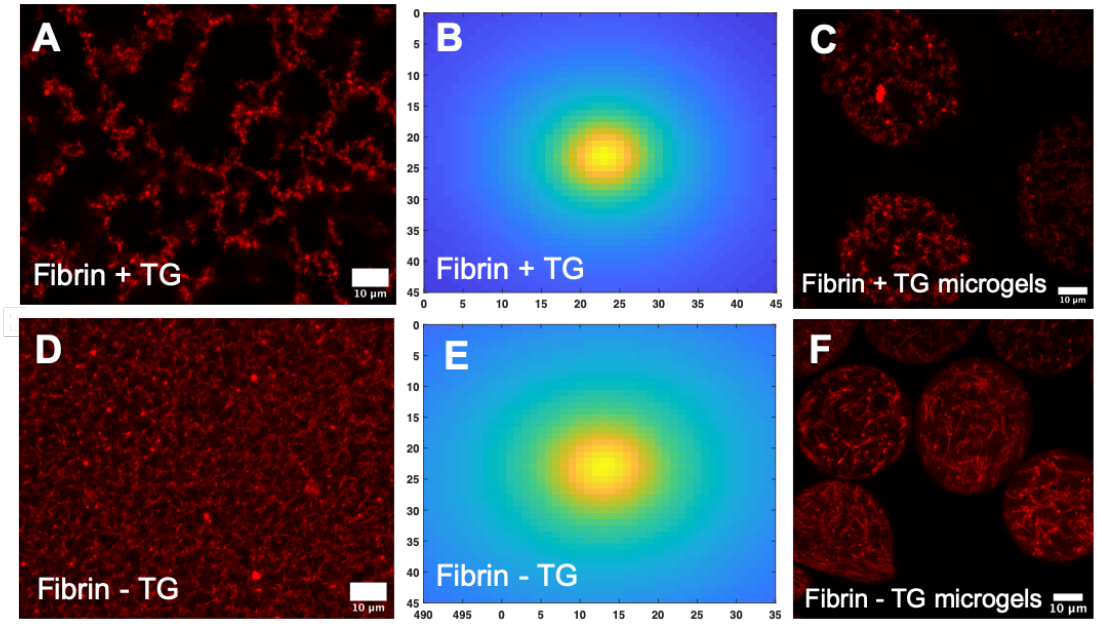

Figure 5.7: Transglutaminase alters fibrin microstructure (scale bar: 10 μm). A) Fibrin with TG seems to have large, densely packed fibers (n = 9). **B)** Autocorrelation function of fibrin with TG. **C)** Fibrin with TG microstructure is maintained in the microgels. **D)** Fibrin without TG has smaller, more densely packed fibers (n = 11). **E)** Autocorrelation function of fibrin without TG. **F)** Fibrin without TG microstructure is maintained in the microgels.

Table 5.2: Impedance correlation spectroscopy analysis demonstrates that fibrin with transglutaminase (TG) has larger structures (higher R) while fibrin without TG has more structures (lower A) at the fiber length scale (0.8 - 1.5 μm).

	A	R
Fibrin + TG	0.87 $\pm$ 0.24	8.27$\pm$ 0.30
Fibrin - TG	0.45 $\pm$ 0.24	7.50 $\pm$ 0.66

Oscillatory shear rheology was used to study the gelation mechanics of fibrin with and without TG. Fibrin with TG (fibrin 1) had a significantly shorter time to gelation (12.76 $\pm$ 2.66 min) than fibrin without TG (fibrin 2) (20.6 $\pm$ 2.05 min) (Figure 5.8A). Fibrin with TG (fibrin1) had a final storage modulus of 204 $\pm$ 104 Pa which was not statistically different than fibrin without TG (fibrin 2) (233 $\pm$ 18 Pa).

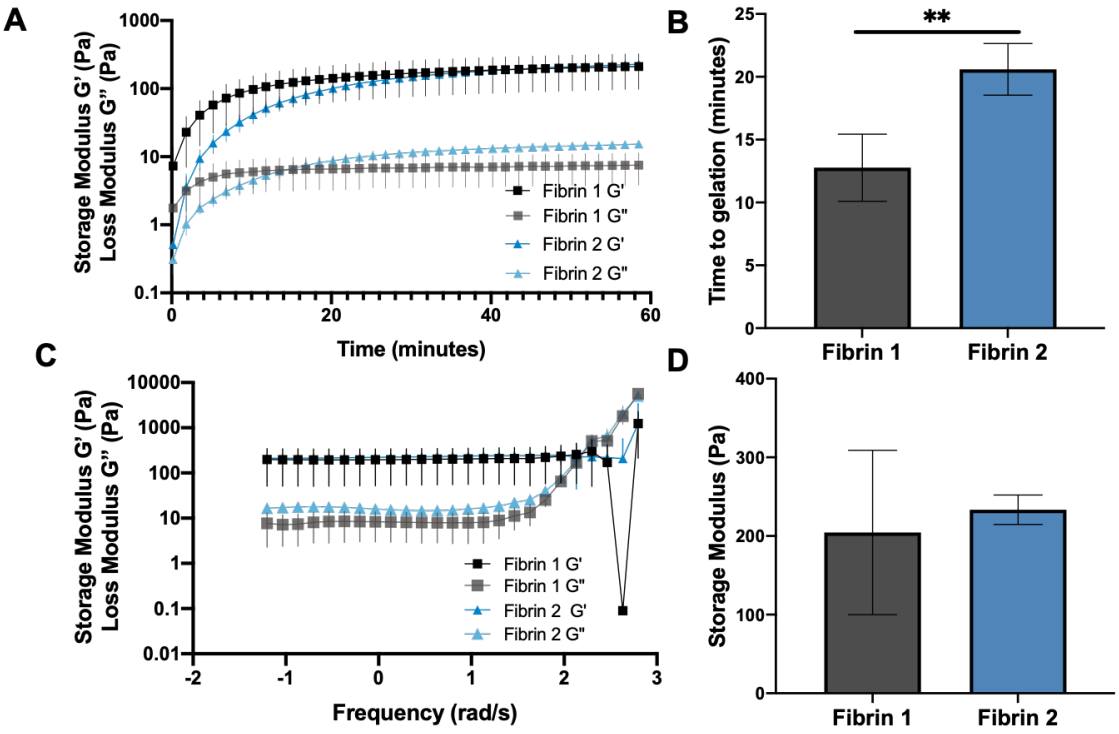

Figure 5.8: Bulk mechanical properties remain similar for fibrin with and without transglutaminase. Results are shown as means ± std. A) Oscillatory shear rheology was used to study the gelation mechanics of fibrin with (fibrin 1) and without (fibrin 2) transglutaminase (TG). Time sweep runs for the fibrin formulations at 0.5% strain, 1 Hz frequency, and 24°C. **B)** Fibrin with TG has a shorter time to gel than fibrin without TG (n = 4, p = 0.006). **c)** Frequency sweeps taken at 0.5% strain and 24°C. **D)** Storage modulus for fibrin with and without TG are similar (n = 3, p = 0.661).

5.4.6 Microstructure can be used to control fibrin degradation in the presence of cells

4T1 mammary gland cancer cells were cultured for four days in the two fibrin formulations to determine if the change in microstructure corresponds to a change in fibrin degradation. Since fibrin without TG has a higher density of fibers, it is more opaque than fibrin with TG which has a lower density of fibers (Figure 5.9A). On day 1 there are a few spots of clearing (spots of higher light intensity indicated by black arrows) already seen in both formulations, however it seems to be more pronounced in fibrin without TG. By day 4, fibrin with TG remained intact

with a slight increase in clearing, suggesting an increase in degradation. Cells cultured in fibrin without TG seem to be both degrading (black arrow) and compacting (white arrow) the gel on day 4, suggesting that the cells are degradting the two gels to a different extent.

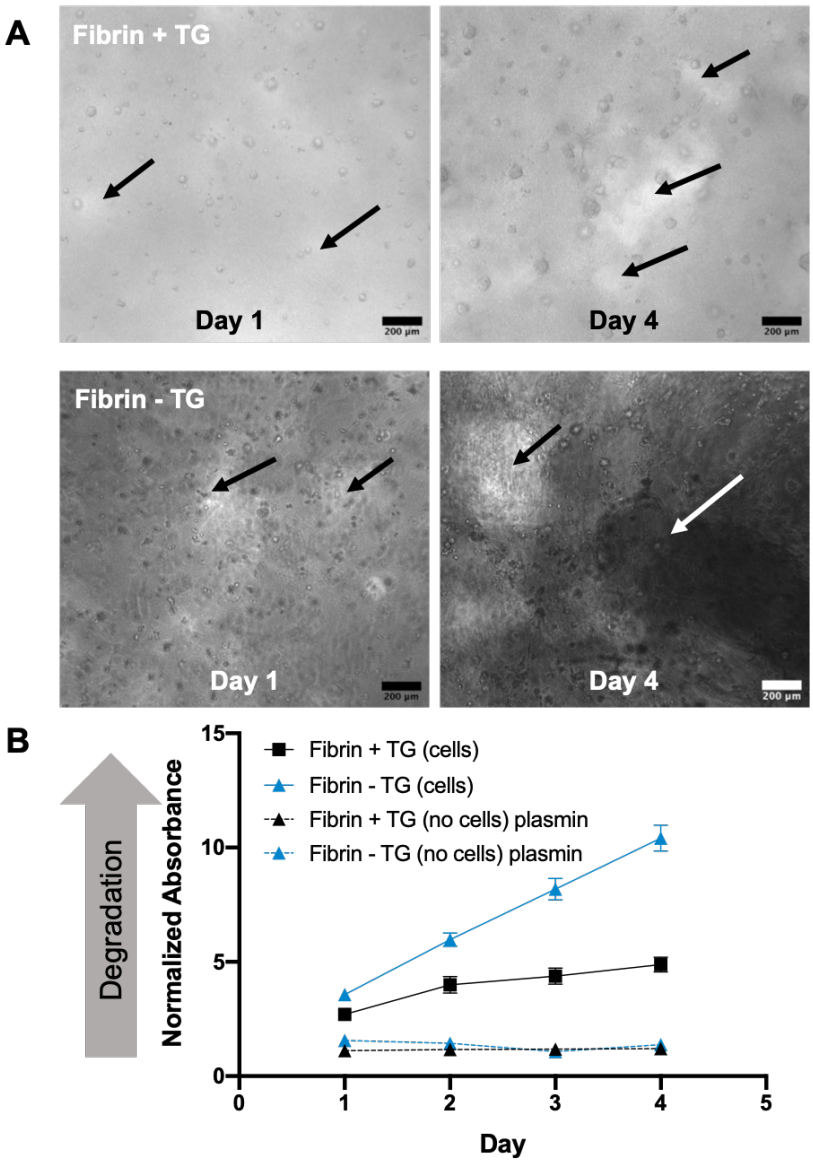

Figure 5.9: Tuning microstructure using transglutaminase changes fibrin degradation. A) 4T1 mouse mammary gland cancer cells were cultured in fibrin with and without transglutaminase (TG). Arrows indicate regions of degradation. By day 4 of culture, the cells seem to be compacting regions of the fibrin gel that lacks TG (white arrow) while also degrading other regions (black arrow). Fibrin with TG also showed some degradation indicated by arrows, but to a lesser extent (Scale bar: 200 μm). **B)** Fluorescent fibrinogen that had been released from the bulk gel was quantified using a spectrophotometer. Fibrin without TG (n = 4) degrades to a greater extent than fibrin with TG (n = 4). Results are shown as normalized means $\pm$ std.

Spectrophotometry measurements indicated that more fluorescent fibrinogen was hydrolyzed and released into the media for fibrin without TG when cultured with cells (Figure 5.9B) than for fibrin with TG. The amount of fluorescent fibrinogen that was hydrolyzed seemed to increase linearly from day 1 to day 4 for fibrin without TG, with almost 10x the amount released from an acellular fibrin hydrogel. On day 4, fibrin with TG released nearly 5x the amount of fibrinogen than its acellular control, indicating that TG prevents cellular degradation. The amount of fibrinogen that was released for fibrin with and without TG were statistically significant from each other for all four days ($p < 0.0001$). Plasmin was used as a positive control, but did not show much more degradation than the acellular control. The degradation of acellular fibrin hydrogels with plasmin for the two formulations were not statistically significant from each other.

5.5 Discussion

We have successfully encapsulated cells in fibrin microgels using a microfluidic flow-focusing device. Using the encapsulation device we were able to fabricate monodisperse microgels and tune their size simply by changing the flow rate ratio between the fibrinogen/thrombin and oil phases. With the flow rates we tested, we were able to fabricate microgels 56 μm to 85 μm in size. It has been shown that for a flow-focusing device, droplet size decreases as the flow rate ratio (Q_c/Q_d) and dispersed phase flow rate increases, matching our results [198]. Ward et al., developed a scaling law that related normalized droplet diameter to the flow rate ratio ($l/a = 2.35(Q_d/Q_c)^{0.25}$) where l is the droplet length and a is the orifice diameter [206]. When we plot our data in this fashion and fit to a power law, we obtain a very similar equation ($l/a = 3.34(Q_d/Q_c)^{0.33}$). To increase the range of diameters of microgels that we can produce, we will need to test a larger range of flow rates (500-2000 μL/hr). From the literature, as the flow rate of the dispersed phase increases, droplet formation transitions from the dripping regime to jetting regime, resulting in smaller droplets. It is also known that orifice diameter and geometry govern microgel size [206, 207, 198], therefore modulating these design features will enable production

of a wider range of microgel diameters.

Our efficiency of cell encapsulation was lower than what was predicted by Poisson distribution, despite using Optiprep ™ to keep the cells suspended in the fibrinogen solution (Table 5.1). It was noticed during experiments that cells did eventually settle in the syringe after $\sim$ 30 minutes. It was also observed that Optiprep ™ changed the microstructure of the microgels, and they appeared to lack their typical fibrous structure. It is known that buffers can have an effect on fibrin formation [208, 209], so Optiprep ™ was eliminated from further experiments and a micro stir bar was used instead to prevent cell settling.

Quantifying cell viability was also challenging since the endothelial cells grew into spheroids 3 days after being encapsulated. There might be several reasons for this happening. First, the cells were sticking to each other during the encapsulation process which may have lead to multiple cells being encapsulated in one microgel. In addition, a larger number of cells entering the orifice may have prevented the fibrin from completely surrounding the cells. Instead, what would result is a clump of cells bound together weakly by a small amount of fibrin. Second, some cells escape the microgels during the process. Since the microgels are placed in a non-adherent well plate after encapsulation, these cells are left to grow in suspension which may result in the formation of spheroids. Therefore, the key to culturing cells long term in the fibrin microgels is to prevent cell settling, clumping, and escape from the microgels.

Several groups have enhanced encapsulation efficiency using active and passive [210, 211, 212] microfluidic methods to order cells before they reach the orifice. Other groups have relied on sorting after encapsulation using both commercially available [213] and microfluidic systems [214, 215, 216, 217]. Instead of manually actuating the microstir bar in the cell solution syringe, groups have attached a magnet to a motor to keep cells suspended [218]. Filters may also be designed into devices to break up cell clumps. In addition, a delayed crosslinking technique was successfully utilized to prevent cell escape [190]. Incorporating these technologies and solutions into our system will enable long-term culture of cells in fibrin microgels for single cell analysis.

Another challenge we faced was removing oil from the microgels and keeping them disperse in cell culture media. We demonstrated that encapsulating the fibrin microgels in droplets of oil allowed us to maintain the microgels in cell culture media for seven days without clumping (Figure 5.4). We also successfully demonstrated cell encapsulation in these double emulsion microgels (Figure 5.5). However, further optimization of the selective PVA surface treatment is needed to prevent wetting of the fibrinogen and thrombin phases at the oil orifice. Cell encapsulation also needs to be optimized and cell viability quantified. In addition, it will be necessary to characterize how the oil shell affects transport of nutrients and cell health. Cai et al., measured transport of molecules out of double emulsions that were being continually perfused [219]. They found that molecules with a lower molecular weight and higher partition coefficient were transported more easily. It will be necessary to characterize transport in our fibrin double emulsions using similar methods. It would also be important to vary the thickness of the oil shell and study how this changes transport. Abate et al., demonstrated that the thickness of the oil shell decreases with increasing velocity of the inner phase and increasing Weber number [199]. From figure 5.5A, it is evident that we are creating double emulsions in a two-step process. Since we are using similar continuous and dispersed phases as Abate et al., we assumed the surface tension between the two phases to be 1-5 mN/m. Calculating the Weber number for our system confirms that it is indeed less than one ($0.007 < We_{in} < 0.033$), matching what was predicted by Abate et al. In the future, it will be necessary to measure the surface tension between the fibrin and Pico-surf solutions and test a wider range of flow rates to induce double emulsion formation in one-step. This would allow us to optimize the thickness of the oil shell to keep microgels disperse in media while also allowing transport of nutrients to cells that are encapsulated.

We have demonstrated the versatility of microgels by incorporating them into bulk hydrogels and by fabricating them using different materials (Figure 5.6). Integrating microgels into a different bulk material enables modification of microenvironments in a macroscale tissue model. The mechanical and chemical properties as well as the biological content encapsulated in microgels can be tuned to direct cell growth and behavior in a tissue [220]. Microgels can also be used to reca-

pitulate the heterogeneity found *in vivo*, not only for tumors, but organs as well by encapsulating different cell types in different biomaterials [190]. To utilize fibrin microgels for tissue engineering applications, it may be necessary to create a core-shell microgel with another material surrounding the fibrin, such as alginate or polyethylene glycol, to enable easier handling and elimination of oil [221].

Fibrin microgels may also be utilized to control cell degradation in tissue engineered models. We demonstrated that adding the enzyme tranglutaminase to fibrin, resulted in a decrease in cell degradation compared to fibrin without transglutaminase (Figure 5.9). Plasmin, a protease known to degrade fibrin [222] resulted in less degradation than the 4T1 cells, indicating the aggressiveness of the cells. Adding transglutaminase to fibrin altered microstructure (Figure 5.7) while retaining similar bulk mechanical properties (Figure 5.8). Impedance correlation spectroscopy (ICS) analysis found that fibrin with TG had larger structures whereas fibrin without TG had more structures, confirming the difference in microstructure (Table 5.2). However ICS is a very generalized quantification and other methods may be used to give insight into the mechanisms responsible for the differences in degradation. Microrheology can be performed to determine the mechanical properties of the microenvironment that the cells experience. Additionally, fluorescence recovery after photobleaching (FRAP) may be performed to characterize differences in transport phenomena in the two different formulations. If pore size in the two formulations is different, this may influence the transport of proteases that the cells are secreting, and therefore change degradation. TG itself may also influence the behavior of cells and warrants investigation. Assays that quantify proliferation and metabolic activity of cells may be helpful in determining TG's effect on cell behavior.

5.6 Conclusion

We have successfully encapsulated cancer and endothelial cells in fibrin microgels and have developed methods that will enable their use for long term cell culture and tissue engineering applications. The double emulsion fibrin microgels may enable testing of different concentrations

of drugs, calcium, or microenvironments in combination with electroporation while providing a 3D environment. Microgels may be used to test electroporation-based therapies at the single cell level while also enabling downstream genomic or transcriptomic analysis to evaluate cell response. The ability to control degradation of fibrin microgels by simply changing their microstructure may be a powerful tool that can be used to control cellular interactions in a tissue engineered model both spatially and temporally. Microgels may also help to preserve the integrity of tissue models when using highly aggressive cancer cells that tend to degrade extracellular matrix quickly such as the 4T1 cells. This technique may also allow creation of multi-material tissue models, therefore enabling *in vitro* and *ex-vivo* recapitulation of tumor heterogeneity found *in vivo*.

Chapter 6

Conclusion

6.1 Introduction

Cancer is a very complex disease that is heterogeneous in nature, making it challenging to develop successful treatments. The same challenges that serve as obstacles in treatment such as heterogeneity of cell types and extracellular matrix, gradients in growth factors and oxygen, and leaky vasculature, also serve as obstacles in developing physiologically relevant *in vitro* or *ex-vivo* tumor platforms. Therefore, the need to develop both superior cancer therapies that overcome limitations of standard treatments, and relevant models with which to test them, are interconnected.

Electroporation-based tumor therapies are an alternative to standard cancer treatments. Electroporation treatments such as electrochemotherapy (ECT) and irreversible electroporation (IRE) utilize pulsed electric fields to permeabilize cellular membranes, allowing otherwise impermeable ions and molecules to enter the cell, with the goal of either enhancing cancer drug delivery or inducing cancer cell death. While these therapies have shown promise in the clinic, they are limited in the size of tumors that they can treat without increasing the applied voltage, which results in increased thermal damage and muscle contractions. Therefore, a method is needed to safely enhance ablation size.

The goal of this dissertation was to address the coupled challenge of advancing electroporation-based therapies and developing a method to create better *in vitro* tumor models with which to test them. A simplified tumor platform was used to study the effect of adjuvant calcium on ablation size for IRE and high-frequency IRE (H-FIRE) treatments. Finite element analysis was used to correlate ablation area to the electric field threshold for different concentrations of calcium as well as different pulse parameters. The predicted increase in ablation volume for an *in vivo* treatment using IRE and adjuvant calcium was also simulated. Gene expression of cells treated using H-FIRE with and without calcium was analyzed to uncover the biological pathways responsible for cell death. Finally, fibrin microgels were created as a tool to incorporate different materials, cells, and microenvironments into *in vitro* and *ex-vivo* tumor models, with the goal of recapitulating the complexity and heterogeneity of tumors found *in vivo*.

6.2 Summary of results

In chapter 3, a simplified tumor platform was designed to study the enhanced susceptibility of glioblastoma cells to irreversible electroporation using a calcium adjuvant. Glioblastoma cells were cultured in a collagen scaffold and were treated with IRE. Fluorescent images of live and dead cells were used to quantify ablation area using a custom algorithm developed in MATLAB. Ablation areas were then used to determine the corresponding electric field threshold in a numerical model of electric field distribution. IRE in combination with adjuvant calcium (5mM $CaCl_2$) resulted in a nearly two-fold increase in ablation area *in vitro* compared to IRE alone. Adjuvant $CaCl_2$ induced death in cells reversibly electroporated by IRE, thereby lowering the electric field thresholds required for cell death to nearly half that of IRE alone. These findings, combined with our numerical modeling, suggested the ability to ablate up to 3.2X larger volumes of tissue *in vivo* when combining IRE and calcium.

Chapter 4 expands upon the results of chapter 3 by investigating the effect adjuvant calcium had on ablation size for H-FIRE treatment. Adjuvant calcium enhanced ablation area *in vitro* for H-FIRE

treatments of several pulse durations (1, 2, 5, 10 μs). Furthermore, H-FIRE treatment using 10 μs pulses delivered with 1 mM $CaCl_2$ resulted in cell death thresholds comparable to IRE thresholds without calcium. This finding may allow researchers to ablate areas similar in size to traditional IRE treatments, while eliminating some of the side effects associated with IRE such as conductivity changes and dependence on tissue geometry. Additionally, clinicians may be able to use commercially available generators instead of custom-made generators for treatment, simplifying translation to the clinic. Quantifying the reversible electroporation threshold revealed that $CaCl_2$ enhances the permeabilization of cells compared to a NaCl control. Gene expression analysis determined that $CaCl_2$ upregulates expression of *EIFB5* and 60S ribosomal subunit genes while downregulating *NOX1/4*, leading to increased signaling in pathways that may lead to necroptosis. The opposite was found for control treatment without $CaCl_2$ suggesting cells experience an increase in pro survival signaling.

In chapter 5, I developed a technology that may enable creation of physiologically relevant and complex *in-vitro* and *ex-vivo* tumor models using droplet microfluidics. Fibrin microgels were created using a microfluidic flow-focusing device. By varying the flow rate ratio between the fibrinogen/thrombin solution and the continuous oil phase, microgel diameter was tuned and ranged from 56 μm to 85 μm. Human cerebral microvascular endothelial cells (hCMEC/D3) were successfully encapsulated in fibrin microgels and approximately 80% survived up to 3 days. Microgels tended to clump in cell culture media, so a double emulsion device was used to create a thin shell of oil around the microgels to prevent this occurrence. Cells were successfully encapsulated in the double emulsions, however, cell encapsulation efficiency needs to be improved. Microgels were also fabricated using Matrigel and a blend of fibrin-alginate demonstrating their versatility. Microgels were also easily incorporated into bulk fibrin and bulk alginate, demonstrating their potential for creating tailored microenvironments in a larger tissue construct.

6.3 Future work

Calcium IRE treatments will need to be tested *in vivo* to confirm the results that were obtained here using *in vitro* studies. H-FIRE treatment using 10 μs pulses delivered with calcium resulted in cell death thresholds comparable to IRE thresholds without calcium, however elimination of muscle contractions during treatment need to be confirmed. Following our observation that sucrose and NaCl may prevent cell death, we envision injecting a buffer that contains sucrose and lacks calcium to control electroporation treatments *in vivo*, therefore preserving tissue that is outside of the desired ablation zone. Spatial control over ablations and sparing of blood vessels may be beneficial for treatments such as blood-brain barrier disruption.

One limitation of the simplified platform that was used to investigate IRE treatments with a calcium additive is that gene expression of cells that were exposed to a range of electric field magnitudes was analyzed. These cells may be experiencing differential gene expression that could be lost in a bulk sample. Microgels may provide a great platform that would enable exposing single cells to a range of electric field magnitudes found in the *in vitro* scaffold. Subsequently, single cell genomic and transcriptomic studies can be carried out to precisely characterize cell response for different electric field strengths. The collagen scaffold used to test the effects of using calcium in combination with IRE and H-FIRE treatment is an improvement upon previous methods used to test electroporation treatments that used cells in suspension or monolayer culture. However, the scaffold still lacks the heterogeneity that exists in cancer.

I envision using fibrin microgels to create 3D tissue constructs using bioprinting techniques. To our knowledge, no one has previously demonstrated the use of cell encapsulated microgels in bioprinting. I hypothesize that microgels may be used to protect cells from the shear forces required by direct ink write techniques. Cells with a range of known sensitivities to shear stress can be used to test this hypothesis along with materials with different shear thinning properties. This would enable bioprinting with cells that have been previously avoided due to concerns about viability.

Skylar-Scott et al., recently developed a technique to use embroid bodies and cardiac organoids

as a self-healing, porous bath to print sacrifical vasculature that can then be washed out after the organoids have been annealed together [223]. We envision using microgels in a similar fashion, however microgel diameter can be tuned more easily than the diameters of organoids. This enables tuning of the structure's pores which can be used to modulate transport throughout the tissue [187, 188]. Additionally, microgels are very monodisperse, ensuring uniformity of pore size whereas organoids and spheroids tend to be more polydisperse. Different cell types may be encapsulated in microgels of different biomaterials, therefore enabling the creation of a complex, heterogeneous tissue construct.

6.4 Conclusion

This dissertation tackled the complementary need to develop both superior cancer therapies that overcome limitations of standard treatments and tissue engineering technologies that can be utilized to create better *in vitro* tumor models. I have developed a method to enhance ablation size for electroporation-based tumor therapies using adjuvant calcium and began uncovering the signaling pathways responsible for cell death in calcium and no calcium conditions. Additionally, I developed a tissue engineering technique that can be used to create more complex and heterogeneous *in vitro* tumor models using micron scale hydrogels (microgels). I envision using these microgels to test different drug, calcium, and microenvironment conditions with electroporation therapies at the single cell level to further our knowledge about the cell death mechanisms induced by irreversible electroporation. In the future, microgels may also be used to advance the field of bioprinting, protecting cells from shear stress as well as enabling creation of perfusable 3D tissue constructs.

Bibliography

[1] Douglas Hanahan and Robert A Weinberg. The hallmarks of cancer, 1 2000.

[2] Charles Gawad, Winston Koh, and Stephen R. Quake. Dissecting the clonal origins of childhood acute lymphoblastic leukemia by single-cell genomics. Proceedings of the National Academy of Sciences of the United States of America, 111(50):17947–17952, 12 2014.

[3] Chang Yu, Jun Yu, Xiaotian Yao, William K.K. Wu, Youyong Lu, Senwei Tang, Xiangchun Li, Li Bao, Xiaoxing Li, Yong Hou, Renhua Wu, Min Jian, Ruoyan Chen, Fan Zhang, Lixia Xu, Fan Fan, Jun He, Qiaoyi Liang, Hongyi Wang, Xueda Hu, Minghui He, Xiang Zhang, Hancheng Zheng, Qibin Li, Hanjie Wu, Yan Chen, Xu Yang, Shida Zhu, Xun Xu, Huanming Yang, Jian Wang, Xiuqing Zhang, Joseph J.Y. Sung, Yingrui Li, and Jun Wang. Discovery of biclonal origin and a novel oncogene SLC12A5 in colon cancer by single-cell sequencing. Cell Research, 24(6):701–712, 2014.

[4] Marco Gerlinger, Andrew J. Rowan, Stuart Horswell, James Larkin, David Endesfelder, Eva Gronroos, Pierre Martinez, Nicholas Matthews, Aengus Stewart, Patrick Tarpey, Ignacio Varela, Benjamin Phillimore, Sharmin Begum, Neil Q. McDonald, Adam Butler, David Jones, Keiran Raine, Calli Latimer, Claudio R. Santos, Mahrokh Nohadani, Aron C. Eklund, Bradley Spencer-Dene, Graham Clark, Lisa Pickering, Gordon Stamp, Martin Gore, Zoltan Szallasi, Julian Downward, P. Andrew Futreal, and Charles Swanton. Intratumor Heterogeneity and Branched Evolution Revealed by Multiregion Sequencing. New England Journal of Medicine, 366(10):883–892, 3 2012.

[5] Nicholas McGranahan and Charles Swanton. Biological and therapeutic impact of intratu-

mor heterogeneity in cancer evolution, 2015.

[6] Jill W Ivey, Mohammad Bonakdar, Akanksha Kanitkar, Rafael V Davalos, and Scott S Verbridge. Improving cancer therapies by targeting the physical and chemical hallmarks of the tumor microenvironment, 2016.

[7] Charissa Kim, Ruli Gao, Emi Sei, Rachel Brandt, Johan Hartman, Thomas Hatschek, Nicola Crosetto, Theodoros Foukakis, and Nicholas E. Navin. Chemoresistance Evolution in Triple-Negative Breast Cancer Delineated by Single-Cell Sequencing. Cell, 173(4):879–893, 5 2018.

[8] Daniela F. Quail and Johanna A. Joyce. Microenvironmental regulation of tumor progression and metastasis, 11 2013.

[9] A Bergamaschi, E Tagliabue, T Sørlie, B Naume, T Triulzi, R Orlandi, H. G. Russnes, J. M. Nesland, R Tammi, P Auvinen, V. M. Kosma, S Ménard, and A. L. Børresen-Dale. Extracellular matrix signature identifies breast cancer subgroups with different clinical outcome. Journal of Pathology, 214(3):357–367, 2 2008.

[10] Jennifer M. Munson and Adrian C. Shieh. Interstitial fluid flow in cancer: Implications for disease progression and treatment, 8 2014.

[11] Kaitlin Graham and Evan Unger. Overcoming tumor hypoxia as a barrier to radiotherapy, chemotherapy and immunotherapy in cancer treatment, 2018.

[12] L. H. Gray, A. D. Conger, M. Ebert, S. Hornsey, and O. C. Scott. The concentration of oxygen dissolved in tissues at the time of irradiation as a factor in radiotherapy. The British journal of radiology, 26(312):638–648, 12 1953.

[13] Rakesh K. Jain. Determinants of Tumor Blood Flow: A Review. Cancer Research, 48(10):2641–2658, 1988.

[14] Rakesh K. Jain. Normalization of tumor vasculature: An emerging concept in antiangiogenic therapy, 1 2005.

[15] Einar K. Rofstad, Kanthi Galappathi, and Berit S. Mathiesen. Tumor Interstitial Fluid Pressure-A Link between Tumor Hypoxia, Microvascular Density, and Lymph Node Metas-

tasis. Neoplasia, 16(7):586–594, 2014.

[16] Ralf W. Glaser, Sergei L. Leikin, Leonid V. Chernomordik, Vasili F. Pastushenko, and Artjom I. Sokirko. Reversible electrical breakdown of lipid bilayers: formation and evolution of pores. BBA - Biomembranes, 940(2):275–287, 5 1988.

[17] I. G. Abidor, V. B. Arakelyan, L. V. Chernomordik, Yu A. Chizmadzhev, V. F. Pastushenko, and M. P. Tarasevich. Electric breakdown of bilayer lipid membranes. I. The main experimental facts and their qualitative discussion. Journal of Electroanalytical Chemistry, 104(C):37–52, 1 1979.

[18] Raphael C Lee, D J Canaday, and S M Hammer. Transient and stable ionic permeabilization of isolated skeletal muscle cells after electrical shock. Journal of Burn Care & Rehabilitation, 14(5):528–40, 1993.

[19] Kazuhiko Kinosita Jr and Tian Yow Tsong. Formation and resealing of pores of controlled sizes in human erythrocyte membrane. Nature, 268(2):438–441, 8 1977.

[20] Stella Somiari, Jill Glasspool-Malone, Joseph J. Drabick, Richard A. Gilbert, Richard Heller, Mark J. Jaroszeski, and Robert W. Malone. Theory and in Vivo Application of Electroporative Gene Delivery. Molecular Therapy, 2(3):178–187, 9 2000.

[21] L M Mir, M F Bureau, J Gehl, R Rangara, D Rouy, J M Caillaud, P Delaere, D Branellec, B Schwartz, and D Scherman. High-efficiency gene transfer into skeletal muscle mediated by electric pulses. Proceedings of the National Academy of Sciences of the United States of America, 96(8):4262–7, 4 1999.

[22] Mohammad Bonakdar, Elisa M. E.M. Wasson, Yong W. Y.W. Lee, and R.V. Rafael V. Davalos. Electroporation of Brain Endothelial Cells on Chip toward Permeabilizing the Blood-Brain Barrier. Biophysical Journal, 110(2):503–513, 2016.

[23] Anita Gothelf, Lluis M. Mir, and Julie Gehl. Electrochemotherapy: Results of cancer treatment using enhanced delivery of bleomycin by electroporation. Cancer Treatment Reviews, 29(5):371–387, 10 2003.

[24] Mark J Jaroszeski, Richard Gilbert, and Richard Heller. Electrochemotherapy: an emerg-

ing drug delivery method for the treatment of cancer. Advanced Drug Delivery Reviews, 26(2):185–197, 1997.

[25] Lluis M Mir and Stéphane Orlowski. Mechanisms of electrochemotherapy. Advanced Drug Delivery Reviews, 35(1):107–118, 1999.

[26] G. Sersa, D. Miklavcic, M. Cemazar, Z. Rudolf, G. Pucihar, and M. Snoj. Electrochemotherapy in treatment of tumours. European journal of surgical oncology : the journal of the European Society of Surgical Oncology and the British Association of Surgical Oncology, 34(2):232–40, 2 2008.

[27] Lluis M. Mir, Julie Gehl, Gregor Sersa, Christopher G. Collins, Jean Rémi Garbay, Valérie Billard, Poul F. Geertsen, Z. Rudolf, Gerald C. O'Sullivan, and Michel Marty. Standard operating procedures of the electrochemotherapy: Instructions for the use of bleomycin or cisplatin administered either systemically or locally and electric pulses delivered by the CliniporatorTM by means of invasive or non-invasive electrodes. European Journal of Cancer, Supplement, 4(11):14–25, 11 2006.

[28] Michel Marty, Gregor Sersa, Jean Rémi Garbay, Julie Gehl, Christopher G. Collins, Marko Snoj, Valérie Billard, Poul F. Geertsen, John O. Larkin, Damijan Miklavcic, Ivan Pavlovic, Snezna M. Paulin-Kosir, Maja Cemazar, Nassim Morsli, Declan M. Soden, Zvonimir Rudolf, Caroline Robert, and Gerald C. O'Sullivan. Electrochemotherapy – An easy, highly effective and safe treatment of cutaneous and subcutaneous metastases: Results of ESOPE (European Standard Operating Procedures of Electrochemotherapy) study. European Journal of Cancer Supplements, 4(11):3–13, 11 2006.

[29] Julie Gehl, Gregor Sersa, Louise Wichmann Matthiessen, Tobian Muir, Declan Soden, Antonio Occhini, Pietro Quaglino, Pietro Curatolo, Luca G. Campana, Christian Kunte, A. James P. Clover, Giulia Bertino, Victor Farricha, Joy Odili, Karin Dahlstrom, Marco Benazzo, and Lluis M. Mir. Updated standard operating procedures for electrochemotherapy of cutaneous tumours and skin metastases. Acta Oncologica, 57(7):874–882, 7 2018.

[30] Overview | Electrochemotherapy for metastases in the skin from tumours of non-skin origin

and melanoma | Guidance | NICE.

[31] Pietro Curatolo, Pietro Quaglino, Federica Marenco, Monica Mancini, Tiziana Nardò, Claudio Mortera, Roberta Rotunno, Stefano Calvieri, and Maria Grazia Bernengo. Electrochemotherapy in the Treatment of Kaposi Sarcoma Cutaneous Lesions: A Two-Center Prospective Phase II Trial. Annals of Surgical Oncology, 19(1):192–198, 1 2012.

[32] Alexander Stratigos, Claus Garbe, Celeste Lebbe, Josep Malvehy, Veronique del Marmol, Hubert Pehamberger, Ketty Peris, Jürgen C. Becker, Iris Zalaudek, Philippe Saiag, Mark R. Middleton, Lars Bastholt, Alessandro Testori, and Jean-Jacques Grob. Diagnosis and treatment of invasive squamous cell carcinoma of the skin: European consensus-based interdisciplinary guideline. European Journal of Cancer, 51(14):1989–2007, 9 2015.

[33] NICE. Electrochemotherapy for primary basal cell carcinoma and primary squamous cell carcinoma carcinoma. Technical report, National Institute for Health and Care Excellence, 2014.

[34] Luca G. Campana, Sara Valpione, Cristina Falci, Simone Mocellin, Michela Basso, Luigi Corti, Nicola Balestrieri, Alberto Marchet, and Carlo R. Rossi. The activity and safety of electrochemotherapy in persistent chest wall recurrence from breast cancer after mastectomy: a phase-II study. Breast Cancer Research and Treatment, 134(3):1169–1178, 8 2012.

[35] Birgit Agerholm-Larsen, Helle K. Iversen, Per Ibsen, Jakob M. Moller, Faisal Mahmood, Kurt Svarre Jensen, Julie Gehl, Kurt Svarre Jensen, and Julie Gehl. Preclinical validation of electrochemotherapy as an effective treatment for brain tumors. Cancer Research, 71(11):3753–3762, 6 2011.

[36] Mette Linnert, Birgit Agerholm-Larsen, Faisal Mahmood, Helle K Iversen, and Julie Gehl. Electrochemotherapy for primary and secondary brain tumors. In Tumors of the central nervous system., number 20, page In press. 2011.

[37] Mette Linnert, Birgit Agerholm-Larsen, Faisal Mahmood, Helle K. Iversen, and Julie Gehl. Treatment of Brain Tumors: Electrochemotherapy. pages 247–259. Springer Netherlands, 2014.

[38] Salvatore Tafuto, Claudia von Arx, Chiara De Divitiis, Claire Tracey Maura, Raffaele Palaia, Vittorio Albino, Roberta Fusco, Massimo Membrini, Antonella Petrillo, Vincenza Granata, and Francesco Izzo. Electrochemotherapy as a new approach on pancreatic cancer and on liver metastases. International Journal of Surgery, 21:S78–S82, 9 2015.

[39] Vincenza Granata, Roberta Fusco, Sergio Venanzio Setola, Mauro Piccirillo, Maddalena Leongito, Raffaele Palaia, Francesco Granata, Secondo Lastoria, Francesco Izzo, and Antonella Petrillo. Early radiological assessment of locally advanced pancreatic cancer treated with electrochemotherapy. World journal of gastroenterology, 23(26):4767–4778, 7 2017.

[40] Laura Coletti, Valentina Battaglia, Paolo De Simone, Laura Turturici, Carlo Bartolozzi, and Franco Filipponi. Safety and feasibility of electrochemotherapy in patients with unresectable colorectal liver metastases: A pilot study. International Journal of Surgery, 44:26–32, 8 2017.

[41] Stine Krog Frandsen, Hanne Gissel, Pernille Hojman, Trine Tramm, Jens Eriksen, and Julie Gehl. Direct therapeutic applications of calcium electroporation to effectively induce tumor necrosis. Cancer research, 72(6):1336–41, 3 2012.

[42] Stine Krog Frandsen, Hanne Gissel, Pernille Hojman, Jens Eriksen, and Julie Gehl. Calcium electroporation in three cell lines: A comparison of bleomycin and calcium, calcium compounds, and pulsing conditions. Biochimica et Biophysica Acta - General Subjects, 1840(3):1204–1208, 2014.

[43] Emilie Louise Hansen, Esin Bengisu Sozer, Stefania Romeo, Stine Krog Frandsen, P. Thomas Vernier, and Julie Gehl. Dose-Dependent ATP Depletion and Cancer Cell Death following Calcium Electroporation, Relative Effect of Calcium Concentration and Electric Field Strength. PLOS ONE, 10(4):e0122973, 4 2015.

[44] H. Falk, L.W. Matthiessen, G. Wooler, and J. Gehl. Calcium electroporation for treatment of cutaneous metastases; a randomized double-blinded phase II study, comparing the effect of calcium electroporation with electrochemotherapy. Acta Oncologica, pages 1–9, 8 2017.

[45] R. V. Davalos, L. M. Mir, and B. Rubinsky. Tissue Ablation with Irreversible Electropora-

tion. Annals of Biomedical Engineering, 33(2):223–231, 2 2005.

[46] Bassim Al-Sakere, Franck André, Claire Bernat, Elisabeth Connault, Paule Opolon, Rafael V. Davalos, Boris Rubinsky, and Lluis M. Mir. Tumor ablation with irreversible electroporation. PLoS ONE, 2(11):1–8, 11 2007.

[47] Gary Onik, Paul Mikus, and Boris Rubinsky. Irreversible Electroporation: Implications for Prostate Ablation. Technology in Cancer Research & Treatment, 6(4):295–300, 8 2007.

[48] Rafael V. Davalos and Boris Rubinsky. Temperature considerations during irreversible electroporation. International Journal of Heat and Mass Transfer, 51(23-24):5617–5622, 11 2008.

[49] Rafael V. Davalos, Boris Rubinsky, and Lluis M. Mir. Theoretical analysis of the thermal effects during in vivo tissue electroporation. Bioelectrochemistry, 61(1-2):99–107, 10 2003.

[50] Paulo A Garcia, John H Rossmeisl, Robert E Neal, Thomas L Ellis, and Rafael V Davalos. A parametric study delineating irreversible electroporation from thermal damage based on a minimally invasive intracranial procedure. Biomedical engineering online, 10(1):34, 2011.

[51] Christopher B. Arena, Christopher S. Szot, Paulo A. Garcia, Marissa Nichole Rylander, and Rafael V. Davalos. A three-dimensional in vitro tumor platform for modeling therapeutic irreversible electroporation. Biophysical Journal, 103(9):2033–2042, 2012.

[52] Jon F J.F. Edd, Liana Horowitz, R.V. Rafael V Davalos, Lluis M L.M. Mir, and Boris Rubinsky. In Vivo Results of a New Focal Tissue Ablation Technique: Irreversible Electroporation. IEEE Transactions on Biomedical Engineering, 53(7):1409–1415, 7 2006.

[53] John H. Rossmeisl, Paulo A. Garcia, John L. Roberston, Thomas L. Ellis, and Rafael V. Davalos. Pathology of non-thermal irreversible electroporation (N-TIRE)-induced ablation of the canine brain. Journal of Veterinary Science, 14(4):433–440, 2013.

[54] Elad Maor, Antoni Ivorra, Jonathan Leor, and Boris Rubinsky. The Effect of Irreversible Electroporation on Blood Vessels. Technology in Cancer Research & Treatment, 6(4):307–312, 8 2007.

[55] Wei Li, Qingyu Fan, Zhenwei Ji, Xiuchun Qiu, and Zhao Li. The Effects of Irreversible

Electroporation (IRE) on Nerves. PLoS ONE, 6(4):e18831, 4 2011.

[56] Robert C G Martin, Kelli McFarland, Susan Ellis, and Vic Velanovich. Irreversible electroporation therapy in the management of locally advanced pancreatic adenocarcinoma. Journal of the American College of Surgeons, 215(3):361–369, 2012.

[57] Salvatore Paiella, Giovanni Butturini, Isabella Frigerio, Roberto Salvia, Giulia Armatura, Matilde Bacchion, Martina Fontana, Mirko D"Onofrio, Enrico Martone, and Claudio Bassi. Safety and Feasibility of Irreversible Electroporation (IRE) in Patients with Locally Advanced Pancreatic Cancer: Results of a Prospective Study. Digestive Surgery, 32(2):90–97, 2015.

[58] Robert C. G. Martin, David Kwon, Sricharan Chalikonda, Marty Sellers, Eric Kotz, Charles Scoggins, Kelly M. McMasters, and Kevin Watkins. Treatment of 200 Locally Advanced (Stage III) Pancreatic Adenocarcinoma Patients With Irreversible Electroporation. Annals of Surgery, 262(3):486–494, 9 2015.

[59] Hester J. Scheffer, Laurien G. P. H. Vroomen, Marcus C. de Jong, Marleen C. A. M. Melenhorst, Babs M. Zonderhuis, Freek Daams, Jantien A. Vogel, Marc G. H. Besselink, Cornelis van Kuijk, Jill Witvliet, Marian A. E. de van der Schueren, Tanja D. de Gruijl, Anita G. M. Stam, Petrousjka M. P. van den Tol, Foke van Delft, Geert Kazemier, and Martijn R. Meijerink. Ablation of Locally Advanced Pancreatic Cancer with Percutaneous Irreversible Electroporation: Results of the Phase I/II PANFIRE Study. Radiology, 282(2):585–597, 2 2017.

[60] Kenneth R. Thomson, Wa Cheung, Samantha J. Ellis, Dean Federman, Helen Kavnoudias, Deirdre Loader-Oliver, Stuart Roberts, Peter Evans, Christine Ball, and Andrew Haydon. Investigation of the Safety of Irreversible Electroporation in Humans. Journal of Vascular and Interventional Radiology, 22(5):611–621, 5 2011.

[61] Jun Zhao, Xiaofei Wen, Li Tian, Tingting Li, Chunyu Xu, Xiaoxia Wen, Marites P. Melancon, Sanjay Gupta, Baozhong Shen, Weiyi Peng, and Chun Li. Irreversible electroporation reverses resistance to immune checkpoint blockade in pancreatic cancer. Nature

Communications, 10(1), 12 2019.

[62] Christine Ball, Kenneth R Thomson, and Helen Kavnoudias. Irreversible electroporation: a new challenge in "out of operating theater" anesthesia. Anesthesia and analgesia, 110(5):1305–9, 5 2010.

[63] John H. Rossmeisl, Paulo A. Garcia, Theresa E. Pancotto, John L. Robertson, Natalia Henao-Guerrero, Robert E. Neal, Thomas L. Ellis, and Rafael V. Davalos. Safety and feasibility of the NanoKnife system for irreversible electroporation ablative treatment of canine spontaneous intracranial gliomas. Journal of Neurosurgery, 123(4):1008–1025, 10 2015.

[64] Christopher B Arena, Michael B Sano, John H Rossmeisl, John L Caldwell, Paulo a Garcia, Marissa Nichole Rylander, and Rafael V Davalos. High-frequency irreversible electroporation (H-FIRE) for non-thermal ablation without muscle contraction. Biomedical engineering online, 10(1):102, 1 2011.

[65] Jill W. Ivey, Eduardo L. Latouche, Michael B. Sano, John H. Rossmeisl, Rafael V. Davalos, and Scott S. Verbridge. Targeted cellular ablation based on the morphology of malignant cells. Scientific Reports, 5:17157, 2015.

[66] Jill W Ivey, Scott S Verbridge, Rafael V Davalos, John H Rossmeisl, Yong Woo Lee, and Zhi Sheng. INVESTIGATING THE APPLICATIONS OF ELECTROPORATION THERAPY FOR TARGETED TREATMENT OF GLIOBLASTOMA MULTIFORME BASED ON MALIGNANT PROPERTIES OF CELLS. 2017.

[67] Veronica M. Ringel-Scaia, Natalie Beitel-White, Melvin F. Lorenzo, Rebecca M. Brock, Kathleen E. Huie, Sheryl Coutermarsh-Ott, Kristin Eden, Dylan K. McDaniel, Scott S. Verbridge, John H. Rossmeisl, Kenneth J. Oestreich, Rafael V. Davalos, and Irving C. Allen. High-frequency irreversible electroporation is an effective tumor ablation strategy that induces immunologic cell death and promotes systemic anti-tumor immunity. EBioMedicine, 44:112–125, 6 2019.

[68] Suyashree P Bhonsle, Christopher B Arena, Daniel C Sweeney, and Rafael V Davalos. Mitigation of impedance changes due to electroporation therapy using bursts of high-frequency

bipolar pulses. Biomedical engineering online, 14 Suppl 3(Suppl 3):S3, 8 2015.

[69] Suyashree Bhonsle, Melvin Lorenzo, Ahmad Safaai-Jazi, and Rafael V. Davalos. Characterization of Nonlinearity and Dispersion in Tissue Impedance during High Frequency Electroporation, 2017.

[70] Christopher B Arena, Michael B Sano, Marissa Nichole Rylander, and Rafael V Davalos. Theoretical considerations of tissue electroporation with high-frequency bipolar pulses. IEEE transactions on bio-medical engineering, 58(5):1474–82, 5 2011.

[71] Michael B. Sano, Christopher B. Arena, Matthew R. DeWitt, Dieter Saur, and Rafael V. Davalos. In-vitro bipolar nano- and microsecond electro-pulse bursts for irreversible electroporation therapies. Bioelectrochemistry, 100:69–79, 12 2014.

[72] Daniel C. Sweeney, Matej Reberšek, Janja Dermol, Lea Rems, Damijan Miklavčič, and Rafael V. Davalos. Quantification of cell membrane permeability induced by monopolar and high-frequency bipolar bursts of electrical pulses. Biochimica et Biophysica Acta - Biomembranes, 1858(11):2689–2698, 11 2016.

[73] Richard Nuccitelli, Uwe Pliquett, Xinhua Chen, Wentia Ford, R James Swanson, Stephen J Beebe, Juergen F Kolb, and Karl H Schoenbach. Nanosecond pulsed electric fields cause melanomas to self-destruct. Biochemical and biophysical research communications, 343(2):351–60, 5 2006.

[74] Xinhua Chen, Juergen F. Kolb, R. James Swanson, Karl H. Schoenbach, and Stephen J. Beebe. Apoptosis initiation and angiogenesis inhibition: melanoma targets for nanosecond pulsed electric fields. Pigment Cell & Melanoma Research, 23(4):554–563, 8 2010.

[75] Edward B. Garon, David Sawcer, P. Thomas Vernier, Tao Tang, Yinghua Sun, Laura Marcu, Martin A. Gundersen, and H. Phillip Koeffler. In vitro andin vivo evaluation and a case report of intense nanosecond pulsed electric field as a local therapy for human malignancies. International Journal of Cancer, 121(3):675–682, 8 2007.

[76] Tadej Kotnik, Damijan Miklavcic, and Damijan Miklavčič. Theoretical evaluation of voltage inducement on internal membranes of biological cells exposed to electric fields. Biophysical

journal, 90(2):480–491, 1 2006.

[77] Wentia E. Ford, Wei Ren, Peter F. Blackmore, Karl H. Schoenbach, and Stephen J. Beebe. Nanosecond pulsed electric fields stimulate apoptosis without release of pro-apoptotic factors from mitochondria in B16f10 melanoma. Archives of Biochemistry and Biophysics, 497(1-2):82–89, 5 2010.

[78] Emily H. Hall, Karl H. Schoenbach, and Stephen J. Beebe. Nanosecond pulsed electric fields induce apoptosis in p53-wildtype and p53-null HCT116 colon carcinoma cells. Apoptosis, 12(9):1721–1731, 7 2007.

[79] P.Thomas Vernier, Yinghua Sun, Laura Marcu, Sarah Salemi, Cheryl M Craft, and Martin A Gundersen. Calcium bursts induced by nanosecond electric pulses. Biochemical and Biophysical Research Communications, 310(2):286–295, 10 2003.

[80] P Thomas Vernier, Yinghua Sun, Meng-Tse Chen, Martin A Gundersen, and Gale L Craviso. Nanosecond electric pulse-induced calcium entry into chromaffin cells. 2008.

[81] Richard Nuccitelli, Ryan Wood, Mark Kreis, Brian Athos, Joanne Huynh, Kaying Lui, Pamela Nuccitelli, and Ervin H. Epstein. First-in-human trial of nanoelectroablation therapy for basal cell carcinoma: Proof of method, 2 2014.

[82] Keiko Morotomi-Yano, Hidenori Akiyama, and Ken-ichi Yano. Different involvement of extracellular calcium in two modes of cell death induced by nanosecond pulsed electric fields. Archives of Biochemistry and Biophysics, 555-556:47–54, 8 2014.

[83] J Piñero, M López-Baena, T Ortiz, and F Cortés. Apoptotic and necrotic cell death are both induced by electroporation in HL60 human promyeloid leukaemia cells. Apoptosis : an international journal on programmed cell death, 2(3):330–6, 1997.

[84] Olga N. Pakhomova, Betsy W. Gregory, Iurii Semenov, and Andrei G. Pakhomov. Two Modes of Cell Death Caused by Exposure to Nanosecond Pulsed Electric Field. PLoS ONE, 8(7):e70278, 7 2013.

[85] Lorenzo Galluzzi and Ilio Vitale. Molecular mechanisms of cell death: recommendations of the Nomenclature Committee on Cell Death 2018. Cell death and differentiation, 25(3):486–

541, 3 2018.

[86] P. Marszalek, D.S. Liu, and T.Y. Tsong. Schwan equation and transmembrane potential induced by alternating electric field. Biophysical Journal, 58(4):1053–1058, 10 1990.

[87] Tadej Kotnik, Damijan Miklavcic, and T. Slivnik. Time course of transmembrane voltage induced by time - varying electric fields - a method for theoretical analysis and its applcation. Bioelectrochemistry and Bioenergetics, 45:3–16, 1998.

[88] T Kotnik and D Miklavcic. Analytical description of transmembrane voltage induced by electric fields on spheroidal cells. Biophysical journal, 79(2):670–9, 8 2000.

[89] Gorazd Pucihar, Damijan Miklavcic, and Tadej Kotnik. A time-dependent numerical model of transmembrane voltage inducement and electroporation of irregularly shaped cells. IEEE transactions on bio-medical engineering, 56(5):1491–501, 5 2009.

[90] Tomo Murovec, Daniel C. Sweeney, Eduardo Latouche, Rafael V. Davalos, and Christian Brosseau. Modeling of Transmembrane Potential in Realistic Multicellular Structures before Electroporation. 111(10):2286–2295, 11 2016.

[91] Zachary A. Levine and P. Thomas Vernier. Calcium and Phosphatidylserine Inhibit Lipid Electropore Formation and Reduce Pore Lifetime. The Journal of Membrane Biology, 245(10):599–610, 10 2012.

[92] Andraž Polak, Daniel Bonhenry, François Dehez, Peter Kramar, Damijan Miklavčič, and Mounir Tarek. On the Electroporation Thresholds of Lipid Bilayers: Molecular Dynamics Simulation Investigations. The Journal of Membrane Biology, 246(11):843–850, 11 2013.

[93] Tadej Kotnik, Feda Bobanović, Damijian Miklavc̆ic̆, and Damijan Miklavčič. Sensitivity of transmembrane voltage induced by applied electric fields - A theoretical analysis. Bioelectrochemistry and Bioenergetics, 43(2):285–291, 8 1997.

[94] J Teissié and M P Rols. An experimental evaluation of the critical potential difference inducing cell membrane electropermeabilization. Biophysical journal, 65(1):409–13, 7 1993.

[95] J Gimsa and D Wachner. Analytical description of the transmembrane voltage induced on arbitrarily oriented ellipsoidal and cylindrical cells. Biophysical journal, 81(4):1888–96, 10

2001.

[96] G. Pucihar, T. Kotnik, B. Valič, and D. Miklavčič. Numerical determination of transmembrane voltage induced on irregularly shaped cells. Annals of Biomedical Engineering, 34(4):642–652, 4 2006.

[97] Blaz Valic, Muriel Golzio, Mojca Pavlin, Anne Schatz, Cecile Faurie, Bruno Gabriel, J Teissie, M P Rols, and Damijan Miklavcic. Effect of electric field induced transmembrane potential on spheroidal cells: theory and experiment. Eur Biophys J, 32(6):519–528, 10 2003.

[98] John C. Neu and Wanda Krassowska. Asymptotic model of electroporation. Physical Review E - Statistical Physics, Plasmas, Fluids, and Related Interdisciplinary Topics, 59(3):3471–3482, 3 1999.

[99] K a DeBruin and W Krassowska. Modeling electroporation in a single cell. I. Effects Of field strength and rest potential. Biophysical journal, 77(3):1213–24, 9 1999.

[100] Lucie Delemotte and Mounir Tarek. Molecular Dynamics Simulations of Lipid Membrane Electroporation. The Journal of Membrane Biology, 245(9):531–543, 9 2012.

[101] Kiril Hristov, Uma Mangalanathan, Maura Casciola, Olga N. Pakhomova, and Andrei G. Pakhomov. Expression of voltage-gated calcium channels augments cell susceptibility to membrane disruption by nanosecond pulsed electric field. Biochimica et Biophysica Acta - Biomembranes, 1860(11):2175–2183, 11 2018.

[102] Robert E. Neal, Paulo A. Garcia, John L. Robertson, Rafael V. Davalos, Robert E II, Neal, Paulo a. Garcia, John L. Robertson, Rafael V. Davalos, Robert E. Neal, Paulo a. Garcia, John L. Robertson, and Rafael V. Davalos. Experimental characterization and numerical modeling of tissue electrical conductivity during pulsed electric fields for irreversible electroporation treatment planning. IEEE transactions on bio-medical engineering, 59(4):1076–85, 4 2012.

[103] D Sel, D Cukjati, D Batiuskaite, T Slivnik, L Mir, and D Miklavcic. Sequential finite element model of tissue electropermeabilisation. Conference proceedings : ... Annual

International Conference of the IEEE Engineering in Medicine and Biology Society. IEEE Engineering in Medicine and Biology Society. Conference, 5(5):3551–3554, 2004.

[104] Nataša Pavšelj, Zvonko Bregar, David Cukjati, Danute Batiuskaite, Lluis M. L.M. Mir, Damijan Miklavčič, N. Pavselj, Zvonko Bregar, David Cukjati, Danute Batiuskaite, Lluis M. L.M. Mir, and D. Miklavcic. The course of tissue permeabilization studied on a mathematical model of a subcutaneous tumor in small animals. IEEE Transactions on Biomedical Engineering, 52(8):1373–1381, 8 2005.

[105] Antoni Ivorra, Bassim Al-Sakere, Boris Rubinsky, and Lluis M Mir. In vivo electrical conductivity measurements during and after tumor electroporation: conductivity changes reflect the treatment outcome. Physics in medicine and biology, 54(19):5949–63, 10 2009.

[106] F.A. Duck. Physical Properties of Tissue: A Comprehensive Reference Book. Press, Academic, London, 1990.

[107] Damijan Miklavčič, Dejan Šemrov, Halima Mekid, and Lluis M Mir. A validated model of in vivo electric field distribution in tissues for electrochemotherapy and for DNA electrotransfer for gene therapy. Biochimica et biophysica acta, 1523(1):73–83, 2000.

[108] Mette Linnert and Julie Gehl. Bleomycin treatment of brain tumors: an evaluation. Anti-cancer drugs, 20(3):157–164, 3 2009.

[109] Theodore L. Bergman, Adrienne S. Lavine, Frank P. Incropera, and David P. Dewitt. Fundamentals of Heat and Mass Transfer. 7th Edition. 2011.

[110] Won Hee Lee, Zhi De Deng, Andrew F. Laine, Sarah H. Lisanby, and Angel V. Peterchev. Influence of white matter conductivity anisotropy on electric field strength induced by electroconvulsive therapy. In Proceedings of the Annual International Conference of the IEEE Engineering in Medicine and Biology Society, EMBS, pages 5473–5476. IEEE, 8 2011.

[111] Yajun Zhao, Suyashree Bhonsle, Shoulong Dong, Yanpeng Lv, Hongmei Liu, Ahmad Safaai-Jazi, Rafael V. Davalos, and Chenguo Yao. Characterization of conductivity changes during high-frequency irreversible electroporation for treatment planning. IEEE Transactions on Biomedical Engineering, 65(8):1810–1819, 2018.

[112] L. A. Stewart. Chemotherapy in adult high-grade glioma: A systematic review and meta-analysis of individual patient data from 12 randomised trials. Lancet, 359(9311):1011–1018, 2002.

[113] Roger Stupp, Warren Mason, Martin J. van den Bent, Michael Weller, Barbara M Fisher, Martin J.B. Taphoorn, Karl Belanger, Alba A. Brandes, Christine Marosi, Ulrich Bogdahn, Jürgen Curschmann, Robert C. Janzer, Samuel K. Ludwin, Thierry Gorlia, Anouk Allgeier, Denis Lacombe, Gregory Cairncross, Elizabeth Eisenhauer, and René O. Mirimanoff. Radiotherapy plus Concomitant and Adjuvant Temozolomide for Glioblastoma. The New England Journal of Medicine, 352(10):987–96, 3 2005.

[114] P A Garcia, T Pancotto, J H Rossmeisl, N Henao-Guerrero, N R Gustafson, G B Daniel, J L Robertson, T L Ellis, and R V Davalos. Non-thermal irreversible electroporation (N-TIRE) and adjuvant fractionated radiotherapeutic multimodal therapy for intracranial malignant glioma in a canine patient. Technology in cancer research & treatment, 10(1):73–83, 2011.

[115] Paulo A. Garcia, John H. Rossmeisl, Robert E. Neal, Thomas L. Ellis, John D. Olson, Natalia Henao-Guerrero, John Robertson, and Rafael V. Davalos. Intracranial nonthermal irreversible electroporation: In vivo analysis. Journal of Membrane Biology, 236(1):127–136, 7 2010.

[116] B. Rubinsky. Irreversible Electroporation in Medicine. Technology in Cancer Research & Treatment, 6(4):255–259, 8 2007.

[117] Christopher Brian Arena, John H Rossmeisl, John L Robertson, and Paulo A Garcia. Advancements in Irreversible Electroporation for the Treatment of Cancer. 2012.

[118] L.G. Salford, B.R.R. Persson, A. Brun, C.P. Ceberg, P.C. Kongstad, and L.M. Mir. A New Brain Tumor Therapy Combining Bleomycin with in Vivo Electropermeabilization. Biochemical and Biophysical Research Communications, 194(2):938–943, 7 1993.

[119] J. Gehl. Electroporation: theory and methods, perspectives for drug delivery, gene therapy and research. Acta physiologica Scandinavica, 177(4):437–47, 4 2003.

[120] D L Bhatt, D C Gaylor, and R C Lee. Rhabdomyolysis due to pulsed electric fields. Plastic

and reconstructive surgery, 86(1):1–11, 7 1990.

[121] R. E. Neal, J. H. Rossmeisl, V. D'Alfonso, J. L. Robertson, P. a. Garcia, S. Elankumaran, and R. V. Davalos. In vitro and numerical support for combinatorial irreversible electroporation and electrochemotherapy glioma treatment. Annals of Biomedical Engineering, 42(3):475–487, 2014.

[122] Claudia Fischbach, Ruth Chen, Takuya Matsumoto, Tobias Schmelzle, Joan S Brugge, Peter J Polverini, and David J Mooney. Engineering tumors with 3D scaffolds. Nature Methods, 4(10):855–860, 10 2007.

[123] Valerie L. Cross, Ying Zheng, Nak Won Choi, Scott S. Verbridge, Bryan A. Sutermaster, Lawrence J. Bonassar, Claudia Fischbach, and Abraham D. Stroock. Dense type I collagen matrices that support cellular remodeling and microfabrication for studies of tumor angiogenesis and vasculogenesis in vitro. Biomaterials, 31(33):8596–8607, 2010.

[124] Johanna Chiche, M Christiane Brahimi-Horn, and Jacques Pouysségur. Tumour hypoxia induces a metabolic shift causing acidosis: a common feature in cancer. Journal of cellular and molecular medicine, 14(4):771–94, 4 2010.

[125] Leo E. Gerweck and Kala Seetharaman. Cellular pH Gradient in Tumor versus Normal Tissue: Potential Exploitation for the Treatment of Cancer. Cancer Research, 56(6), 1996.

[126] A B Hjelmeland, Q Wu, J M Heddleston, G S Choudhary, J MacSwords, J D Lathia, R McLendon, D Lindner, A Sloan, and J N Rich. Acidic stress promotes a glioma stem cell phenotype. Cell Death and Differentiation, 18(5):829–840, 5 2011.

[127] Martin Bier, Stephanie M. Hammer, Daniel J. Canaday, and Raphael C. Lee. Kinetics of sealing for transient electropores in isolated mammalian skeletal muscle cells. Bioelectromagnetics, 20(3):194–201, 1999.

[128] Igor Lacković, Ratko Magjarević, and Damijan Miklavćić. Three-dimensional finite-element analysis of joule heating in electrochemotherapy and in vivo gene electrotransfer. IEEE Transactions on Dielectrics and Electrical Insulation, 16(5):1338–1347, 2009.

[129] Hanne Gissel and Torben Clausen. Ca2+ uptake and cellular integrity in rat EDL muscle

exposed to electrostimulation, electroporation, or A23187. American Journal of Physiology - Regulatory, Integrative and Comparative Physiology, 285(1), 2003.

[130] Gorazd Pucihar, Tadej Kotnik, Maša Kandušer, and Damijan Miklavčič. The influence of medium conductivity on electropermeabilization and survival of cells in vitro. Bioelectrochemistry, 54(2):107–115, 2001.

[131] Thomas L Ellis, Paulo A Garcia, John H Rossmeisl, Natalia Henao-Guerrero, John Robertson, and Rafael V Davalos. Nonthermal irreversible electroporation for intracranial surgical applications. Laboratory investigation. Journal of neurosurgery, 114(3):681–688, 2011.

[132] Xuejin Li, Aleksander S Popel, and George Em Karniadakis. Bloodplasma separation in Y-shaped bifurcating microfluidic channels: A dissipative particle dynamics simulation study. Physical Biology, 9(2):026010, 4 2012.

[133] Robert E Neal, John H Rossmeisl, Paulo A Garcia, Otto I Lanz, Natalia Henao-Guerrero, and Rafael V Davalos. Successful treatment of a large soft tissue sarcoma with irreversible electroporation. Journal of clinical oncology : official journal of the American Society of Clinical Oncology, 29(13):372–7, 5 2011.

[134] Helmut Schoellnast, Sebastien Monette, Paula C. Ezell, Ajita Deodhar, Majid Maybody, Joseph P. Erinjeri, Michael D. Stubblefield, Gordon W. Single, William C. Hamilton, and Stephen B. Solomon. Acute and Subacute Effects of Irreversible Electroporation on Nerves: Experimental Study in a Pig Model. Radiology, 260(2):421–427, 8 2011.

[135] Katsutoshi Sugimoto, Fuminori Moriyasu, Yoshiyuki Kobayashi, Kazuhiro Saito, Hirohito Takeuchi, Saori Ogawa, Mayumi Ando, Takatomo Sano, Toshifumi Mori, Yoshihiro Furuichi, and Ikuo Nakamura. Irreversible electroporation for nonthermal tumor ablation in patients with hepatocellular carcinoma: initial clinical experience in Japan. Japanese Journal of Radiology, 33(7):424–432, 7 2015.

[136] Keiichiro Suzuki, Yuji Tsunekawa, Reyna Hernandez-Benitez, Jun Wu, Jie Zhu, Euiseok J. Kim, Fumiyuki Hatanaka, Mako Yamamoto, Toshikazu Araoka, Zhe Li, Masakazu Kurita, Tomoaki Hishida, Mo Li, Emi Aizawa, Shicheng Guo, Song Chen, April Goebl,

Rupa Devi Soligalla, Jing Qu, Tingshuai Jiang, Xin Fu, Maryam Jafari, Concepcion Rodriguez Esteban, W. Travis Berggren, Jeronimo Lajara, Estrella Nuñez-Delicado, Pedro Guillen, Josep M. Campistol, Fumio Matsuzaki, Guang-Hui Liu, Pierre Magistretti, Kun Zhang, Edward M. Callaway, Kang Zhang, and Juan Carlos Izpisua Belmonte. In vivo genome editing via CRISPR/Cas9 mediated homology-independent targeted integration. Nature, 540(7631):144–149, 12 2016.

[137] W. J. Dower, J. F. Miller, and C. W. Ragsdale. High efficiency transformation of E.coli by high voltage electroporation. Nucleic Acids Research, 16(13):6127–6145, 7 1988.

[138] Gregor Sersa, Justin Teissie, Maja Cemazar, Emanuela Signori, Urska Kamensek, Guillermo Marshall, and Damijan Miklavcic. Electrochemotherapy of tumors as in situ vaccination boosted by immunogene electrotransfer. Cancer Immunology, Immunotherapy, 64:1315–1327, 2015.

[139] Mojca Pavlin, Natasa Pavselj, and Damijan Miklavcic. Dependence of induced transmembrane potential on cell density, arrangement, and cell position inside a cell system. IEEE transactions on bio-medical engineering, 49(6):605–12, 6 2002.

[140] Stine K Frandsen, Mie B Krüger, Uma M Mangalanathan, Trine Tramm, Faisal Mahmood, Ivana Novak, and Julie Gehl. Normal and malignant cells exhibit differential responses to calcium electroporation. Cancer Research, 77(16):4389–4401, 8 2017.

[141] E.M. Wasson, J.W. Ivey, S.S. Verbridge, and R.V. Davalos. The Feasibility of Enhancing Susceptibility of Glioblastoma Cells to IRE Using a Calcium Adjuvant. Annals of Biomedical Engineering, 45(11):2535–2547, 11 2017.

[142] Kamran C. Melikov, Vadim A. Frolov, Arseniy Shcherbakov, Andrey V. Samsonov, Yury A. Chizmadzhev, and Leonid V. Chernomordik. Voltage-Induced Nonconductive Pre-Pores and Metastable Single Pores in Unmodified Planar Lipid Bilayer. Biophysical Journal, 80(4):1829–1836, 4 2001.

[143] Stanisława Koronkiewicz, Sławomir Kalinowski, and Krzysztof Bryl. Programmable chronopotentiometry as a tool for the study of electroporation and resealing of pores

in bilayer lipid membranes. Biochimica et Biophysica Acta (BBA) - Biomembranes, 1561(2):222–229, 4 2002.

[144] Jaromir Stancl, Jan Skocilas, Ales Landfeld, Rudolf Zitny, and Milan Houska. Electrical and thermodynamic properties of a collagen solution. Acta Polytechnica, 57(3):229–234, 6 2017.

[145] G. H. Bardelmeyer. Electrical conduction in hydrated collagen. I. Conductivity mechanisms. Biopolymers, 12(10):2289–2302, 10 1973.

[146] Paulo A. Garcia, John H. Rossmeisl, John L. Robertson, John D. Olson, Annette J. Johnson, Thomas L. Ellis, and Rafael V. Davalos. 7.0-T Magnetic Resonance Imaging Characterization of Acute Blood-Brain-Barrier Disruption Achieved with Intracranial Irreversible Electroporation. PLoS ONE, 7(11):1–8, 11 2012.

[147] Kristin Eden, Daniel E Rothschild, Dylan K McDaniel, Bettina Heid, and Irving C Allen. Noncanonical NF-κB signaling and the essential kinase NIK modulate crucial features associated with eosinophilic esophagitis pathogenesis. Disease models & mechanisms, 10(12):1517–1527, 12 2017.

[148] Michelle H Theus, Thomas Brickler, Armand L Meza, Sheryl Coutermarsh-Ott, Amanda Hazy, Denis Gris, and Irving C Allen. Loss of NLRX1 Exacerbates Neural Tissue Damage and NF-κB Signaling following Brain Injury. Journal of immunology (Baltimore, Md. : 1950), 199(10):3547–3558, 11 2017.

[149] Irving C. Allen, Chris B. Moore, Monika Schneider, Yu Lei, Beckley K. Davis, Margaret A. Scull, Denis Gris, Kelly E. Roney, Albert G. Zimmermann, John B. Bowzard, Priya Ranjan, Kathryn M. Monroe, Raymond J. Pickles, Suryaprakash Sambhara, and Jenny P.Y. Ting. NLRX1 Protein Attenuates Inflammatory Responses to Infection by Interfering with the RIG-I-MAVS and TRAF6-NF-κB Signaling Pathways. Immunity, 34(6):854–865, 6 2011.

[150] James C Weaver, Kyle C Smith, Axel T Esser, Reuben S Son, and T R Gowrishankar. A brief overview of electroporation pulse strength-duration space: a region where additional intracellular effects are expected. Bioelectrochemistry (Amsterdam, Netherlands), 87:236–

43, 10 2012.

[151] Bennett L Ibey, Jody C Ullery, Olga N Pakhomova, Caleb C Roth, Iurii Semenov, Hope T Beier, Melissa Tarango, Shu Xiao, Karl H Schoenbach, and Andrei G Pakhomov. Bipolar nanosecond electric pulses are less efficient at electropermeabilization and killing cells than monopolar pulses. Biochemical and biophysical research communications, 443(2):568–73, 1 2014.

[152] Florin Ciobanu, Muriel Golzio, Eugenia Kovacs, and Justin Teissié. Control by Low Levels of Calcium of Mammalian Cell Membrane Electropermeabilization. The Journal of Membrane Biology, 251(2):221–228, 4 2018.

[153] Janja Dermol, Olga N. Pakhomova, Andrei G. Pakhomov, and Damijan Miklavčič. Cell Electrosensitization Exists Only in Certain Electroporation Buffers. PLOS ONE, 11(7):e0159434, 7 2016.

[154] Borja Mercadal, Christopher B Arena, Rafael V Davalos, and Antoni Ivorra. Avoiding nerve stimulation in irreversible electroporation: a numerical modeling study. Physics in Medicine and Biology ACCEPTED MANUSCRIPT, 2017.

[155] Olena M. Nesin, Olga N. Pakhomova, Shu Xiao, and Andrei G. Pakhomov. Manipulation of cell volume and membrane pore comparison following single cell permeabilization with 60- and 600-ns electric pulses. Biochimica et Biophysica Acta (BBA) - Biomembranes, 1808(3):792–801, 3 2011.

[156] Olga N Pakhomova, Betsy Gregory, Iurii Semenov, and Andrei G Pakhomov. Calcium-mediated pore expansion and cell death following nanoelectroporation. Biochimica et Biophysica Acta - Biomembranes, 1838(10):2547–2554, 2014.

[157] David I. Brown and Kathy K. Griendling. No Title. 47(9), 11 2009.

[158] R S Arnold, J Shi, E Murad, A M Whalen, C Q Sun, R Polavarapu, S Parthasarathy, J A Petros, and J D Lambeth. Hydrogen peroxide mediates the cell growth and transformation caused by the mitogenic oxidase Nox1. Proceedings of the National Academy of Sciences of the United States of America, 98(10):5550–5, 5 2001.

[159] Peter M. Burch and Nicholas H. Heintz. Redox Regulation of Cell-Cycle Re-entry: Cyclin D1 as a Primary Target for the Mitogenic Effects of Reactive Oxygen and Nitrogen Species. Antioxidants & Redox Signaling, 7(5-6):741–751, 5 2005.

[160] Joseph A. Ross, Keiran Vanden Dungen, Kamiko R. Bressler, Mikayla Fredriksen, Divya Khandige Sharma, Nirujah Balasingam, and Nehal Thakor. Eukaryotic initiation factor 5B (eIF5B) provides a critical cell survival switch to glioblastoma cells via regulation of apoptosis. Cell Death & Disease, 10(2):57, 2 2019.

[161] Myung Gwon Lee, Joong Ho Shin, Sungyoung Choi, and Je Kyun Park. Enhanced blood plasma separation by modulation of inertial lift force. Sensors and Actuators, B: Chemical, 190:311–317, 2014.

[162] P Pinton, C Giorgi, R Siviero, E Zecchini, and R Rizzuto. Calcium and apoptosis: ER-mitochondria Ca2+ transfer in the control of apoptosis. Oncogene, 27(50):6407–6418, 10 2008.

[163] V. Sridhara and R.P. Joshi. Evaluations of a mechanistic hypothesis for the influence of extracellular ions on electroporation due to high-intensity, nanosecond pulsing. Biochimica et Biophysica Acta (BBA) - Biomembranes, 1838(7):1793–1800, 7 2014.

[164] K. L. Hoejholt, T. Mužić, S. D. Jensen, L. T. Dalgaard, M. Bilgin, J. Nylandsted, T. Heimburg, S. K. Frandsen, and J. Gehl. Calcium electroporation and electrochemotherapy for cancer treatment: Importance of cell membrane composition investigated by lipidomics, calorimetry and in vitro efficacy. Scientific Reports, 9(1):4758, 12 2019.

[165] M. Broholm, T. Stigaard, M. Bulut, R. Vogelsang, I. Gögenur, and J. Gehl. Calcium electroporation for the treatment of colorectal cancer calcium endove – preliminary results. European Journal of Surgical Oncology, 45(2):e119, 2 2019.

[166] Christina Caroline Plaschke, Julie Gehl, Helle Hjorth Johannesen, Barbara Malene Fischer, Andreas Kjaer, Anne Fog Lomholt, and Irene Wessel. Calcium electroporation for recurrent head and neck cancer: A clinical phase I study. Laryngoscope Investigative Otolaryngology, 4(1):49–56, 2 2019.

[167] Nicholas E Navin. The first five years of single-cell cancer genomics and beyond, 10 2015.

[168] Assieh Saadatpour, Shujing Lai, Guoji Guo, and Guo Cheng Yuan. Single-Cell Analysis in Cancer Genomics, 10 2015.

[169] Travis W. Murphy, Qiang Zhang, Lynette B. Naler, Sai Ma, and Chang Lu. Recent advances in the use of microfluidic technologies for single cell analysis. The Analyst, 2018.

[170] N. Reginald Beer, Benjamin J. Hindson, Elizabeth K. Wheeler, Sara B. Hall, Klint A. Rose, Ian M. Kennedy, and Bill W. Colston. On-chip, real-time, single-copy polymerase chain reaction in picoliter droplets. Analytical Chemistry, 79(22):8471–8475, 11 2007.

[171] Eric Brouzes, Martina Medkova, Neal Savenelli, Dave Marran, Mariusz Twardowski, J. Brian Hutchison, Jonathan M. Rothberg, Darren R. Link, Norbert Perrimon, and Michael L. Samuels. Droplet microfluidic technology for single-cell high-throughput screening. Proceedings of the National Academy of Sciences of the United States of America, 106(34):14195–14200, 8 2009.

[172] Tao Geng, Richard Novak, and Richard A. Mathies. Single-cell forensic short tandem repeat typing within microfluidic droplets. Analytical Chemistry, 86(1):703–712, 1 2014.

[173] Shaun W. Lim, Tuan M. Tran, and Adam R. Abate. PCR-activated cell sorting for cultivation-free enrichment and sequencing of rare microbes. PLoS ONE, 10(1):e0113549, 1 2015.

[174] Rapolas Zilionis, Juozas Nainys, Adrian Veres, Virginia Savova, David Zemmour, Allon M. Klein, and Linas Mazutis. Single-cell barcoding and sequencing using droplet microfluidics. Nature Protocols, 12(1):44–73, 1 2017.

[175] Allon M. Klein, Linas Mazutis, Ilke Akartuna, Naren Tallapragada, Adrian Veres, Victor Li, Leonid Peshkin, David A. Weitz, and Marc W. Kirschner. Droplet barcoding for single-cell transcriptomics applied to embryonic stem cells. Cell, 161(5):1187–1201, 5 2015.

[176] Evan Z. Macosko, Anindita Basu, Rahul Satija, James Nemesh, Karthik Shekhar, Melissa Goldman, Itay Tirosh, Allison R. Bialas, Nolan Kamitaki, Emily M. Martersteck, John J. Trombetta, David A. Weitz, Joshua R. Sanes, Alex K. Shalek, Aviv Regev, and Steven A.

McCarroll. Highly parallel genome-wide expression profiling of individual cells using nanoliter droplets. Cell, 161(5):1202–1214, 2015.

[177] Tom Kamperman, Marcel Karperien, Séverine Le Gac, and Jeroen Leijten. Single-Cell Microgels: Technology, Challenges, and Applications, 8 2018.

[178] Saharnaz Bigdeli, Roger O. Dettloff, Curtis W. Frank, Ronald W. Davis, and Laurel D. Crosby. A simple method for encapsulating single cells in alginate microspheres allows for direct PCR and whole genome amplification. PLoS ONE, 10(2):e0117738, 2 2015.

[179] Yaolei Wang and Jinyi Wang. Mixed hydrogel bead-based tumor spheroid formation and anticancer drug testing. The Analyst, 139(10):2449–2458, 2014.

[180] Marie-Elena Brett, Alexandra L. Crampton, and David K. Wood. Rapid generation of collagen-based microtissues to study cell-matrix interactions. TECHNOLOGY, 4(2):80–87, 6 2016.

[181] Shaohua Ma, Manuela Natoli, Xin Liu, Martin P. Neubauer, Fiona M. Watt, Andreas Fery, and Wilhelm T. S. Huck. Monodisperse collagen–gelatin beads as potential platforms for 3D cell culturing. Journal of Materials Chemistry B, 1(38):5128, 9 2013.

[182] Minjeong Jang, Ilkyoo Koh, Seok Jae Lee, Jae Ho Cheong, and Pilnam Kim. Droplet-based microtumor model to assess cell-ECM interactions and drug resistance of gastric cancer cells. Scientific Reports, 7:41541, 1 2017.

[183] Angelo S. Mao, Jae Won Shin, Stefanie Utech, Huanan Wang, Oktay Uzun, Weiwei Li, Madeline Cooper, Yuebi Hu, Liyuan Zhang, David A. Weitz, and David J. Mooney. Deterministic encapsulation of single cells in thin tunable microgels for niche modelling and therapeutic delivery. Nature Materials, 16(2):236–243, 2 2017.

[184] Fanyi Li, Vinh X. Truong, Helmut Thissen, Jessica E. Frith, and John S. Forsythe. Microfluidic Encapsulation of Human Mesenchymal Stem Cells for Articular Cartilage Tissue Regeneration. ACS Applied Materials & Interfaces, 9(10):8589–8601, 3 2017.

[185] Simone Allazetta and Matthias P Lutolf. Stem cell niche engineering through droplet microfluidics, 2015.

[186] S. Allazetta, A. Negro, and M. P. Lutolf. Microfluidic Programming of Compositional Hydrogel Landscapes. Macromolecular Rapid Communications, 38(15):1700255, 8 2017.

[187] Donald R. Griffin, Westbrook M. Weaver, Philip O. Scumpia, Dino Di Carlo, and Tatiana Segura. Accelerated wound healing by injectable microporous gel scaffolds assembled from annealed building blocks. Nature Materials, 14(7):737–744, 7 2015.

[188] Jaekyung Koh, Donald R. Griffin, Maani M. Archang, An-Chieh Feng, Thomas Horn, Michael Margolis, David Zalazar, Tatiana Segura, Philip O. Scumpia, and Dino Di Carlo. Cell Delivery: Enhanced In Vivo Delivery of Stem Cells using Microporous Annealed Particle Scaffolds (Small 39/2019). Small, 15(39):1970208, 9 2019.

[189] Amir Sheikhi, Joseph de Rutte, Reihaneh Haghniaz, Outman Akouissi, Alireza Sohrabi, Dino Di Carlo, and Ali Khademhosseini. Microfluidic-enabled bottom-up hydrogels from annealable naturally-derived protein microbeads. Biomaterials, 192:560–568, 2 2019.

[190] Tom Kamperman, Sieger Henke, Claas Willem Visser, Marcel Karperien, and Jeroen Leijten. Centering Single Cells in Microgels via Delayed Crosslinking Supports Long-Term 3D Culture by Preventing Cell Escape. Small, 13(22):1603711, 6 2017.

[191] Yukiko T. Matsunaga, Yuya Morimoto, and Shoji Takeuchi. Molding cell beads for rapid construction of macroscopic 3D tissue architecture. Advanced Materials, 23(12):H90–H94, 3 2011.

[192] Stephanie M Willerth, Kelly J Arendas, David I Gottlieb, and Shelly Elese Sakiyama-Elbert. Optimization of fibrin scaffolds for differentiation of murine embryonic stem cells into neural lineage cells. Biomaterials, 27(36):5990–6003, 2006.

[193] Isabelle Catelas, Nadjah Sese, Benjamin M. Wu, James C.Y. Dunn, Sam Helgerson, and Bill Tawil. Human Mesenchymal Stem Cell Proliferation and Osteogenic Differentiation in Fibrin Gels in Vitro. Tissue Engineering, 12(8):2385–2396, 8 2006.

[194] Wendy Ho, Bill Tawil, James C.Y. Dunn, and Benjamin M. Wu. The behavior of human mesenchymal stem cells in 3D fibrin clots: Dependence on fibrinogen concentration and clot structure. Tissue Engineering, 12(6):1587–1595, 6 2006.

[195] Janahan Arulmoli, Heather J Wright, Duc T T Phan, Urmi Sheth, Richard A Que, Giovanni A Botten, Mark Keating, Elliot L Botvinick, Medha M Pathak, Thomas I Zarembinski, Daniel S Yanni, Olga V Razorenova, Christopher C W Hughes, and Lisa A Flanagan. Combination scaffolds of salmon fibrin, hyaluronic acid, and laminin for human neural stem cell and vascular tissue engineering. Acta Biomaterialia, 43:122–138, 2016.

[196] Monica L Moya, Yu-Hsiang Hsu, Abraham P Lee, Christopher C W Hughes, and Steven C George. In vitro perfused human capillary networks. Tissue engineering. Part C, Methods, 19(9):730–7, 9 2013.

[197] Seema M. Ehsan, Katrina M. Welch-Reardon, Marian L. Waterman, Christopher C. W. Hughes, and Steven C. George. A three-dimensional in vitro model of tumor cell intravasation. Integrative Biology, 6(6):603, 5 2014.

[198] G F Christopher and S L Anna. Microfluidic methods for generating continuous droplet streams, 2007.

[199] Adam R. Abate, Julian Thiele, and David A. Weitz. One-step formation of multiple emulsions in microfluidics. Lab on a Chip, 11(2):253–258, 1 2011.

[200] Tatiana Trantidou, Yuval Elani, Edward Parsons, and Oscar Ces. Hydrophilic surface modification of pdms for droplet microfluidics using a simple, quick, and robust method via pva deposition. Microsystems and Nanoengineering, 3, 2017.

[201] Claire Robertson. Theory and practical recommendations for autocorrelation-based image correlation spectroscopy. Journal of Biomedical Optics, 17(8):080801, 8 2012.

[202] Claire Robertson, Kenji Ikemura, Tatiana B. Krasieva, and Steven C. George. Multiscale analysis of collagen microstructure with generalized image correlation spectroscopy and the detection of tissue prestress. Biomaterials, 34(26):6127–6132, 8 2013.

[203] Sadiq Mohammed Mir, Brenda Baggett, and Urs Utzinger. The efficacy of image correlation spectroscopy for characterization of the extracellular matrix. Biomedical Optics Express, 3(2):215, 2 2012.

[204] Susanne Wolbank, Valentin Pichler, James Crawford Ferguson, Alexandra Meinl, Martijn

Van Griensven, Andreas Goppelt, and Heinz Redl. Non-invasive in vivo tracking of fibrin degradation by fluorescence imaging. Journal of Tissue Engineering and Regenerative Medicine, 9(8):973–976, 8 2015.

[205] Stavros Thomopoulos, Melissa Zaegel, Rosalina Das, Fredrick L. Harwood, Matthew J. Silva, David Amiel, Shelly Sakiyama-Elbert, and Richard H. Gelberman. PDGF-BB released in tendon repair using a novel delivery system promotes cell proliferation and collagen remodeling. Journal of Orthopaedic Research, 25(10):1358–1368, 6 2007.

[206] Thomas Ward, Magalie Faivre, Manouk Abkarian, and Howard A. Stone. Microfluidic flow focusing: Drop size and scaling in pressure versus flow-rate-driven pumping. Electrophoresis, 26(19):3716–3724, 10 2005.

[207] Shelley L. Anna, Nathalie Bontoux, and Howard A. Stone. Formation of dispersions using "flow focusing" in microchannels. Applied Physics Letters, 82(3):364–366, 1 2003.

[208] U. Abildgaard. Acceleration of fibrin polymerization by dextran and ficoll. Interaction with calcium and plasma proteins. Scandinavian Journal of Clinical and Laboratory Investigation, 18(5):518–524, 1966.

[209] Nicholas A. Kurniawan, Thomas H.S. Van Kempen, Stijn Sonneveld, Tilaï T. Rosalina, Bart E. Vos, Karin A. Jansen, Gerrit W.M. Peters, Frans N. Van De Vosse, and Gijsje H. Koenderink. Buffers Strongly Modulate Fibrin Self-Assembly into Fibrous Networks. Langmuir, 33(25):6342–6352, 6 2017.

[210] Jon F. Edd, Dino Di Carlo, Katherine J. Humphry, Sarah Köster, Daniel Irimia, David A. Weitz, and Mehmet Toner. Controlled encapsulation of single-cells into monodisperse picoliter drops. In 12th International Conference on Miniaturized Systems for Chemistry and Life Sciences - The Proceedings of MicroTAS 2008 Conference, pages 1828–1830. Chemical and Biological Microsystems Society, 2008.

[211] Evelien W.M. Kemna, Rogier M. Schoeman, Floor Wolbers, Istvan Vermes, David A. Weitz, and Albert Van Den Berg. High-yield cell ordering and deterministic cell-in-droplet encapsulation using Dean flow in a curved microchannel. Lab on a Chip, 12(16):2881–2887, 8

2012.

[212] Adam R. Abate, Chia Hung Chen, Jeremy J. Agresti, and David A. Weitz. Beating Poisson encapsulation statistics using close-packed ordering. Lab on a Chip, 9(18):2628–2631, 2009.

[213] Ming Li, Mark van Zee, Carson T. Riche, Bobby Tofig, Sean D. Gallaher, Sabeeha S. Merchant, Robert Damoiseaux, Keisuke Goda, and Dino Di Carlo. A Gelatin Microdroplet Platform for High-Throughput Sorting of Hyperproducing Single-Cell-Derived Microalgal Clones. Small, 14(44):1803315, 11 2018.

[214] Jean Christophe Baret, Oliver J. Miller, Valerie Taly, Michaël Ryckelynck, Abdeslam El-Harrak, Lucas Frenz, Christian Rick, Michael L. Samuels, J. Brian Hutchison, Jeremy J. Agresti, Darren R. Link, David A. Weitz, and Andrew D. Griffiths. Fluorescence-activated droplet sorting (FADS): Efficient microfluidic cell sorting based on enzymatic activity. Lab on a Chip, 9(13):1850–1858, 2009.

[215] Keunho Ahn, Charles Kerbage, Tom P. Hunt, R. M. Westervelt, Darren R. Link, and D. A. Weitz. Dielectrophoretic manipulation of drops for high-speed microfluidic sorting devices. Applied Physics Letters, 88(2):1–3, 2006.

[216] Jeonghun Nam, Hyunjung Lim, Choong Kim, Ji Yoon Kang, and Sehyun Shin. Density-dependent separation of encapsulated cells in a microfluidic channel by using a standing surface acoustic wave. Biomicrofluidics, 6(2), 4 2012.

[217] Tengyang Jing, Ramesh Ramji, Majid Ebrahimi Warkiani, Jongyoon Han, Chwee Teck Lim, and Chia Hung Chen. Jetting microfluidics with size-sorting capability for single-cell protease detection. Biosensors and Bioelectronics, 66:19–23, 4 2015.

[218] Linas Mazutis, John Gilbert, W Lloyd Ung, David A Weitz, Andrew D Griffiths, and John A Heyman. Single-cell analysis and sorting using droplet-based microfluidics. Nature protocols, 8(5):870–91, 5 2013.

[219] Bo Cai, Tian Tian Ji, Ning Wang, Xin Bo Li, Rong Xiang He, Wei Liu, Guobin Wang, Xing Zhong Zhao, Lin Wang, and Zheng Wang. A microfluidic platform utilizing anchored

water-in-oil-in-water double emulsions to create a niche for analyzing single non-adherent cells. Lab on a Chip, 19(3):422–431, 2019.

[220] Fanben Meng, Carolyn M. Meyer, Daeha Joung, Daniel A. Vallera, Michael C. McAlpine, and Angela Panoskaltsis-Mortari. 3D Bioprinted In Vitro Metastatic Models via Reconstruction of Tumor Microenvironments. Advanced Materials, 31(10):1806899, 3 2019.

[221] Linfen Yu, Cynthia Ni, Samantha M. Grist, Carmen Bayly, and Karen C. Cheung. Alginate core-shell beads for simplified three-dimensional tumor spheroid culture and drug screening. Biomedical Microdevices, 17(2), 2015.

[222] Tamer A.E. Ahmed, May Griffith, and Max Hincke. Characterization and Inhibition of Fibrin Hydrogel–Degrading Enzymes During Development of Tissue Engineering Scaffolds. Tissue Engineering, 13(7):1469–1477, 7 2007.

[223] Mark A. Skylar-Scott, Sebastien G.M. Uzel, Lucy L. Nam, John H. Ahrens, Ryan L. Truby, Sarita Damaraju, and Jennifer A. Lewis. Biomanufacturing of organ-specific tissues with high cellular density and embedded vascular channels. Science Advances, 5(9), 9 2019.